IOWA STATE UNIVERSITY
Digital Repository

Graduate Theses and Dissertations | Graduate College

2015

Experimental and numerical study of Taylor-Couette flow

Haoyu Wang
Iowa State University

Follow this and additional works at: http://lib.dr.iastate.edu/etd

 Part of the Mechanical Engineering Commons

Recommended Citation
Wang, Haoyu, "Experimental and numerical study of Taylor-Couette flow" (2015). *Graduate Theses and Dissertations*. 14462.
http://lib.dr.iastate.edu/etd/14462

This Dissertation is brought to you for free and open access by the Graduate College at Iowa State University Digital Repository. It has been accepted for inclusion in Graduate Theses and Dissertations by an authorized administrator of Iowa State University Digital Repository. For more information, please contact digirep@iastate.edu.

Experimental and numerical study of Taylor-Couette flow

by

Haoyu Wang

A dissertation submitted to the graduate faculty

in partial fulfillment of the requirements for the degree of

DOCTOR OF PHILOSOPHY

Major: Mechanical Engineering

Program of Study Committee:

Michael G. Olsen, Major Professor

Terry Meyer

Shankar Subramaniam

James Christian Hill

Richard Dennis Vigil

Iowa State University

Ames, Iowa

2015

Copyright © Haoyu Wang, 2015. All rights reserved.

TABLE OF CONTENTS

LIST OF TABLES

LIST OF FIGURES

ACKNOWLEDGEMENTS

I would like to take this opportunity to express my thanks to those who helped me with various aspects of conducting research and the writing of this thesis.

First and foremost, Dr. Michael G. Olsen for his guidance, patience and support throughout this research and the writing of this thesis. His insights and words of encouragement have often inspired me and renewed my hopes for completing my graduate education. I feel lucky for receiving the opportunity to work with him and am certain that doing so has made me a much better engineer.

I would also like to thank my committee members for their efforts and contributions to this work: Dr. Dennis Vigil, Dr. James Christian Hill, Dr. Shankar Subramaniam and Dr. Terry Meyer.

In addition, I would additionally like to thank Dr. Bo Kong for his help and useful suggestions throughout the research and writing of this thesis. To fellow graduate students in the Department of Mechanical Engineering, thank you for all your support.

Finally, I would like to thank my wife and my parents, who constantly support and encourage me.

ABSTRACT

Taylor-Couette flow between in a gap of two coaxial cylinders is studied using a combination of particle image velocimetry (PIV) experimental data and computational fluid dynamics (CFD). Wavy vortex flow and modulated wavy vortex flow which are two flow regimes of Taylor-Couette flow are investigated using the PIV technique and power spectral density. In addition, the turbulent Taylor-Couette flow is studied by means of Reynolds-average Navier-Stokes (RANS) simulations and stereo-PIV. Two main turbulence models of Reynolds-average Navier-Stokes simulations are used in the investigation and verified with the PIV experimental data. The investigations provide in-depth evaluation of the simulation schemes.

This work shows that computational fluid dynamics in combination with PIV data is an excellent tool to study turbulent structures in the Taylor-Couette flow. Furthermore, this work demonstrates the in-depth evaluation of RANS simulation.

CHAPTER 1. INTRODUCTION

Taylor-Couette flow is a canonical flow geometry that has long been a subject of interest in the fluid mechanics community. The study of Taylor-Couette flow is useful in many research and industrial applications, such as water purification and desalination (Dutta and Ray, 2004; Sengupta etc al., 2001; Wereley and Lueptow, 1998), and bisectors (Bo and Vigil, 2013; Curran and Black, 2005; Haut etc al., 2003).

General Introduction

The flow in a gap of two coaxial cylinders, when inner one is rotating and outer one is at rest, called Taylor-Couette flow, is a classical and important subject in fluid mechanics. Over one hundred years ago, Maurice Couette, a French physicist, designed an apparatus consisting of two coaxial cylinders, with the space between the cylinders being filled with a viscous fluid and the outer cylinder being rotated at angular velocity ω. The purpose of this experiment was to deduce the viscosity of the fluid from measurements of the torque exerted by the fluid on the inner cylinder. When ω is not too large, the fluid flow is nearly laminar, and the method of Couette becomes very useful for measuring viscosity because the torque is then proportional to $\nu \cdot \omega$ where ν is the kinematic viscosity of the fluid. If ω is increased beyond a transition point, the flow will eventually become turbulent. The Taylor-Couette flow system exhibits a series of instabilities, both laminar and turbulent, as the rotating velocity of the inner cylinder is increased. Many researchers had made significant contributions to the understanding

of flow transitions and turbulence by studying this canonical flow system (Taylor, 1923; Davey, 1962; Coles, 1965; Gollub and Freilich, 1976; Walden and Donnelly, 1979; Gorman and Swinney, 1979, 1982; Berland et al., 1986; Wereley and Lueptow, 1994; Smith and Matsoukas, 1998).

Because of its interest in the fluid mechanics community, Taylor-Couette flow has been studied over a 100 years. The study of Taylor Couette flow began as early as the year 1890 and still continues on today due to its importance to various areas of fundamental and applied research. Before the development of laser-based measurement techniques, the flow was studied by visual observations such as Couette (1890) described a series of experiments in which he measured the viscosities of water and air using the concentric cylinder apparatus of his own design, Taylor (1923) used ink visualization and presented for the first time measurements of patterns in the unstable flow, and Taylor (1936) reported the a series of measurements of the torque on the cylinder of Couette flow apparatus due to the rotation of the other for a variety of radius ratios and Reynolds numbers, and by intrusive electrical measurements such as Taylor (1936) described the velocity profile of Taylor-Couette flow observed and measured by Pitot tube where the outer cylinder rotated and the inner cylinder was fixed, Wendt (1933) reported measurements of velocity and pressure distributions inside the gap between the inner and outer cylinders of Taylor-Couette flow apparatus, Bagnold (1954) designed a Couette rheometer to measure the shear and normal forces on the inner cylinder and described the relationship between the shear and normal stresses, Hollis-Hallett and W.J. Heikkila (1955) adapted the Hollis-Hallet's viscometer to study the Taylor-Couette flow at very low Reynolds number, and Coles (1965) used hot-wire measurement in air to investigate the transition in Taylor-Couette flow and showed 'patterns of alternating laminar and turbulent flow'. The development of laser Doppler velocimetry was a big advantage in the study of Taylor-Couette flow as it allowed for the non-intrusive measurement of velocity. Over the past two decades, with the advancement of Particle Image Velocimetry

(PIV) and Planar Laser-Induced Fluorescence (PLIF) which have provided the ability to measure instantaneous velocity and concentration fields and have thus become very popular experimental techniques for the study of unsteady and turbulent flows. Compared to Laser Doppler Velocimetry which is a point-wise measurement technique, flow field data measured by PIV can be simultaneously collected at a large number of points over a two-dimensional or even three-dimensional domain.

Gollub and Swinney (1975) investigated the time-dependent local radial velocity in Taylor-Couette flow with Light-scattering measurements. Three flow regimes, TVF, WVF, and MWVF, were observed as the Reynolds number increased. Walden and Donnely (1979) investigated Taylor-Couette flow in a reactor in which length-gap aspect ratio could change using both visual observations and electrical measurements. Electrical measurements were made with collectors attached to the gold-plated brass outer cylinder. In their research, they observed and reported the WVF regime and the disappearance of the azimuthal waves in the Taylor-Couette flow. They also reported a unexplained reemergence of a sharp peak in their power spectrum study. However, they claimed that the reemergence was only for a large aspect ratio system. Lueptow (1992) performed electrical measurements using a photodiode to investigate Taylor-Couette flow. A wide range of different flow regimes was observed in this research which was basically an observational study of Taylor-Couette flow.

Non-intrusive measurements of velocity have been widely used in the study of Taylor-Couette flow. For example, Fenstermacher et al. (1979) used Laser Doppler velocimetry (LDV) to measure the local radial velocity in a chaotic Taylor vortex flow. The measurements were limited to a radial component passing through the vortex centers. Their measurements ranged from relative Reynolds number 5.4 to 45. Power spectra were calculated and used to analyze the experiment results which indicated the increasing small scale structure in the flow and the disappearance of the azimuthal waves with increasing Reynolds number. Takeda et al. (1999, 2008) used laser doppler velocimetry

to measure axial and radial velocities and also used particle tracking velocimetry (PTV) to investigate azimuthal velocity. Their research focused mainly on WVF, MWVF, and the reappearance of azimuthal waves. Wereley and Lueptow (1994, 1998, 1999) used laser Doppler velocimetry to measure the azimuthal velocity and PIV to measure time-resolved axial and radial velocities in a meridional plane for both wavy and non-wavy vortex flow. Axial flow was found winding around the vortices for both non-wavy and wavy vortices. In wavy vortex flow, the vortices were found to translate along with the axial flow at low Reynolds number and be more random in character at higher Reynolds number. Akonura and Lueptow (2003) measured the azimuthal and radial velocities in latitudinal planes perpendicular to the axis of rotation using particle image velocimetry for the Taylor-Couette flow. Their measurements focused in the WVF. Azimuthal momentum was found to be transported radially by vortical motion and axially by the axial exchange of fluid between vortices in wavy vortex flow, and these effects were also found to strengthen. Wang et al. (2005) used PIV to investigate the reappearance of azimuthal waves in Taylor vortex flow. However, in his experiments, Wang only measured two component velocity data, the axial and radial velocities. In these previous experimental investigations, the different techniques (LDV and PIV) used to investigate Taylor-Couette flow only provided one or two components of velocity data, and the researchers were primarily focused on the transition from WVF through MWVF to the onset of TVF.

In the present work, stereoscopic particle image velocimetry is used to collect all three velocity components, axial, radial, and azimuthal velocities, simultaneously in a two-dimensional field in Taylor-Couette flow. A wide range of relative Reynolds numbers have been selected in the current work, ranging from 6 to 200 and including flow regimes from WVF through MWVF to highly TTVF. Three component velocity field data over this large range of Reynolds numbers can provide detailed information for investigating Taylor-Couette flow. The velocity fields from the PIV measurements provide visualiza-

tion of WVF, MWVF, TTVF, and transitions between the various flow regimes. The PIV data for turbulent Taylor-Couette flow are also used for the validation of numerical simulation models in this work for all three mean velocity components, turbulence kinetic energy, and dissipation rate.

The numerical study of Taylor-Couette flow has also developed rapidly in recent decades with increases in computer technology. These advances have led to different turbulent modeling methods of Computational Fluid Dynamics (CFD) to be performed on Taylor-Couette flows. Same examples are the various Reynolds-Averaged Navier-Stokes (RANS) methods which are the most common CFD method for turbulent flows due to their being less expensive than more computationally intensive techniques such as Large-Eddy simulation (LES) and Direct Numerical simulation (DNS). However, the accuracy of CFD models must be tested, and one important role of experiments is to validate the predictions of CFD.

Numerical simulation in Taylor-Couette flow has been the focus of study of many researchers. Some simulation studies have used RANS simulations. For example, Wild et al. (1996) used a RANS simulation with the $k-\varepsilon$ model to predict the Taylor-Couette reactor torque and compared the results to experimental torque measurements, Batten et al. (2002) performed RANS simulations using a low Reynolds number $k-\omega$ model to study the transition to turbulent flow in Taylor-Couette reactor at low Reynolds numbers. Both of these studies used steady-state simulations. Friess et al. (2013) simulated a Taylor-Couette-Poiseuille flow using both a hybrid RANS/LES model and pure RANS model. In their research, the RANS simulations were performed on a 1D grid using only the azimuthal velocity in the Taylor-Couette flow.

Most simulations of Taylor-Couette flow have been done using LES and DNS. For example, Liao et al. (1999) used DNS to investigate a Taylor-Couette flow system with a semi-implicit projection method to solve the unsteady, three-dimensional Navier-Stokes equations in a cylindrical coordinate system. Flow patterns were obtained in the simula-

tion of laminar Taylor-Couette flow at low Reynolds numbers. The numerical code was proved to accurately simulate the unsteady Taylor-Couette flow. Bilson and Bremhorst (2007) investigated the Taylor-Couette flow for a Reynolds number of 3200 with direct numerical simulation. In their simulation, secondary near-wall vortex pares and weaker evidence of secondary vortices were observed. The mean velocity, velocity fluctuation intensities, Reynolds stress budgets, and visualization of the instantaneous velocity fluctuation field were compared with experiments. Farnik and Kozubkova (2006) presented a simulation study of laminar Taylor-Couette flow in counter rotating concentric cylinders using DNS. Taylor-Couette flow was simulated over a wide range of flow regimes, including TVF, WVF, MWVF, and TTVF. Velocity and flow statistics from the simulation were compared with experiments and proved to be accurate for simulating the nonlinear cases for Taylor vortices. Pirro and Quadrio (2007) performed DNS simulations to investigate turbulent Taylor-Couette flow. Their code was validated by computing several physical quantities available from previous DNS or experiments in the laminar and transitional regimes. Almost constant angular momentum, the numerical value of which was compared with experiment result, was revealed by their simulation. Dong (2007, 2008) investigated the dynamical and statistical features of turbulent TaylorCouette flow through three-dimensional direct numerical simulations (DNS) at Reynolds numbers ranging from 1000 to 8000. In their investigation, with increasing Reynolds number, Görtler vortices concentrated at the outflow boundaries of Taylor vortex cells and the prevailing structure in the flow were azimuthal vortices. Standard Taylor-Couette and the counter rotating systems were compared in the simulation to demonstrate the profound effects of the Coriolis force on the mean flow and other statistical quantities. Though the simulation of Taylor-Couette flow performed with LES and DNS has been proved to be accurate, interest of the accuracy of Reynolds-averaged Navier-Stokes simulations of the Taylor-Couette flow drives the numerical study with RANS in this work, because RANS simulations, which model all the turbulence are much faster and less expensive

compared to other simulation methods. Simulation works that have been done in the previous researches and the current work for different flow regimes can be found in the Table 1.1.

Table 1.1 Numerical simulation works of Taylor-Couette flow

Flow Regimes	**Investigator**	**Simulation Method**
TVF	Liao et al. (1999)	DNS
	Battern et al. (2002)	RANS
	Farnik and Kozubkova (2006)	DNS
	Pirro and Quadrio (2007)	DNS
WVF	Farnik and Kozubkova (2006)	DNS
	Dong (2008)	DNS
	Present work	RANS ($k-\varepsilon$ and $k-\omega$ models)
MWVF	Friess (2013)	hybrid RANS/LES model & RANS
	Dong (2008)	DNS
	Farnik and Kozubkova (2006)	DNS
TTVF	Wild et al. (1996)	RANS
	Bilson and Bremhorst (2007)	DNS
	Farnik and Kozubkova (2006)	DNS
	Pirro and Quadrio (2007)	DNS
	Dong (2007)	DNS
	Present work	RANS ($k-\varepsilon$ and $k-\omega$ models)

Velocity profiles of all three velocity components in Taylor-Couette flow as well as turbulent kinetic energy and dissipation rate have also been collected for comparison in the present work. Simulation results are validated with the PIV data to investigate the accuracy of the RANS simulations. In this work, unsteady simulations are performed in order to capture any unsteady bulk motions in the flow.

Turbulence models are required to close the RANS equations. In this work, two commonly used two-equations turbulence models, the $k-\varepsilon$ model and the $k-\omega$ model, are investigated. Since these two models are the most commonly used RANS turbulence model, once RANS simulations using these two turbulence models are validated to be accurate, the models can be confidently transferred to other applications using simulations of Taylor-Couette flow, such as heat transfer and mass transfer.

Power Spectral Density is a tool to describe how the power of a signal or time series is distributed over different frequencies. It is one of the most widely used methods of data analysis of time-varying signals and can be regarded as the analysis of the variance of time series using sinusoids. Power spectral density is a powerful tool to study and analyze the various flow regimes and transitions in Taylor-Couette flow. Since the spatial and temporal nature of the PIV data presented in this work allows the identification and characterization of vortex structures, the presented experimental and numerical studies of Taylor-Couette flow are focused on the flow structure of Taylor-Couette with particular emphasis on using the power spectral density function to investigate the various flow transitions.

Dissertation Organization

The reminder of this thesis is organized as follows: In Chapter 2, velocity fields in a meridional plan are measured using Particle Image Velocimetry (PIV). Vortex characteristics and flow transitions were examined using the Power Spectral Density (PSD) function. The results of the power spectral density and investigation of the vortex structures revealed the spatio-temporal character for different flow regimes in the Taylor-Couette flow. A computational investigation of Taylor-Couette flow is presented in Chapter 3. Computational fluid dynamics (CFD) simulations using Reynolds-Averaged Navier-Stokes (RANS) equation using the kappa-epsilon turbulence model were performed and the flow field predictions were validated with the PIV experimental data. The power spectral density function results were compared between CFD and experiment to verify the precision of computational model. Next, the kappa-omega turbulence model was used in RANS simulations to compare with the experimental results and previous kappa-epsilon simulation, and results are presented in Chapter 4. Finally, summary and conclusions are given in Chapter 5. Some future work is also briefly discussed.

CHAPTER 2. POWER SPECTRUM ANALYSIS IN TAYLOR-COUETTE FLOW

A paper in preparation

Abstract

Experimental research was performed by acquiring time-dependent, three-component velocity field data for Taylor-Couette flow in the annular gap between an inner rotating cylinder and a stationary concentric outer cylinder using high-speed stereoscopic Particle Image Velocimetry (PIV). Flow regimes corresponding to wavy vortex flow, modulated wavy vortex flow, and turbulent Taylor vortex flow were investigated with data which were collected over a large range of rotational Reynolds numbers. The velocity fields were analyzed for the different Reynolds numbers spanning the different flow regimes in Taylor-Couette flow. In particular, the characteristics of travelling azimuthal waves were investigated. The wavy motion was found to weaken and disappear as the Reynolds number increased to R=17, and then reappeared at a higher frequency when Reynolds number increased beyond R=17 before weakening and disappearing for R>24. The Power Spectral Density (PSD) function was used to analyze the wavy motion in the Taylor-Couette flow. The magnitude of the peak frequency in the PSD which corresponded to strength of the travelling azimuthal waves at that frequency and was used as a measure of the wavy motion in the flow. The magnitude of this peak decreased from a maximum at R=6 as the Reynolds numbers increased until reaching a minimum at R=17. This agreed the results observed in the velocity fields that showed the wavy motion diminished with

increasing Reynolds number and the azimuthal waves disappeared at R=17. As Reynolds number increased beyond R=17, a new peak appeared in the PSD at a higher frequency, and the flow again showed periodic motion before the new peak also decreased with increasing Reynolds number and disappeared again in the PSD.

Introduction

The flow in the gap between two coaxial cylinders, when inner one is rotating and outer one is at rest, is called Taylor-Couette flow which is one of the canonical flow fields in fluid mechanics. The Taylor-Couette flow system exhibits a series of instabilities, in both the laminar and turbulent regimes, as the rotational velocity of the inner cylinder is increased, Fig. 2.1. Due to the complex series of instabilities that arises in this flow, many researches have studied Taylor-Couette flow using theoretical, computational, and experimental techniques for more than a century.

The behavior of a Newtonian fluid confined in the annulus (with a stationary outer cylinder) can be characterized by the rotational Reynolds number,

$$Re = \frac{\omega r_i \left(r_i - r_o\right)}{\nu} \tag{2.1}$$

where ω is the inner cylinder angular velocity, r_i and r_o are the radii of the inner and outer cylinders, respectively, and ν is the kinematic viscosity of the fluid. When Re is increased above but very close to a critical point, Re_c, it is found that the laminar flow is unstable with respect to axisymmetric perturbations with wavenumber in the range bounded by the neutral stability curve and Taylor vortices appear in the flowfield. The critical Reynolds number of the onset of Taylor vortices depends on the radius ratio of the cylinders $\eta = r_i/r_o$. (Coles, 1965; Eagles, 1974) The initial bifurcation from the laminar state is characterized by the appearance of toroidal vortices positioned about the axis of the cylinder in pairs of opposite circulation. This vortex state is known as Taylor vortex flow (TVF) (Taylor, 1923). Taylor investigated theoretically and experimentally the

stabilities of azimuthal Couette flow with both cylinders rotating. He studied in detail only the onset of axisymmetric Taylor vortices. Several limited measurements of the velocity in Taylor vortex flow have been made using Laser Doppler Velocimetry (LDV). (Heinrichs et al., 1988; Gollub and Freilich, 1976; Berland et al., 1986; Wereley and Lueptow, 1994) These measurements were collected at various location in the flowfield for each of one velocity component (the radial velocity (v_r), the axial velocity (v_z), or the azimuthal velocity (v_θ)). Later, Particle image velocimetry (PIV) was used to measure v_r and v_z in a meridional plane for laminar vortex flow by Wereley and Lueptow (1998). All these measurements confirmed the validity of Davey's perturbation expansion of the NavierStokes equations about the cylindrical Couette flow solution (Davey, 1962), particularly that the vortices strengthen with increasing rotational Reynolds number. Upon further increasing Re above the critical value, the system exhibits a sequence of distinct time-dependent instabilities and flow regimes before the onset of turbulence. These secondary instabilities occur when TVF gives way to a wavy vortex flow (WVF). Wavy vortex flow in a cylindrical Couette device is characterized by travelling azimuthal waves superimposed on the inflow and outflow boundaries of the Taylor vortices is more complex than non-wavy flow. The vortex centers, which are defined as the points within a vortex where the axial and radial velocities vanish in a meridional plane, display radial undulations in addition to moving axially. Compared to non-wavy Taylor vortex flow, the flow field of wavy vortex flow is unsteady and fully three-dimensional, with three components of velocity and three nonzero gradients of velocity.

As Re is increased even higher, the amplitude of the azimuthal waves begins to vary with time, giving rise to a quasiperiodic regimes known as modulated Wavy Vortex flow (MWVF), which has been characterized in detail by Gorman and Swinney (1982). Modulated Wavy Vortex flow involves non-axisymmetric vortices described by two temporal frequencies. Coughlin et al. (1991) reported that there are two different modes for MWVF, and that for some parameter ranges they coexist. The two-traveling-wave flows

studied by Gorman and Swinney (1979,1982) and Shaw et al. (1985) extends the investigation of two modes in MWVF with spectrum analysis. Moreover, the 'non-traveling modulation' discovered by Zhang and Swinney (1985) appears near the outflow region with a higher phase speed inducing the appearance of a ripple on the roll. On further increasing Re, many researchers have observed that the azimuthal waves disappear at some critical Re, beyond which the flow is turbulent, even though the Taylor vortex structure remains. (Colse, 1965; Walden and Donnelly, 1979; Fenstermacher et al., 1979; Burkhalter and Koschmieder, 1973). This flow is called turbulent Taylor vortex flow (TTVF). This turbulent Taylor vortex flow becomes increasingly complex as Re increases until the vortex structures eventually become indiscernible (Smith and Matsoukas, 1998).

Particle image velocimetry (PIV) is a whole-flow-field technique that provides instantaneous velocity vector field measurements in a planar region of a flow. In regular PIV, two velocity components are measured, but using a stereoscopic approach permits all three velocity components to be measured, resulting in instantaneous three-component velocity vectors for the entire measurement area. In recent years, PIV has been applied to Taylor-Couette flow. Wereley and Lueptow (1998) measured the radial and axial velocities in a meridional plane for both wavy and nonwavy Taylor vortex flow using PIV and were able to calculate the azimuthal component of the velocity field for this axisymmetric flow. Akonur and Lueptow (2003) used PIV to measure the azimuthal and radial velocity components in the latitudinal planes perpendicular to the axis of rotation of wavy Taylor-Couette flow. Wereley et al. (2002) studied fluid velocity fields in Taylor-Couette flow containing particles in the rotating filtration of a suspension using PIV and particle tracking velocimetry. All these previous studies focused on low Reynolds number and wavy vortex flow. Also, the particle image velocimetry satem used in these studies were regular 2D PIV systems.

Power Spectral Density (PSD) describes how the power of a signal or time series is distributed over frequencies. In Taylor-Couette flow, there is a traveling azimuthal flow

in WVF and MWVF, so a PSD can be performed and used as a method to analyze these wavy Taylor-Couette flows in a efficient way. It will be demonstrated that PSD is very useful for identifying traveling azimuthal waves in Taylor-Couette flow. In the present work, we present a study on Taylor-Couette flow using high speed PIV measurements and power spectral density analysis of Taylor vortex flow for a range of reduced Reynolds numbers corresponding to WVF, the transition to MWVF, and TTVF.

Experiment Apparatus and Procedure

Experiment Apparatus

The Taylor-Couette flow apparatus used in present work was fabricated using two concentric Plexiglas cylinders and is shown schematically in Fig. 2.2. The diameters of the rotating inner cylinder and the fixed outer cylinder are $2r_i = 6.985\ cm$ and $2r_o = 9.525\ cm$, respectively, resulting in a gap width of $d = 1.27\ cm$ and a radius ratio of $\eta = r_i/r_o = 0.733$. The inner cylinder is driven by a compumotor control system (Parker Hannifin Corporation) and has acrylic end caps fitted with stainless steel drive shafts on the central axis. The length of the cylinder is 43.2 cm resulting in a cylinder aspect ratio, τ, of 34. Leakage paths between stationary components are sealed with o-rings. Two o-rings are used as a mechanical seal to block the leakage path between the rotating and stationary interface of the driving shaft.

In order to eliminate optical distortion, a working fluid was chosen that has a refractive index matched to that of the Plexiglas (Parker and Merati, 1996). This working fluid was a mixture of water, glycerol, sodium iodide, and small quantities of sodium thiosulfate. The outer cylinder was enclosed in a square Plexiglas box and this enclosure was also filled with the working fluid. To create the working fluid, sodium iodide and trace amounts of sodium thiosulfate were added into a mixture of water (90% by volume) and glycerol (10% by volume) until the solution was saturated. Then, additional 90%

water-glycerol mixture was added to the solution until the refractive index of the fluid matched the refractive index of Plexiglas (1.4905).

Silver-coated hollow glass beads (Potters Industries, NJ) were added into the solution as PIV seed particles in a weight concentration of approximately 8.2×10^{-6}. The seed particles had a density of 1.6 g/cm^3 and a mean diameter of 13 μm. This density made the seed particles nearly neutrally buoyant in the working fluid, which was found to be 1.85 g/cm^3. The temperature of the working fluid and the room was kept at 24 °C and varied by no more than 0.1 °C over the course of an experimental run. The nominal kinematic viscosity of the fluid was measured as $1.71 \times 10^{-6}\ m^2/s$ using a Canon-Fenske viscometer.

The flow velocities were measured using a LaVison Inc. high speed stereoscopic Particle Image Velocimetry (PIV) system. A schematic of the apparatus and stereo PIV system is shown in Fig. 2.3. Two high-resolution, high-speed CCD cameras set to an oblique angle to the laser sheet were used to capture the particle images in a plane illuminated in the middle of the reactor through the outer cylinder by a laser light sheet. The laser beam from a high-speed laser was formed into a thin sheet by a spherical plano-convex lens followed by a cylindrical planoconcave lens and then reflected by a mirror towards the test section. The laser sheet had a thickness of $0.5mm$ in the measurement area. The laser sheet was carefully aligned in the meridional plane to avoid a possible anomalous apparent radial velocity component caused by the azimuthal path of the particles through the laser sheet. LaVison Davis 7.0 software was used to control the laser pulses, image acquisition, and analysis of resulting images. For each of the Reynolds number investigated, 2048 image pairs measuring 1024 pixels axially and 1024 pixels radially were captured. Velocity vectors were calculated using a cross-correlation technique and an interrogation region measuring 32×32 pixels with 50% overlap between adjacent interrogation regions. This resulted in a velocity vector spacing of 0.4 mm. The velocity measurements had an experimental uncertainty of approximately 2% (Prasad

et al., 1992). In all the PIV images presented in this work, the top boundary of image represents the inner cylinder wall and the bottom boundary of image represents the outer cylinder wall.

Before the PIV measurements were carried out, a calibration was performed in order to convert the measured velocities from pixels to millimeters. The calibration was done by placing a three dimensional calibration plate in the object plane. As the separation between two points in the calibration plate was known, these known positions could be used to calibrate the PIV images.

Experimental Procedure

The critical Reynolds number for the onset of LVF for a Taylor-Couette system occurs near $Re_c = 99.53$ (Taylor, 1923). Using this value of Re_c, a Reynolds number ratio can be calculated,

$$R = \frac{Re}{Re_c} \tag{2.2}$$

In this work, R was varied between 6 and 200, spanning from Wavy Vortex flow (WVF) to turbulent Vortex flow (TVF).

The uncertainty in the Reynolds number due to the variation in the inner cylinder velocity, fluid viscosity and other factors was less than 4%. The uncertainty in the velocity measurements depends on the ability of seed particles to follow the flow and the accurate measurement of the particles' average displacement between PIV images.

It is well know that hysteresis effects may play an important role in Taylor vortex formation (Park et al., 1981; Anderec et al., 1986). In this experiment to ensure a consistent number of Taylor vortices in the flowfield, one must carefully avoids a sudden acceleration to a high value of R or data acquiring shortly after start-up or before reaching a quasi-steady state. Also, in order to further ensure that the number of vortices were identical for each R, all experiments were performed using the following startup protocol. First, the inner cylinder was accelerated from rest to R=55 at a constant

angular acceleration of 0.314 rad/s^2. The inner cylinder rotation rate was then maintained at this angular velocity for half an hour, resulting in a flow state consisting of 14 vortex pairs, as confirmed by visual observation. Then, the rotation rate of the inner cylinder was increased at a constant angular acceleration of 0.314 rad/s^2 or reduced at a constant angular acceleration of 0.126 rad/s^2 until the desired value of R was reached. Then the number of vortex pairs at this new angular velocity was counted to make sure the desired 14 Taylor vortex were obtained. After the desired value of R was reached, the inner cylinder was maintained at the desired angular velocity for approximately 10 minutes before PIV data were collected.

Example PIV velocity fields

Figure 2.4 shows some examples of PIV velocity fields for different Reynolds numbers in Taylor Couette flow. Figure 2.4-a is an example velocity field at R=6, which is just beyond the transition to wavy vortex flow. The vortexes are in rectangular shape, and the inflow and outflow boundaries of the vortexes can be clearly seen extending from the top and bottom walls (i.e., the inner and outer cylinder walls). Figure 2.4-b is the velocity field for R=17, the Reynolds number at which the wavy motion reaches a minimum. The structure of velocity field at this R is similar to the structure at R=6, except for the absence of the azimuthal waves. Figure 2.4-c shows the velocity field at R=50, which is beyond the transition to turbulent Taylor vortex flow. The inflow and outflow exhibit "waviness" of their own, an indication that the flow at these boundaries is becoming turbulent. Also, it can be seen that small vortexes are beginning to appear inside the larger vortex structure a further indication of the transition to turbulence. At even higher R, such as R=80 as shown in Figure 2.4-d, the flow is even more turbulent. The inflow and outflow boundaries are more difficult to discern due to the turbulence in these regions. More small vortexes are visible inside the large vortex structure.

Data analysis

The power spectral density (PSD) describes how the power of a time series is distributed over various frequencies. In this project, PIV is used to measure instantaneous velocity fields by tracing the movement of fluid particles in the Taylor-Couette flow. In the PIV experiments, 2047 images were taken at equally spaced time intervals for each individual set of experiments. Multiple sets of 2047 images were obtained for each Reynolds number in the Taylor-Couette flow.

In order to calculate the power spectral density, the Fourier transform of the original data series must be calculated first. The Fourier transform decomposes a function of time into the frequencies that compose it. Fourier transformation is formally an analytic process which uses integral calculus. In our experiments, however, the integrand is a set of discrete experimental data, and the integration is necessarily done computationally. Thus, the Discrete Fourier Transform (DFT) is introduced and used in the present work. The discrete Fourier transform is the equivalent of the continuous Fourier Transform for signals known only at N instants separated by constant sample times. Since there are only a finite number of input data points, the DFT treats the data as if it were periodic.

Direct computation of the Discrete Fourier Transform (DFT) for a single N sequence requires $N-1$ complex additions and N complex multiplications. Thus, direct computation of all N points requires $N(N-1)$ complex additions and N^2 complex multiplications, which can be a prohibitive burden for large values of N. The practical implementation of the DFT on a computer usually uses the Fast Fourier Transform algorithm, which can the compute the DFT indirectly and reduce the computational complexity to the order of $N \log_2^N$. The fast Fourier transform computes the DFT and yields nearly the same results as evaluating the DFT directly, but the fast Fourier transform is much faster and less computationally intensive. Thus, the fast Fourier transform will be used instead of the DFT in calculating the power spectral density.

The input data sequences used for the calculation of Power Spectral Density are the fluid velocity components in each instantaneous velocity field realization obtained in the time series for each case in the Taylor-Couette flow. In each realization, the velocity field is calculated using the interrogation windows representing small area of the PIV images. The velocity data in each image are then recorded in a matrix form (x, y) over the recording area. In order to calculate the Power Spectral Density in one image, all the velocity data in the x array and y array are used and are exported as the input data, using a 2 dimension Fourier transform process.

The 2D Fourier transforms are calculated using a number of one dimensional Fourier transforms. First, a complex function $h(x, y)$ is a defined over a two-dimensional grid, 0 $\leqslant$ x $\leqslant$ N_1 -1, 0 $\leqslant$ y $\leqslant$ N_2 -1, and its two-dimensional discrete Fourier transform can be defined as a complex function $H(n_1, n_2)$, defined over the same grid,

$$H(n_1, n_2) = \sum_{x=0}^{N_1-1} \sum_{y=0}^{N_2-1} e^{-2\pi i x n_1/N_1} e^{-2\pi i y n_2/N_2} h(x, y), \tag{2.3}$$

and its inverse transform is then

$$h(x, y) = \frac{1}{N_1 \cdot N_2} \sum_{n_1=0}^{N_1-1} \sum_{n_2=0}^{N_2-1} e^{2\pi i x n_1/N_1} e^{2\pi i y n_2/N_2} H(n_1, n_2) \tag{2.4}$$

Considering all 2047 images taken in a time series, the Fourier transform for two dimensions in time can be used. The generalization of the Fourier transform to more than two dimensions, for example to L-dimensions, is represented by

$$H(n_1, ..., n_L) = \sum_{x_1=0}^{N_1-1} \cdots \sum_{x_L=0}^{N_L-1} e^{-2\pi i x_1 n_1/N_1} \cdots e^{-2\pi i x_L n_L/N_L} h(x_1, \cdots, x_L), \tag{2.5}$$

In order to use the fast Fourier transform, all N_1 to N_L should be a power of 2, which is an efficient length for an computing fast Fourier transform. In the most general situation a 2D Fourier transform consists of a complex array. However, the most common application of the fast Fourier transform is for image processing, where each value in the

array represents a scalar value at one pixel; therefore, the real value is the scalar value and the imaginary value is 0. If N is not a power of 2, the fast Fourier transform algorithm cannot be applied directly to the original data sequence. In this project, each velocity components at each array location is a real value, and zero padding is used to pad 0 into the array as the imaginary value.

After the original data sequence is zero padded, the PSD can be computed using the Danielson-Lanczos Lemma which is the most common fast Fourier transform algorithm. The PSD is calculated for velocity fluctuations around average values. With the Danielson-Lanczos Lemma, the structure of an fast Fourier transform algorithm has two sections. The first section sorts the data into bit-reversed order. The Fourier transform can be split into one sum over the even order and one over the odd order. The second section has an outer loop that is executed $\log_2 N$ times and calculates the transforms.

The definition of power spectral density, $P(f)$, of an N-point sequence $x(t)$, can be expressed as

$$P = \frac{1}{N}|H(x)|^2 \qquad\qquad 0 < f < \infty \tag{2.6}$$

which means the estimation of a PSD can be found by calculating the Discrete Fourier Transform (DFT)of a time series. However, before performing this calculation, it is found that the time series in this project (i.e., the temporal velocity field data) used as the inputs have a non-zero average. This average will show up in the resulting spectrum and may possibly have a low-frequency contribution. Hence, in the first step of calculating the PSD, the average is removed from the signal before starting the DFT processing by computing the average of the whole time series and subtracting that average from all data points.

In this work, the input data sequences used for the calculation of Power Spectral Density are the velocity components in different images taken for each case in the Taylor-Couette flow, which means the number of image is equal to 2047 for each case. Because

one image is a 2D data set, a series of images taken in a period of time could be treated as a 3D data set, where the third "axis" is time. In order to find the distribution of the power of each image over frequencies, which is the power spectral density, a three dimensional Fourier transform and a series of two dimensional inverse Fourier transforms of the data series should be done. For the calculation of PSD, all the velocity data at every vector position in the image series were normalized by the linear velocity of inner cylinder, subtracted the non-zero mean velocities, and loaded into the matrix. After zero padding the imaginary values into the data matrix which transform the data into a power of 2, a three dimensions Fourier transform based on the previous equation, Equation 2.5, and methodology was done for the whole data series. In order to find the power spectrum of each image in the frequency domain, a 2D inverse Fourier transform was performed in each image based on the 3D Fourier transform result. The total power spectrum in each image was then calculated using previous step results by applying Equation 2.6, which is ratio of the sum of the square of the value at every vector location for all three velocity components and vector numbers. Frequencies were defined using the image numbers and the time of image capturing, and then normalized by the angular velocity of the inner cylinder.

Results and Discussion

Figure 2.5 shows a sequence of six instantaneous velocity fields for R=6 (which falls within the laminar wavy vortex flow regime). The time interval between the vector fields in each of the sequences is $1.2s$. It can be seen that both the inflow and outflow boundaries in the WVF move periodically along the reactor axis, and the vortices expand and contract following the same cycle as the boundary movements due to the superimposed azimuthal waves on the toroidal vortices. The expansion and contraction of the middle vortex is made clear by the motion of the arrows indicating the position of outflow and

inflow boundaries. In addition to the expansion and contraction of the vortex, the vortex position which is shown by the center of the vortex also moves periodically along the axis. The expansion and contraction and the oscillation of the position of vortex are due to the effects of azimuthal waves superimposed on the flow. In Taylor vortex flow, Taylor vortices are time-independent toroidal vortices. Viscous forces dissipate the centrifugal force resulting from the circular motion. As the flow transiting to WVF, the azimuthal waves in the Taylor-Couette flow cause periodic motions of the inflow and outflow boundaries along the cylinder axis and the expansion and contraction of the vortices. The expansion and contraction are mainly due to fluid transfer between neighboring vortices due to the traveling azimuthal waves. When the fluid transfer is into the middle vortex from the two side vortices, the middle vortex expands, while the contraction is due to fluid transfer in the opposite way. The driving force of the circular motion overpowers the viscous force which leads to the complexity of WVF. Gollub and Swinney (1975) reported the similar findings, a periodic state occurring once Reynolds number rises above a critical value of relative Reynolds number, R^*=0.064 which is around Reynolds number of 160, in their experiment facility. Compard to Gollub and Swinney's work, the velocity fields presented in present work provide clear visualization of the wavy motions in the flow with the help of the PIV technique. Other researchers have also observed the same phenomenon. (Lueptow, 1992; Wereley and Lueptow, 1998, 1999; Takeda, 1999; Akonura and Lueptow, 2003). Since the critical value of R is highly dependent on the facility parameters, the Reynolds number of the onset of wavy vortex flow varies between experiments.

The power spectral density (PSD) calculated from the instantaneous velocity fields for R=6 is shown in Fig. 2.6. The sharp peak in the frequency component in the PSD is due to the periodic motion of the azimuthal waves passing the point of observation. This is confirmed by observing the sequence of instantaneous velocity fields and noting that the motion of the inflow and outflow boundaries occurs of the same frequency as this peak

in the PSD. The magnitude of this sharp frequency peak is a measure of the power of the waviness corresponding to the motion caused by the azimuthal waves. Peaks at this same frequency for other values of R in the WVF regime correspond to the presence of these same azimuthal waves. In Fig. 2.6, the total power spectral density is calculated based on all three velocity components, i.e. u, v, and w. The horizontal axis of the figure is the normalized frequency of the power spectral density, defined as the frequency over the angular velocity of inner cylinder at current Reynolds number, f/ω. This normalization makes it possible to identify similar features the PSD at different values of R. The peak magnitude is a relative magnitude in that all presents PSDs in this work are normalized by the maximum peak magnitude observed at R=6. As a result, the relative magnitude in Fig. 2.6 is 1.0, and the peak in the PSD at this frequency represents the motion induced by the azimuthal waves in the TC flow. There is a second smaller peak in Fig. 2.6 at a normalized frequency of 0.14 that represents that corresponds to the modulation observed in modulated wavy vortex flow. Compared to the primary peak in the figure, the magnitude of modulated wavy movement is less than 10 percents of the primary wavy movement. As a result, for R=6 the modulation is very weak, and the flow at this R appears as WVF. Previous researchers have also used power spectra to investigate WVF, such as Coles (1965), Takeda (1999), and Gollub and Swinney (1975). In these works, one single peak was observed in the power spectral density which indicates the same result in the present work represented the WVF regime. However, the power spectra in the previous studies were mostly calculated using only one velocity component of the Taylor-Couette flow. In the present work, the power spectral density is calculated using all three velocity components, which is helpful in the capturing of traveling azimuthal waves and the identification of different flow regimes, especially for MWVF as will be discussed later. Just as was mentioned for the previous figure, the Reynolds number of the onset of WVF varies based on different experiment facilities, and leads to different peak frequency of the peak observed in the power spectral density.

As Reynolds number is increased to R=11, it can be seen in the instantaneous velocity fields (Figure 2.7) that the inflow and outflow boundaries still move periodically along the reactor axis, and expansions and contractions of vortex also follow the same cycle as was observed at R=6. However, the periodic motion of the inflow and outflow boundaries appears to be relatively weaker than at the lower Reynolds number. This suggests that the superimposed azimuthal waviness still play an important role at R=11, but the azimuthal waves and wavy motion are becoming weaker than at R=6. As can be seen in the PSD (Fig. 2.8) at R=11, there is still one dominant peak in the PSD. However, the relative magnitude of the dominant peak is less than half of the magnitude observed at R=6. Thus, the PSD also shows that the wavy motion at R=11 is weaker than the wavy motion at R=6 which corresponds to the result observed in Fig. 2.7. The normalized frequency of the dominant peak is same as the normalized frequency found at R=6. Since the frequency of the peak represents the frequency of the azimuthal wave motion in the flow, the normalized same peak frequency observed at different Reynolds numbers indicates that same fundamental instability is responsible for the azimuthal waves observed at the different Reynolds numbers. A second peak can also be seen in the Fig. 2.8. Compared to the second peak, primary peak is still more than 7 times larger than the secondary one indicating that the TC flow at R=11 is still primarily in the regime WVF. However, modulated wavy motion is becoming more significant as R increases. Note that just as for the primary peak, the normalized magnitude of the secondary peak also becomes smaller with the increasing of Reynolds number. However, the ratio of primary to secondary peak strength becomes *relatively* more significant. This trend of weaker azimuthal waves was also observed and reported by other researchers. (Lueptow, 1992; Wereley and Loeptow, 1998, 1999; Takeda, 1999; Andereck et al., 1986; Wang et al., 2005). In these investigations, WVF , MWVF, and the transition between the flow regimes were of primary interest. Wavy motion intensity in WVF was briefly reported in the analysis of the power spectrum. However, the visualization of the disap-

pearance of wavy motion with increasing the Reynolds number in Taylor-Couette flow, as in the present work, were lacking in the previous investigations. The mechanism of this reduced strength of wavy motion was not determined in the previous work. Since the wavy motion originates from the balance of viscous force and centrifugal force, one could would assume that this balance of forces varies as the Reynolds number increases leading to variations in the axial flow and azimuthal flow and result in the weakening of traveling azimuthal waves.

Figure 2.9 shows a sequence of six instantaneous velocity vector fields for R=15. It can be seen in the figure that the inflow and outflow boundaries and the center of the vortex still move along the reactor axis, and there are still expansion and contraction of the vortex. However, the boundary motion vortex expansion and contraction are even weaker than those observed in the instantaneous velocity fields at R=11. This indicates that while there are still traveling azimuthal waves at this Reynolds number, the influence of traveling azimuthal waves is much smaller than before and the wavy vortex flow appears to be disappearing. The PSD shows the same trends as the velocity fields (Fig. 2.10). There is one dominant peak with the same normalized frequency as in the previous Reynolds numbers, and this peak represents the same traveling azimuthal waves superimposed upon the Taylor-Couette flow. At R=15 the flow is still in the WVF regime, but the relative magnitude of the primary peak is only about two-thirds of the magnitude of the primary peak at R=11 illustrating that the wavy motion observed at this Reynolds number is weaker and the flow is undergoing the same weakening of the WVF that was observed when R was increased from 6 to 11. The relative magnitude of the secondary peak also further decreased with increasing Reynolds number, (indeed, the secondary peak has nearly disappeared) meaning that both azimuthal wavy motion and modulated wavy motion are disappearing with increasing Reynolds number.

A sequence of six instantaneous velocity fields for R=17 is shown in Fig. 2.11. The locations of the inflow and outflow boundaries and the vortex centers remain nearly

constant over this sequence of velocity fields, and the vortex contraction and expansion have virtually disappeared. This suggests that traveling azimuthal waves have weakened to the point of having a negligible effect on the Taylor vortices. This feature is also observed in the power spectral density at R=17. In Fig. 2.12, the axis of relative magnitude of the PSD has been scaled down in order to see the power at this R clearly. It can be seen in the figure that the relative magnitude of the peak at the normalized frequency corresponding to the wavy motion is less than four percent of the primary peak magnitude that was observed at R=6 indicates that for R=17, the wavy motion has all but disappeared since the peak at the normalized frequency corresponding to the azimuthal waves is just above the background noise. Also, the same feature is observed in the secondary peak corresponding to the modulation. Its normalized value is less than 0.02 at R=17.

In Figs. 2.13 through 2.16, contour plots of the azimuthal velocities for R=6, 11, 15, and 17 are presented. It can be seen in the contour plots that vortex center moves periodically which agrees with the results in both instantaneous velocity fields and PSD, and similar results to those previously observed can be seen in the expansion and contraction of the vortexes in the figures. As the relative Reynolds number R increases from 6 to 17, the amplitude of oscillation of the vortex decreases. At R=17, the shapes of the contour plots are almost unchanged with time, indicating that the periodic behavior associated with the presence of azimuthal waves is nearly absent.

Fig. 2.17 and 2.18 represent the first and second peak in the PSD at different Reynolds numbers from 6 through 17. The vertical axis is still the relative magnitude which is normalized by the maximum peak magnitude observed at R=6. It can be seen in Fig. 2.17, that the relative magnitude of the dominant peak decreases with the increasing of Reynolds number before reaching the minimum, R=17. The wavy motion induced by the azimuthal wave becomes weaker and disappears when R increases from 6 to 17. Same trend can be found in Fig. 2.18 for the second peak in the PSD at different Reynolds

numbers. The relative magnitude of the second peak decreases which represents the modulated wavy motion disappears in the Taylor-Couette flow. As shown in the figures, the comparison between the relative magnitude of the second peaks and the first peaks proves that the WVF dominates the flow.

As the Reynolds number of the Taylor-Couette flow increases, the wavy motion that was observed to decrease and reach a minimum at R=17 may be expected to remain small at higher R. However, Fig. 2.20, which represents the PSD at R=19, shows a sudden rise in the relative magnitude of a peak at a normalized frequency of 0.15, which is the frequency observed that corresponded to wave modulation. To allow for easy comparison with the peak observed at a normalized frequency of 0.05 at lower R, the magnitude of this 0.15 peak is also normalized by the magnitude of the primary peak observed at R=6. It can be observed in Fig. 2.20 that the peak at the 0.05 normalized frequency remains small as the Reynolds number increased to 19 while the peak at the frequency representing modulated wavy motion is now the larger peak. The appearance of this new primary peak at higher frequency indicates the reappearance of azimuthal waves at R=19, but at a higher frequency than observed at lower R. Figure 2.19 shows a sequence of six instantaneous velocity vector fields at R=19. It can be seen that the inflow and outflow boundaries once again move (although the motion is small) and the center of vortices also move in the same cycle as the boundaries. The movements are due to the reappearance of the azimuthal waves in the Taylor-Couette flow with a normalized frequency of 0.15. This reappearance of the traveling azimuthal waves was first reported by Walden and Donnelly (1979). In their research, the reappeared azimuthal waves were found in a power spectrum analysis of velocity data. They briefly reported on the reappearance without any specific investigation and argued that the reappearance only occurred in large aspect ratio reactors. The work of Takeda (1999) was the first detailed investigation of the reappearance of azimuthal waves. In Takeda's experiments, the reactor had a relatively short aspect ratio, below the threshold reported

by Walden and Donnelly, and experimental data were analyzed using Fourier and proper orthogonal decomposition. Takeda reported the reappearance of a frequency peak in Fourier analysis at R=23 after the disappearance of this flow mode at R=21. Since the experiment facilities in present work are different from Takeda's experiments, the Reynolds number is expected to be different. However, the range of disappearance and reappearance of the traveling azimuthal waves in the present work agrees with Takeda's results. Furthermore, since the experimental results in the present work are collected by high speed PIV with high speed cameras, velocity fields which are capable of capturing the weak wavy motion of the reappeared azimuthal waves can provide good visualization of the reappearance in addition to the power spectrum analysis.

At R=21, a sequence of instantaneous velocity fields are shown in Fig. 2.21, and the inflow and outflow boundaries near periodic movements and expansion and contraction of the vortex can still be observed, even though they are weaker than all previous results. This indicates the reappeared azimuthal waves are still present in the Taylor-Couette flowat this Reynolds number. Figure 2.22 is the PSD result for the flow at R=21. In this figure, the relative magnitude of this new primary weak peak decreases from 0.08 to 0.04 as the Reynolds number increases from 19 to 21. This follows the previous observations at lower R that the wavy motion decreases as R is increased.

Figure 2.23 shows a sequence of instantaneous velocity fields at R=24. Unlike at R=19 and 21, there is hardly any movements can be observed in the vortex boundaries or center. The inflow and outflow boundaries of the vortex stay nearly fixed in one position, and the vortex size does not vary over time. These results suggest that the reappeared azimuthal waves are in the process of disappearing again in the Taylor-Couette flow. In the PSD result shown in Fig. 2.24, the relative magnitude of the reemerged peak at a normalized frequency of 0.15 has dropped to 0.02, which is a further indication of the decay of the reemerged azimuthal waves in the flow. This also corresponds to the finding in Fig. 2.23.

As the Reynolds number increases further, the wavy motions continues to decay in the Taylor-Couette flow. Figure 2.25 is a sequence of instantaneous velocity fields at R=30. In this figure, no periodic movements of inflow and outflow boundaries or the Taylor vortices are observed. However, small scale turbulent structures appear in the velocity field which represents the Taylor-Couette flow transiting to turbulence. In Fig. 2.26, which is the PSD result at R=30, the magnitude of the peak of a normalized frequency of 0.15 is no longer present indicating that the reemerged azimuthal waves have disappeared.

Summary and Conclusion

In the Taylor-Couette reactor described in this work, the presence and characteristics of azimuthal waves were investigated over a range of Reynolds numbers spanning the wavy vortex regime, the modulated wavy vortex regime, and the transition to turbulence. These regimes were studied using stereo PIV to obtain time-resolved three-component velocity field data in a meridional plane of a device and the application of a Power Spectral Density analysis method to the collected velocity fields.

The Wavy Vortex flow and Modulated Wavy Vortex flow regimes were characterized by travelling azimuthal waves. As the flow underwent transition from laminar WVF to MWVF then TTVF, the azimuthal waves were observed to first weaken, then disappear, and then reappear again at a higher frequency. In the power spectral density analysis, power spectra obtained at a fixed position for a WVF shows an isolated primary peak which corresponds to the oscillations caused by this azimuthal wave. A second weak peak appears in the power spectral which can be attributed to a modulated frequency of the fundamental azimuthal wave. As the flow began to transition to TTVF no obvious peak dominated in the power spectral and there was a rise in the background "noise" level, indicating a broadband transition to turbulence. It was difficult to observe the

modulated wavy vortex flow in this reactor by visual observation of the flow or in the PIV velocity data, a phenomenon which has also been noted in other studies (Takeda et al., 1994; Wereley and Lueptow, 1994; Wang et al., 2005). However, using the power spectral density analysis method, one can detect the MWVF by observing the secondary peak in power spectral density function. Thus, it was found that the power spectral density analysis described here is an efficient and valid method for investigating flow transitions in Taylor Couette flow.

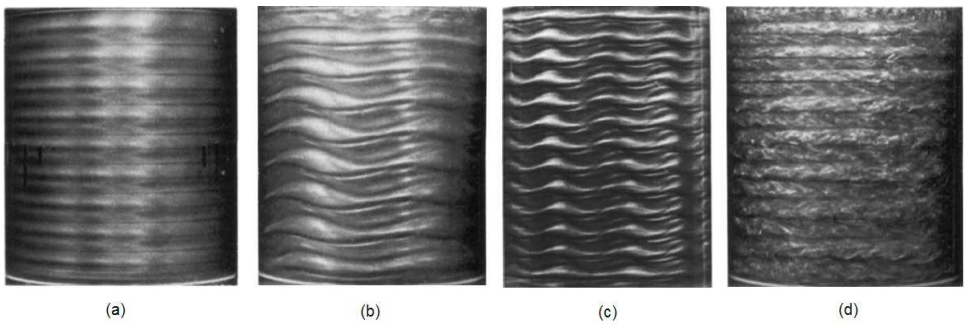

Figure 2.1 Example flow regimes of Taylor-Couette flow: (a) TVF (b) WVF (c) MWVF (d) TTVF (Fenstermacher et al., 1979)

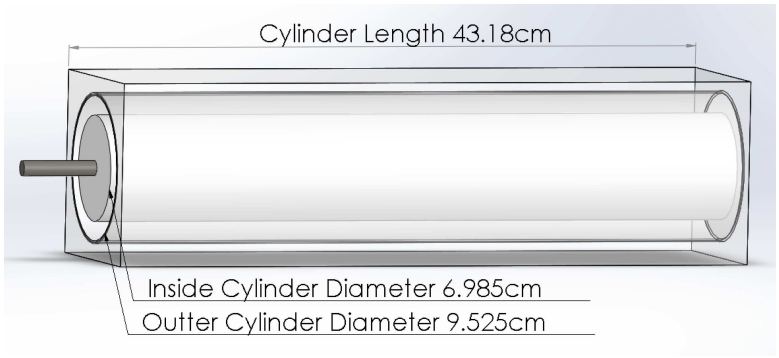

Figure 2.2 Apparatus of experiment: Cylinder Length: 43.18cm; Inside Cylinder Diameter: 6.985cm; Outside Cylinder Diameter: 9.525cm

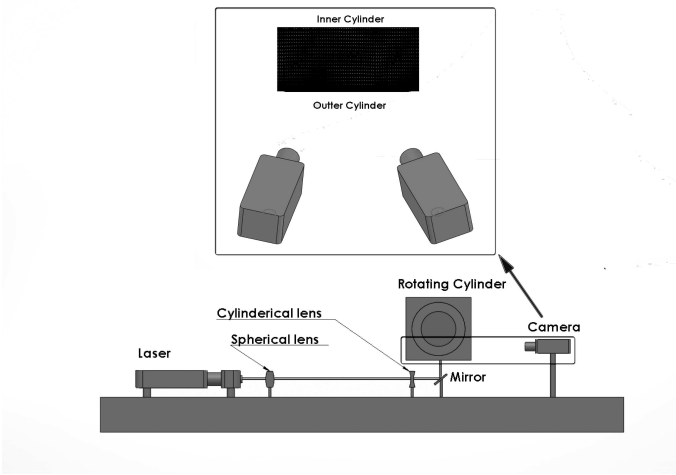

Figure 2.3 Schematic of experiment setup

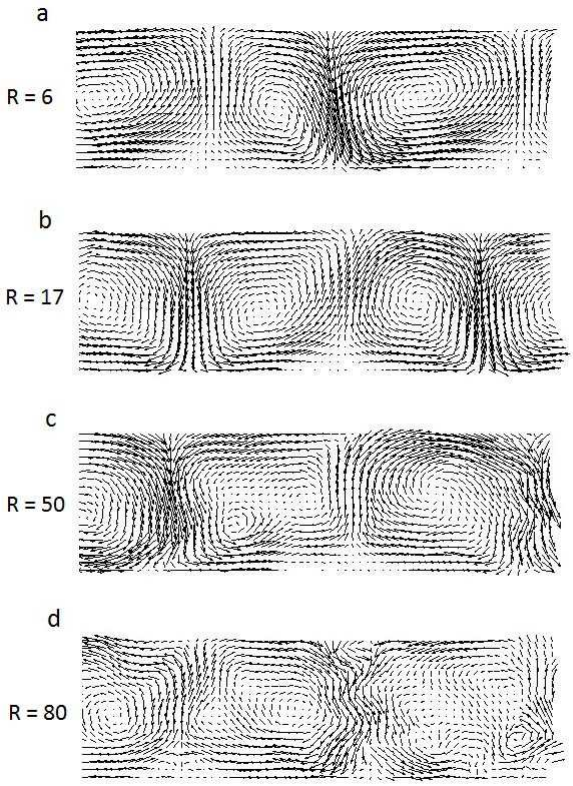

Figure 2.4 Example of PIV velocity fields

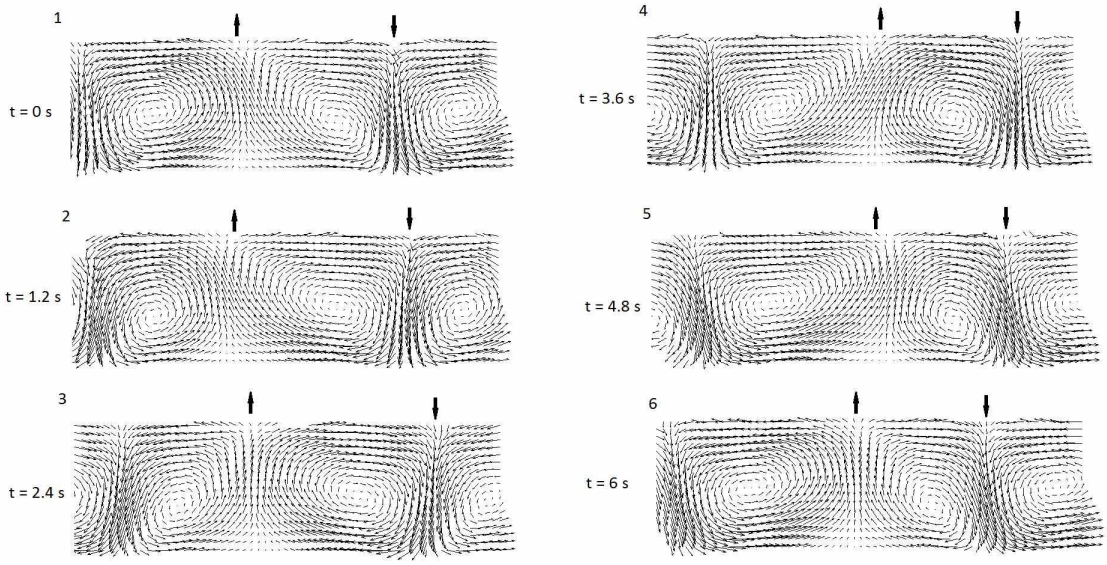

Figure 2.5 PIV velocity fields for R=6

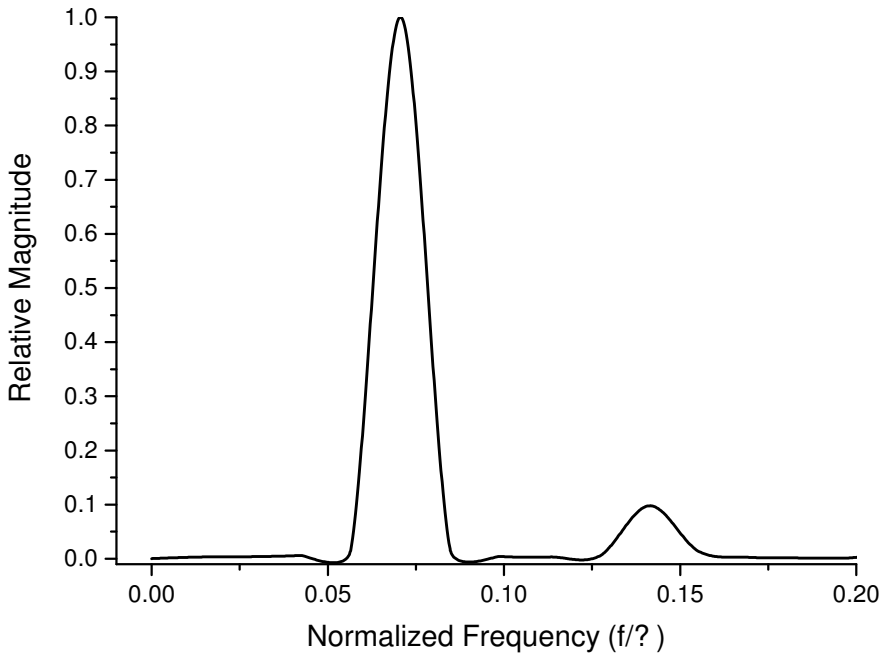

Figure 2.6 Power Spectral Density for R=6

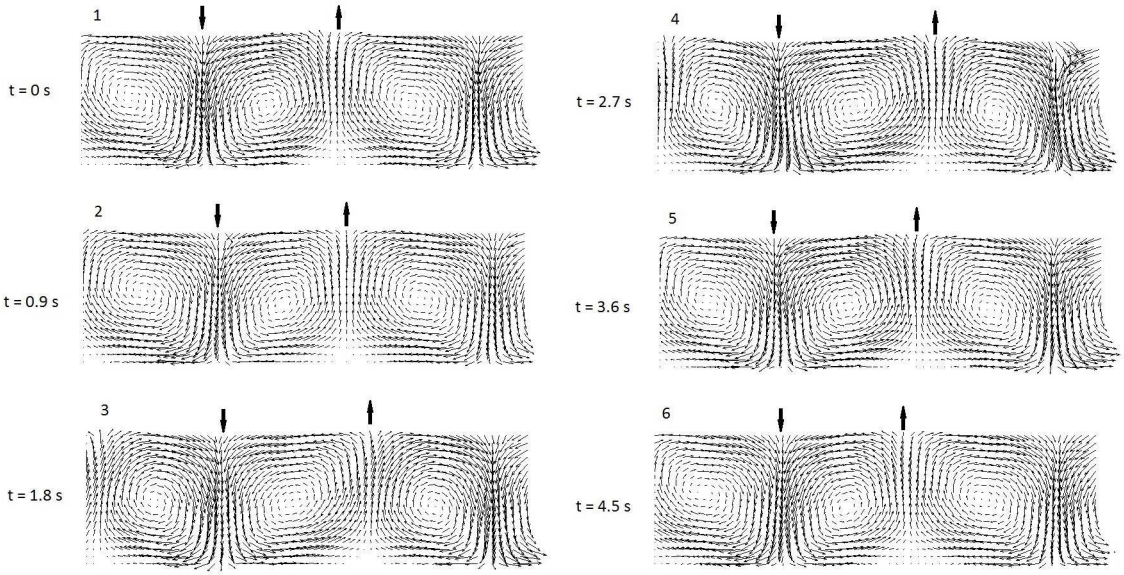

Figure 2.7 PIV velocity fields for R=11

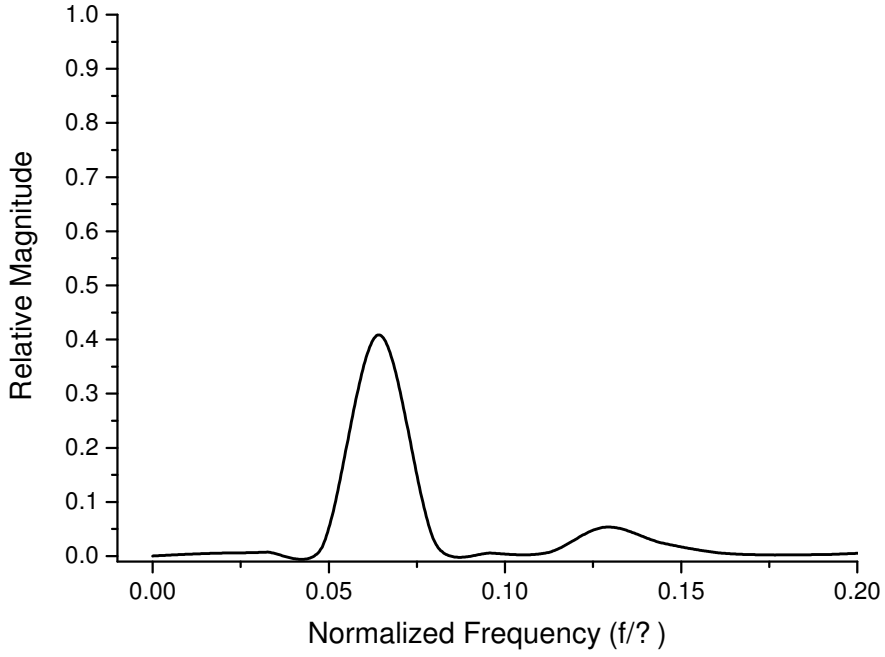

Figure 2.8 Power Spectral Density for R=11

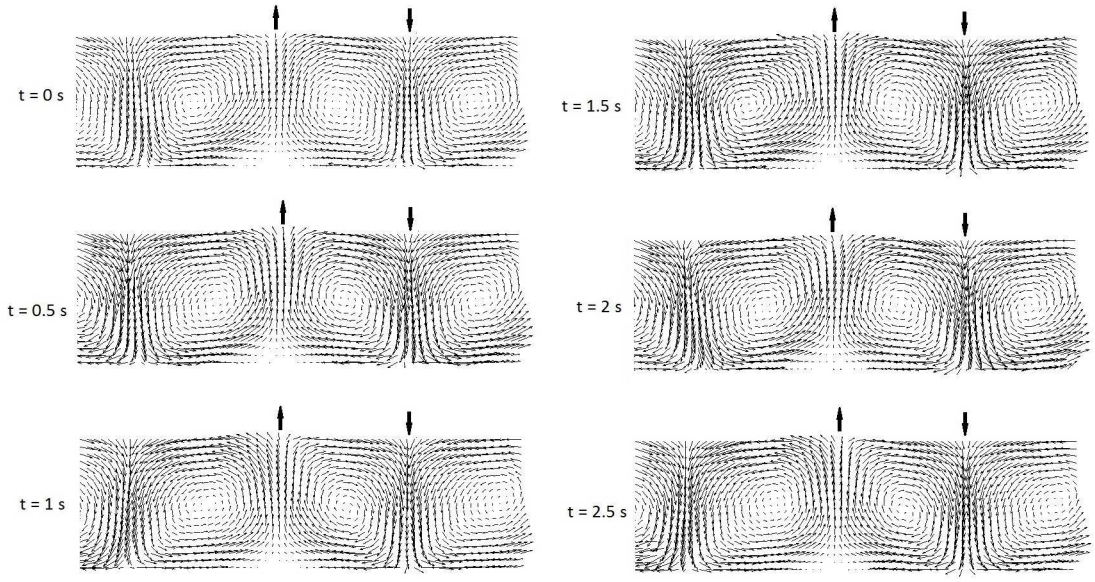

Figure 2.9 PIV velocity fields for R=15

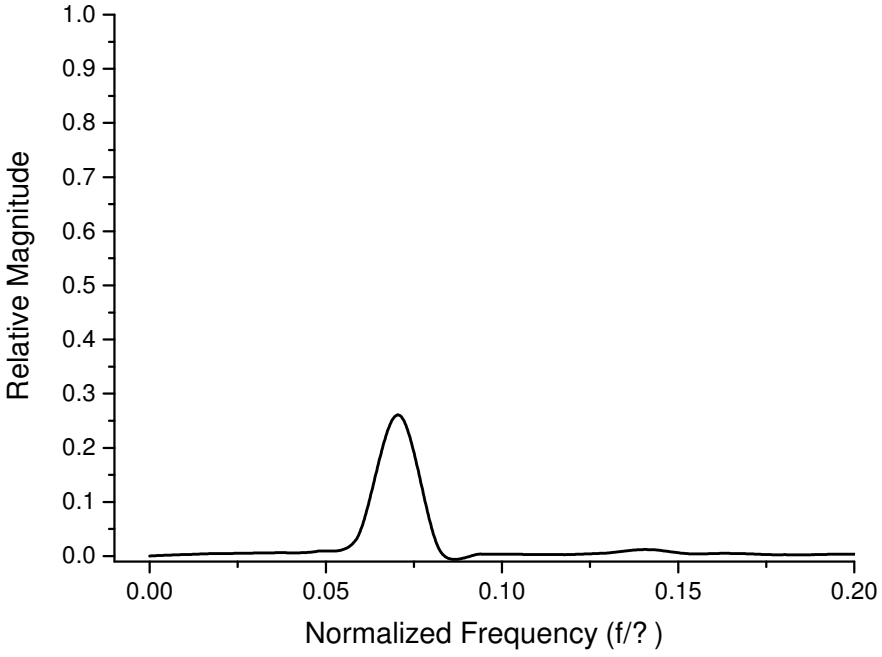

Figure 2.10 Power Spectral Density for R=15

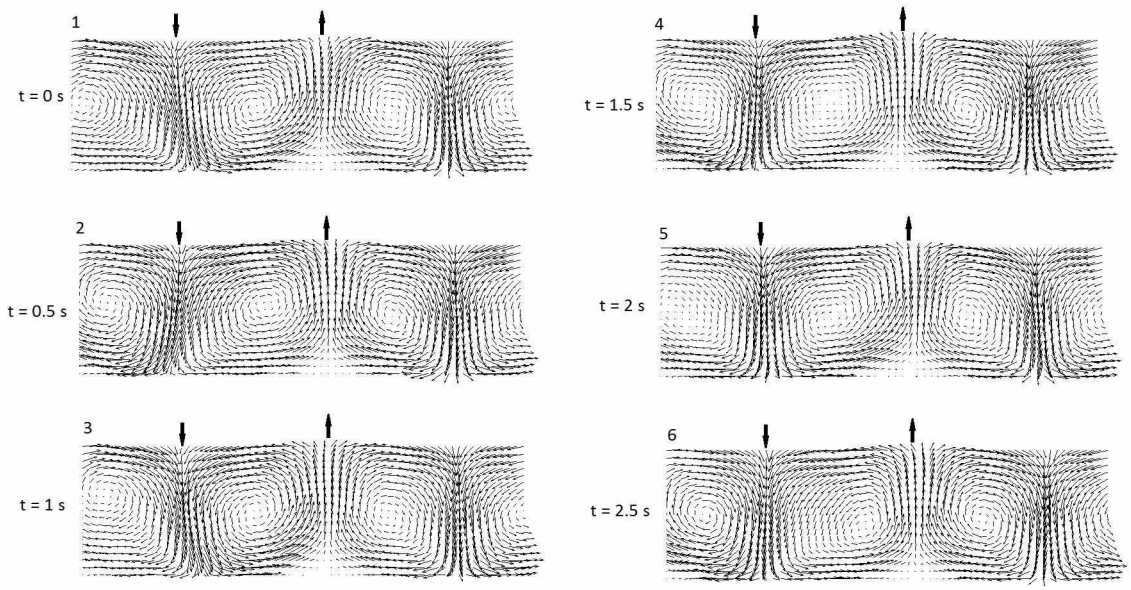

Figure 2.11 PIV velocity fields for R=17

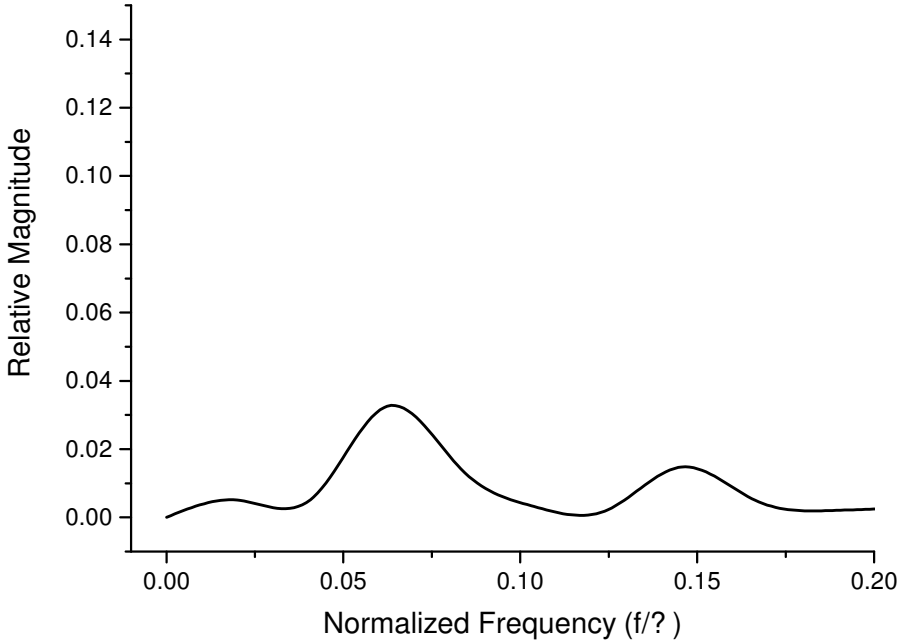

Figure 2.12 Power Spectral Density for R=17

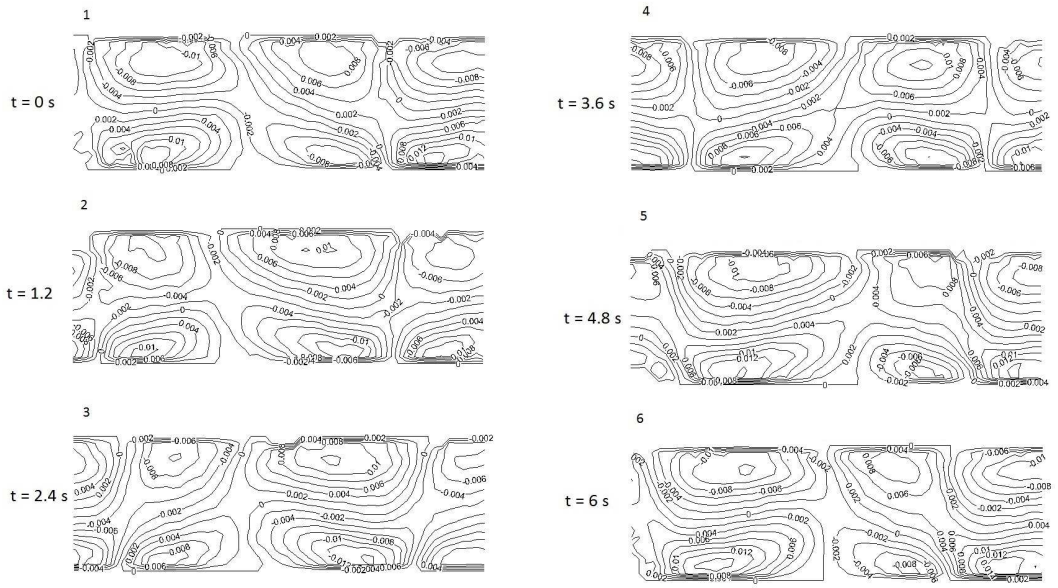

Figure 2.13 Contour plot of axial velocity for R=6

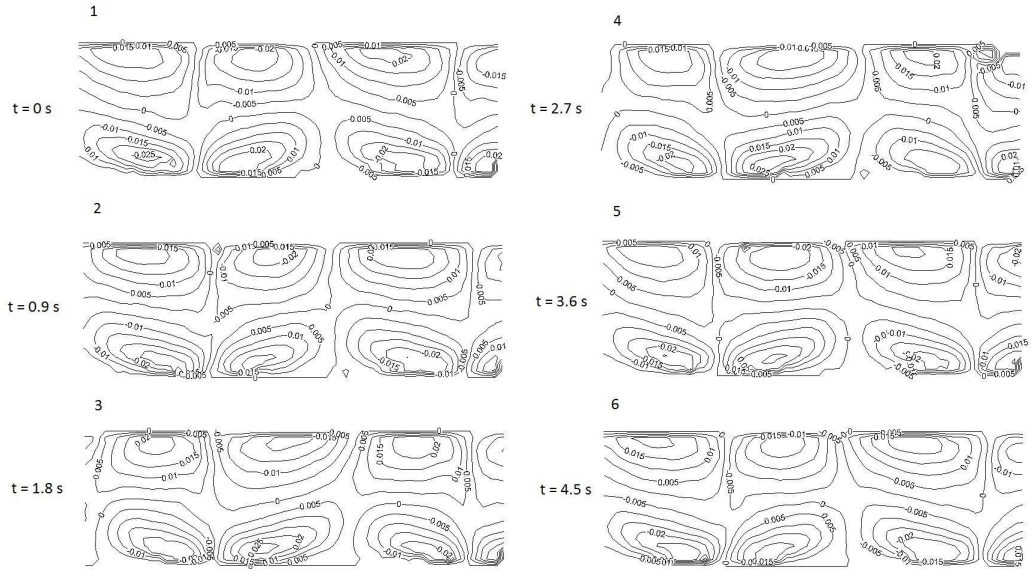

Figure 2.14 Contour plot of axial velocity for R=11

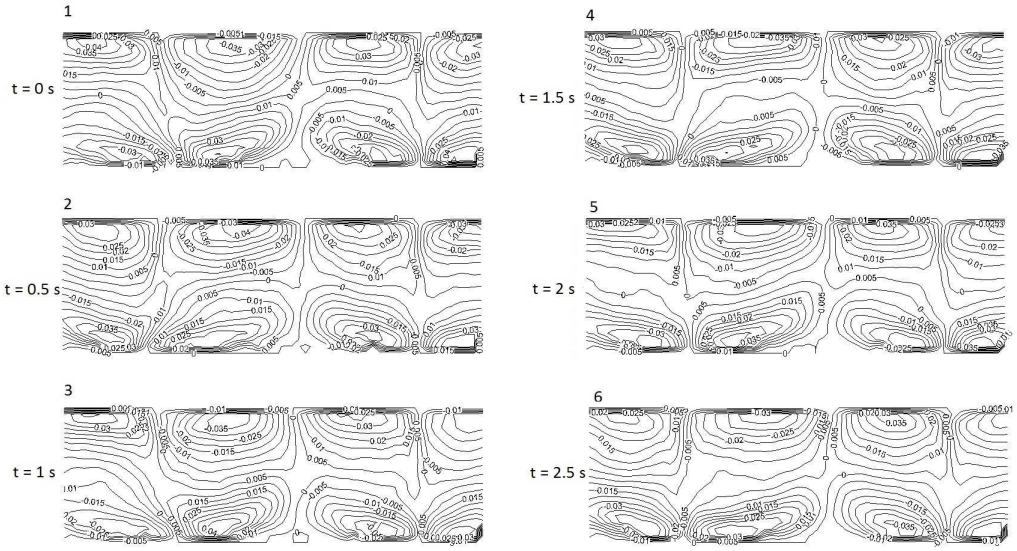

Figure 2.15 Contour plot of axial velocity for R=15

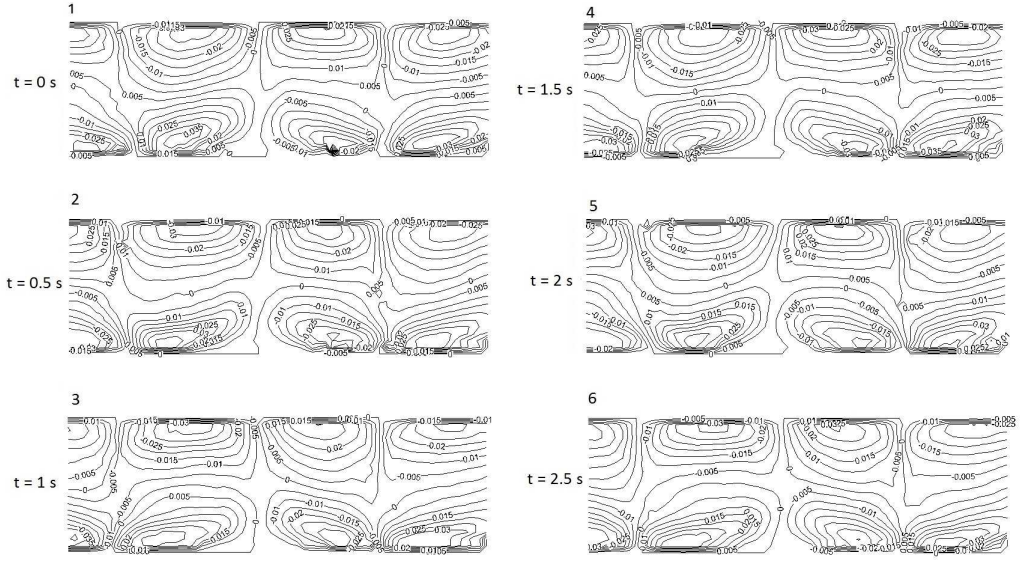

Figure 2.16 Contour plot of axial velocity for R=17

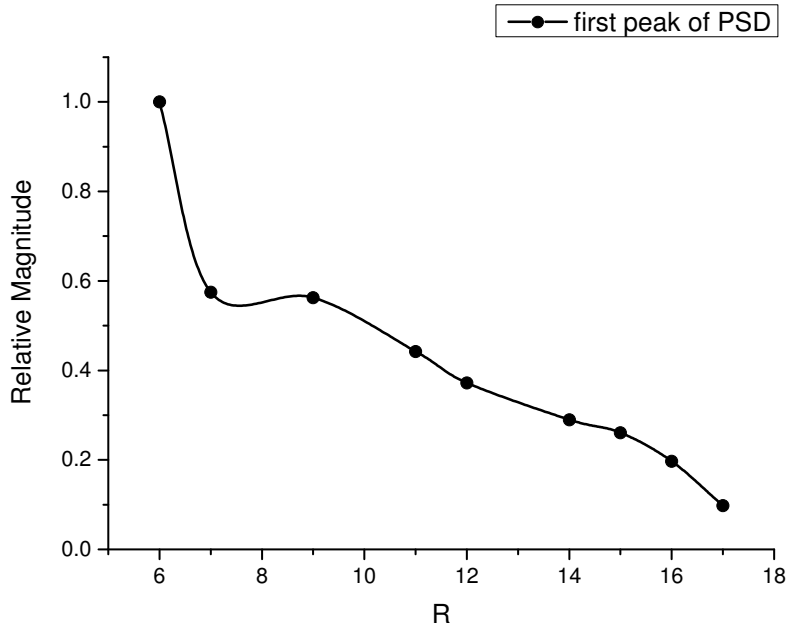

Figure 2.17 First Peak in PSD of R from 6 through 17

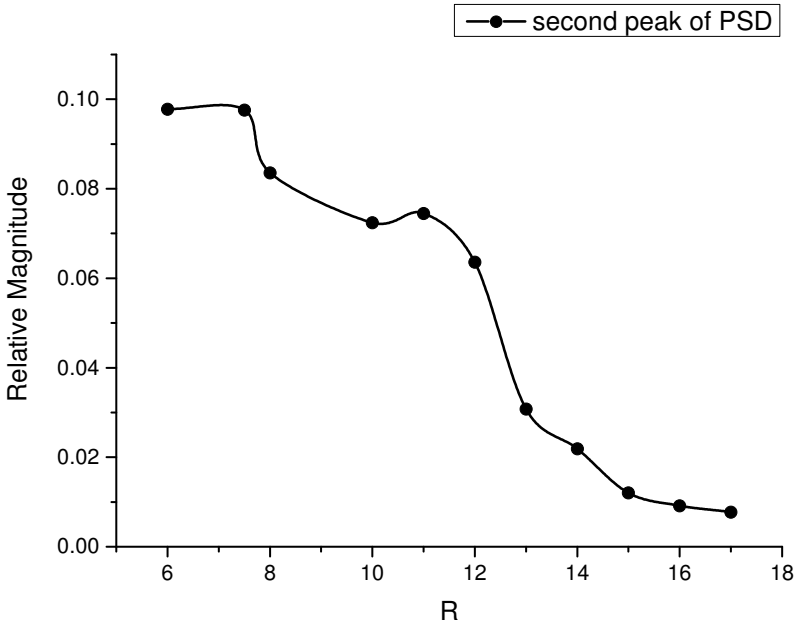

Figure 2.18 Second Peak in PSD of R from 6 through 17

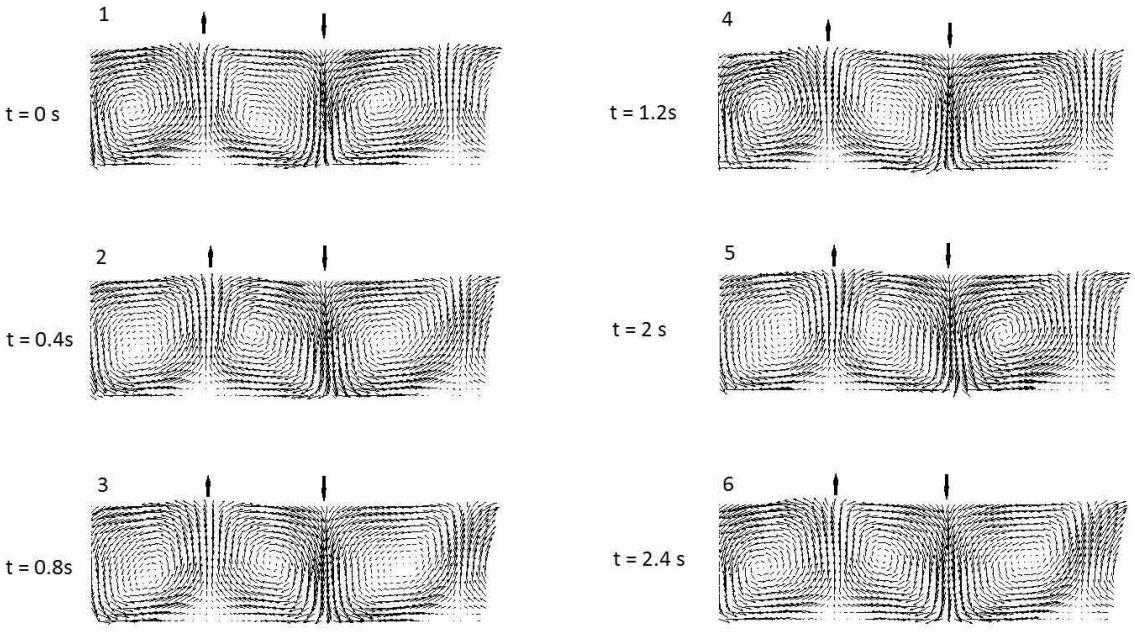

Figure 2.19 PIV velocity fields for R=19

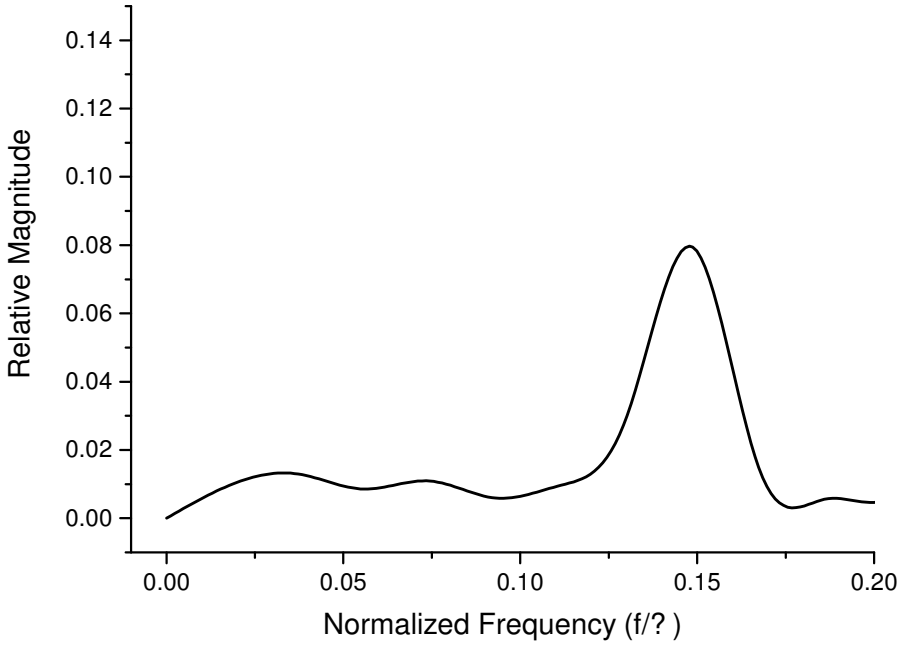

Figure 2.20 Power Spectral Density for R=19

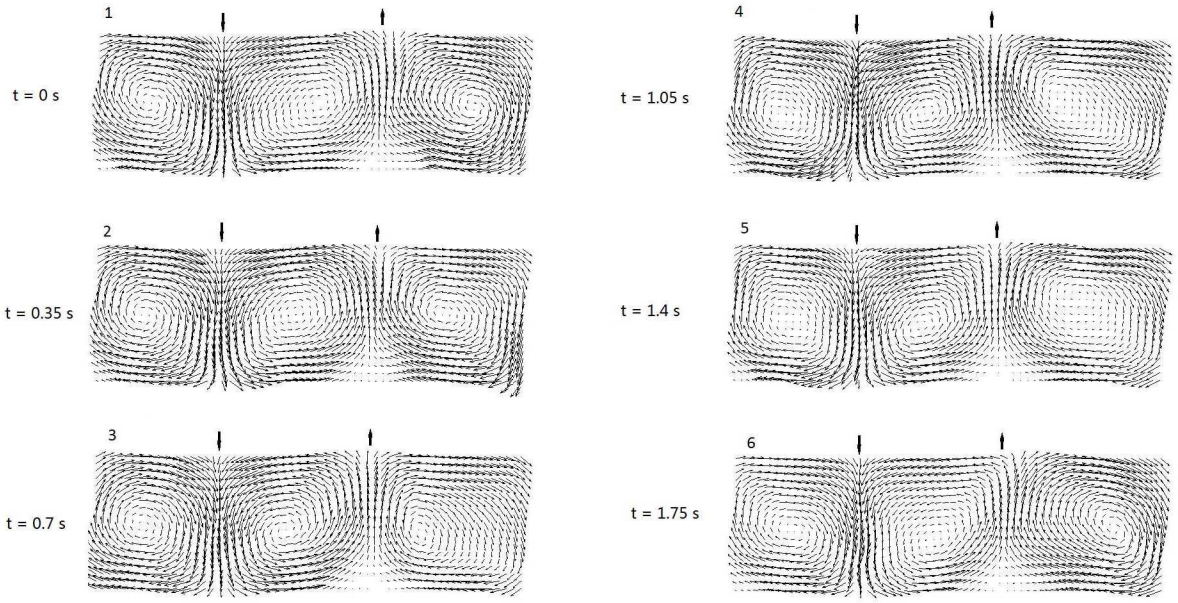

Figure 2.21 PIV velocity fields for R=21

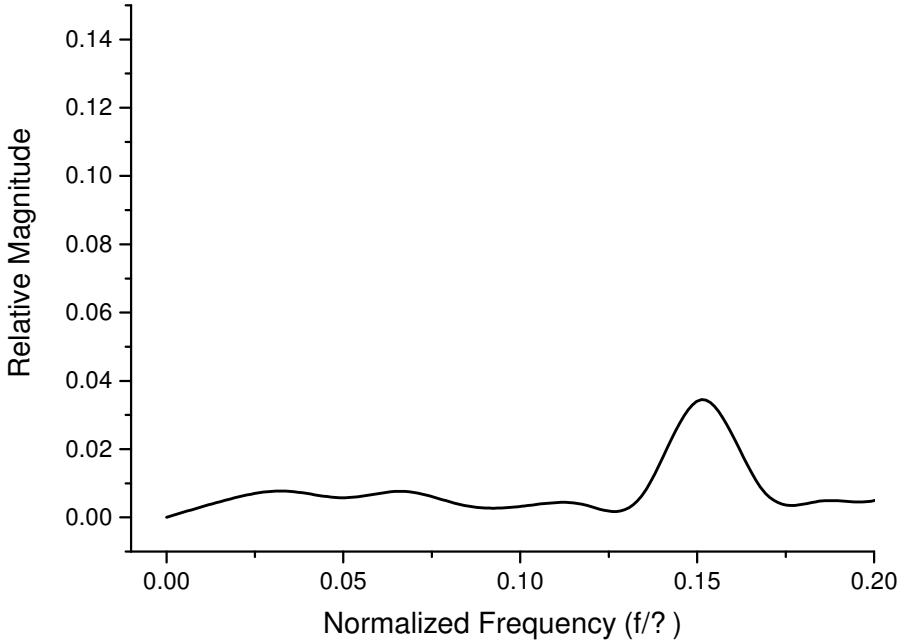

Figure 2.22 Power Spectral Density for R=21

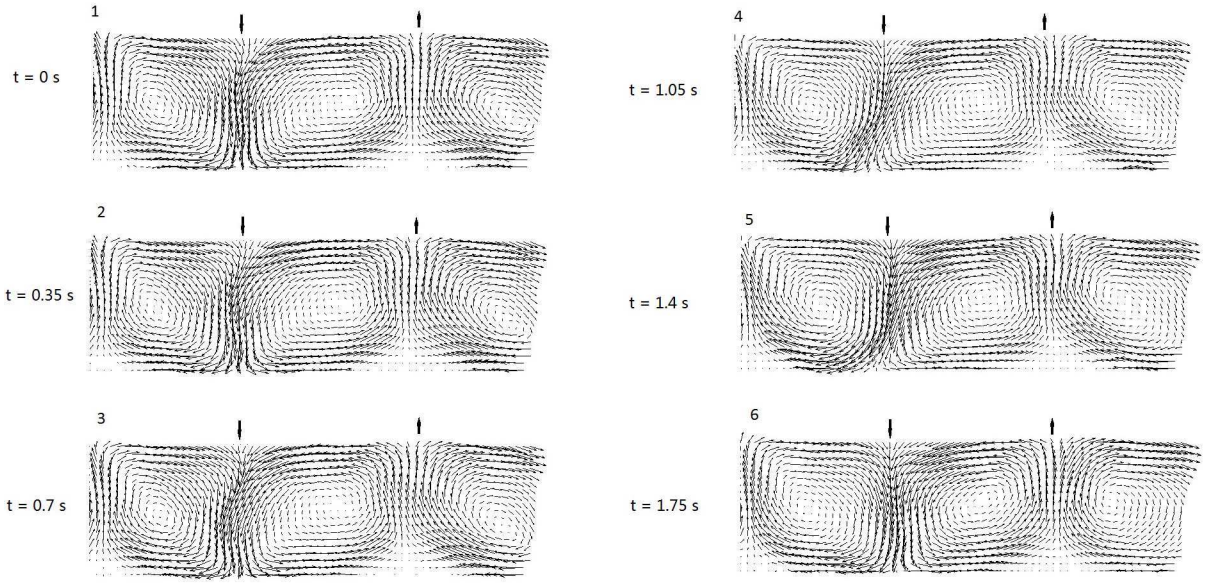

Figure 2.23 PIV velocity fields for R=24

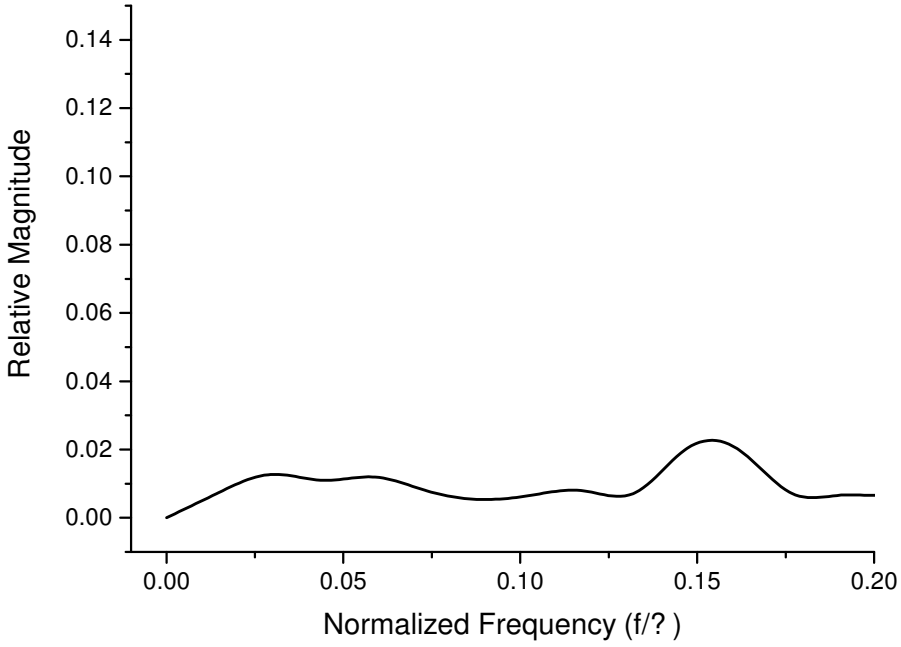

Figure 2.24 Power Spectral Density for R=24

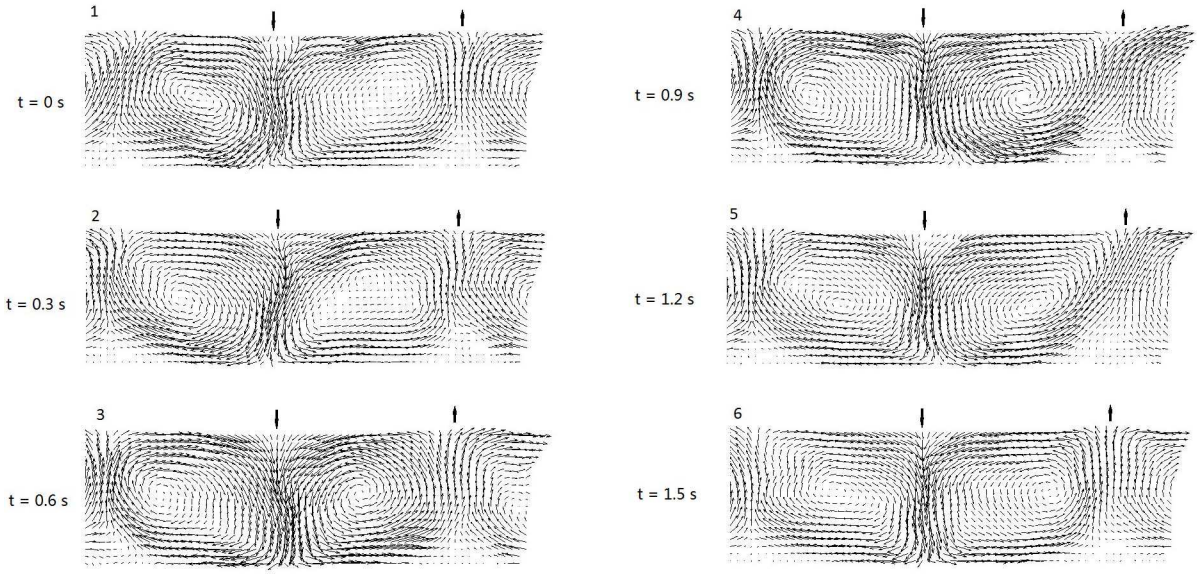

Figure 2.25 PIV velocity fields for R=30

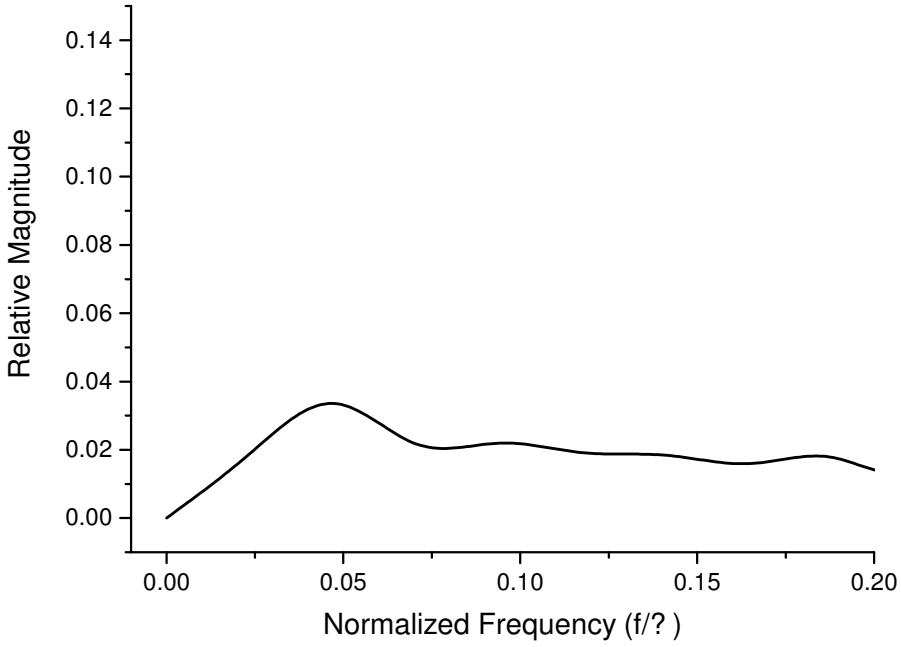

Figure 2.26 Power Spectral Density for R=30

CHAPTER 3. NUMERICAL INVESTIGATION OF TAYLOR-COUETTE FLOW WITH $k-\varepsilon$ MODEL

A paper in preparation

Abstract

Unsteady Reynolds-averaged Navier-Stokes (RANS) simulation were performed over a range of Reynolds numbers for a Taylor-Couette flow with the fixed outer cylinder and rotating inner cylinder and compared in detail with stereoscopic particle image velocimetry (PIV) measurements. A finite-volume Computational Fluid Dynamics (CFD) library, OpenFOAM, was used to discretize and solve the filtered Navier-Stokes equation. The effects of grid resolution on the results of the RANS simulation using the k-ε turbulence model results were investigated for both 2D and 3D computational grids. Model validation was performed by comparing RANS results for velocity statistics such as the axial, radial, and azimuthal velocities and turbulent kinetic energy with the stereo PIV data. In addition, the power spectral density (PSD) of the RANS simulation were computed and compared with PIV data to determine if the unsteady RANS simulations could capture the instabilities and periodic motions due to that instabilities. Excellent agreement was observed leading to the conclusion that the RANS with k-ε model accurately captures the important characteristics of all the turbulent and unsteady features present in the Taylor-Couette flow. The 2D and 3D simulations yield similar results, suggesting the 2D simulation provides a precise and and economical method for simulating the turbulent Taylor-Couette flow.

Introduction

Couette flow was first investigated in the viscosity research of Mourice Couette (1890). Later, in 1923, Geoffrey I. Taylor discovered and described the cellular motion that develops with the rotation of the cylinder. A fluid which is confined between two concentric cylinders with inner and perhaps the outer cylinder rotating along the concentric axis is called Taylor-Couette flow. Taylor-Couette flow is a classic and important flow in fluid mechanics and has been studied for more than a hundred years. For a fixed outer cylinder, the flow undergoes a series of transitions from purely laminar flow, to vortex flow, to turbulent vortex flow as the inner cylinder increases rotation velocity from rest. The behavior of a Newtonian fluid confined in the annulus can be characterized by the rotational Reynolds number.

$$Re = \frac{\omega r_i \left(r_i - r_o\right)}{\nu} \tag{3.1}$$

where ω is the inner cylinder angular velocity, r_i and r_o are the radii of the inner and outer cylinders, respectively, and ν is the kinematic viscosity of the fluid.

As a canonical flow in fluid mechanics, Taylor-Couette flow has been studied widely by many researchers. As the rotation velocity of inner cylinder increases pass a critical value, the laminar flow between the gap of inner and outer cylinder develops a series of instabilities. For low Reynolds numbers, the flow which develops is called Taylor vortex flow (TVF) and has time-independent and axisymmetric vortices. If the Reynolds number is increased above a critical value, the vortices in the flow begin to oscillate in position, size, and shape due to the emergence of azimuthal waves and the flow becomes Wavy vortex flow (WVF). Based on spectral analysis, this state can be described by one temporal frequency (Coles, 1965; Andereck et al., 1986). The value of the Reynolds number at this critical value of the rotation velocity is defined as Re_c, where Re_c depends on the radius ratio of the cylinders, η. In this paper, all the Reynolds numbers presented are the relative Reynolds number, which is defined as the ratio of actual Reynolds number

to the critical Reynolds number, $R = Re/Re_c$. When the Reynolds number is increased further, the flow turns transitions to modulated Wavy vortex flow (MWVF). MWF still involves non-axisymmetric vortices, but vortices are described by two temporal frequencies (Gorman and Swinney, 1982; Swinney, 1983; Andereck et al., 1986). As the Reynolds number is further increased, non-periodic spatial structure appears in the flow, and the flow states in the Taylor-Couette flow transition to chaotic wavy vortex flow (CWF) (Brandstater and Swinney, 1987)and then finally turbulent Taylor vortex flow (TTVF) (Gollub and Swinney, 1975). In the turbulent regime, power spectral density analysis on Taylor vortex flow has some limitations due to a broadband spectrum in the PSD representing the turbulent nature of the flow making it difficult to isolations due to wavy motion.

Computational Fluid Dynamics (CFD) is the analysis of systems involving fluid flow, heat transfer and associated phenomena such as chemical reactions by means of computer-based simulation. The technique is very powerful and spans a wide range of industrial and non-industrial application areas. CFD has been developed and widely used in the investigation of turbulent flow in the recent decades. Different techniques have been developed for simulating turbulent flows, including Direct Numerical Simulation (DNS), Large Eddy Simulation (LES), and Reynolds-averaged Navier-Stokes (RANS) simulation. DNS is the most accurate method in which the turbulence is not modeled at all, but it is prohibitively very expensive. In LES, only the smallest scales of turbulence are modeled, which can reduce computational costs; however, LES is still computationally expensive. Reynolds-averaged Navier-Stokes (RANS) simulations model all of the turbulence, making them the least expensive. However, the accuracy of RANS models must be validated when it is applied. In the present study, we seek to investigate the accuracy of using RANS to model this Taylor-Couette flow over a large range of Reynolds numbers. Both 2D and 3D unsteady RANS simulations are investigated, and compared with stereo PIV results.

Compared quantities include mean velocities and turbulent kinetic energies. A PSD analysis is also performed to determine if the RANS simulations can capture the instabilities that cause the azimuthal waves to appear in the flow.

Experimental Section

Experiment Apparatus

The inner cylinder of the Taylor-Couette reactor in present work had a diameter of $6.985cm$ while the outer cylinder had a diameter of $9.525cm$, resulting in an annular gap width between the cylinders of $1.27cm$. Both cylinders were made of Plexiglas, and the outer cylinder was enclosed in a square Plexiglas box. The length of the cylinders was $43.2cm$. The inner cylinder was driven by a compumotor control system with digital controller.

The working fluid in the apparatus was a mixture which had its refractive index matched with that of the Plexiglas (1.4905). The mixture contained water (90% by volume) and glycerol (10% by volume) with sodium iodide and small quantities of sodium thiosulfate. The mixture was created by beginning with a saturated solution of sodium iodide in water and glycerin until the index of refraction matched that of water. Silver-coated hollow glass spheres with a density of 1.6 g/cm^3 and an average diameter of 13 μm were used as the PIV seed particles. The density of working fluid was 1.85 g/cm^3, and the viscosity of the working fluid was $1.71\times\ 10^{-6}\ m^2/\text{s}$. For this apparatus, the critical value of Reynolds number was $Re_c = 99.53$.

PIV Measurement

The PIV system used in present work was a Lavison Inc. high speed stereoscopic PIV system. A thin laser sheet which was formed by the combination of spherical plano-convex lens and cylindrical planoconcave lens was reflected by a mirror and then passed

through the outer cylinder to illuminate a thin region of the annulus. The laser sheet was carefully aligned in the meridional plane to avoid a possible anomalous apparent radial velocity component caused by the azimuthal path of the particles through the laser sheet. The images were captured in the illuminated plane at the different investigate Reynolds numbers, and the images measured 1024 pixels axially and 1024 pixels radially. An interrogation region of 32×32 pixel with 50% overlap between adjacent interrogation regions was used to calculate the velocity vectors in the images resulting in an in-plane velocity vector spacing of $0.4mm$.

At the beginning of each experimental measurement, the inner cylinder was accelerated from rest to $R = 55$ at a constant angular acceleration of $0.314rad/s^2$. The inner cylinder angular velocity was maintained constant at this velocity for half an hour before increasing to higher velocity at a constant angular acceleration of $0.314rad/s^2$ or reducing to a lower velocity at a constant angular acceleration of $0.126rad/s^2$. In order to ensure the number of vortices had maintained a steady state, the inner cylinder was maintained at the desired angular velocity for approximately 10 minutes before PIV data were collected.

CFD Methodology

Governing Equations

The general Navier-Stokes equations and conservation of mass are expressed as:

$$\frac{\partial \rho}{\partial t} + \nabla \cdot (\rho V) = 0 \tag{3.2}$$

$$\rho(\frac{\partial V}{\partial t} + V \cdot \nabla V) = -\nabla P + \nabla \cdot T + f \tag{3.3}$$

where V is the fluid velocity vector, ρ is the fluid density, P is the pressure, T is the stress tensor, and f represents body forces acting on the fluid.

The pseudo-random nature of a turbulent flow make a statistical approach to describing the turbulence in the flow a useful strategy. Accordingly, Reynolds decomposition can be used to describe the turbulent field such that

$$u(t) = \bar{u} + u'(t) \tag{3.4}$$

That is, velocity is decomposed into a steady mean value of velocity $\bar{u}$ with a fluctuating component $u'(t)$ superimposed on it. Turbulent flow can then be characterized in term of mean values of fluid properties and some statistical properties of their fluctuation. Using Reynolds decomposition, the effects of fluctuations on the mean flow can be investigated. Similar to the velocity, the flow variables P can be replaced by the sum of a mean and fluctuating component. Then an ensemble average is taken for both the continuity equation and the momentum equations in the Navier-Stokes equation for the mean flow. This yields the Reynolds-averaged Navier-Stokes equations.

$$\frac{\partial \rho}{\partial t} + \nabla V = 0 \tag{3.5}$$

$$\frac{\partial \bar{u}}{\partial t} + \nabla \cdot (\bar{u}V) = -\frac{1}{\rho}\frac{\partial P}{\partial x} + \nu \nabla \cdot \nabla \bar{u} + \frac{1}{\rho}[\frac{\partial(-\rho\overline{u'^2})}{\partial x} + \frac{\partial(-\rho\overline{u'v'})}{\partial y} + \frac{\partial(-\rho\overline{u'w'})}{\partial z}] \tag{3.6}$$

$$\frac{\partial \bar{v}}{\partial t} + \nabla \cdot (\bar{v}V) = -\frac{1}{\rho}\frac{\partial P}{\partial x} + \nu \nabla \cdot \nabla \bar{v} + \frac{1}{\rho}[\frac{\partial(-\rho\overline{u'v'})}{\partial x} + \frac{\partial(-\rho\overline{v'^2})}{\partial y} + \frac{\partial(-\rho\overline{v'w'})}{\partial z}] \tag{3.7}$$

$$\frac{\partial \bar{w}}{\partial t} + \nabla \cdot (\bar{w}V) = -\frac{1}{\rho}\frac{\partial P}{\partial x} + \nu \nabla \cdot \nabla \bar{w} + \frac{1}{\rho}[\frac{\partial(-\rho\overline{u'w'})}{\partial x} + \frac{\partial(-\rho\overline{v'w'})}{\partial y} + \frac{\partial(-\rho\overline{w'^2})}{\partial z}] \tag{3.8}$$

where V is the mean flow velocity vector, ρ is the flow density, and P is the pressure. The term in the square bracket on the right hand side of the equation represents the additional apparent stress as that results from the velocity fluctuations. These additional apparent stresses are called Reynolds stresses. Since no additional equations are available to solve these extra unknown quantities, it is necessary to develop turbulence models to predict the Reynolds stresses and the scalar transport terms and close the system of mean flow equations in order to be able to analyze turbulent flows using the RANS equations.

Turbulence Model

A large number of models exist to model the turbulence and thus have closure in the RANS equations (Kolmogorov, 1942; Saffman, 1970; Wilcox and Alber, 1972; Wilcox, 1988; Spalart, 1992). Among these models, the two-equation models are presently the most widely used and validated be far. There are many two-equation models for engineering and environmental flows have been used in practice. Among them is the kappa-epsilon ($k-\varepsilon$) model, which has been most widely used RANS closure model. The $k-\varepsilon$ model focuses on the mechanisms that affect the turbulent kinetic energy. The turbulent kinetic energy is the energy contained in the velocity fluctuations and can be calculated as k=$\frac{1}{2}(\overline{u'^2}+\overline{v'^2}+\overline{w'^2})$ The standard two-transport-equation $k-\varepsilon$ model solves for turbulent kinetic energy and turbulent dissipation, where turbulent dissipation is the rate at which velocity fluctuations dissipate due to viscous effects in the flow. The transport equations contain coefficients empirically derived and typically are valid for fully turbulent flows only.

In order to develop a mathematical description of the turbulent stress, Boussinesq introduced the concept of an eddy viscosity analogous to the fluid viscosity such that Reynolds stresses would be proportional to mean rates of deformation. Using the suffix notation, the turbulent stresses in the Boussinesq model can be expressed as

$$\tau_{ij} = 2\mu_t S_{ij} - \frac{2}{3}\rho k \delta_{ij} \tag{3.9}$$

where k is the turbulent kinetic energy per unit mass, μ_t is the turbulent (or eddy) viscosity, and S_{ij} is the mean strain-rate tensor. In the standard $k-\varepsilon$ model, the eddy viscosity is determined using a single turbulence length scale, and thus the calculated turbulent diffusion is that which occurs only at this specified scale. Of course, this is a simplification, because in reality all scales of motion will contribute to the turbulent diffusion. The k-ε model then uses the gradient diffusion hypothesis to relate the Reynolds stresses to the mean velocity gradients and the turbulent viscosity. The standard $k-\varepsilon$

model (Launder and Spalding, 1974) has two model equations, one for k and one for ε. Applying dimensional analysis, the eddy viscosity can be found to be:

$$\mu_t = \rho C_\mu \frac{k^2}{\varepsilon} \tag{3.10}$$

where C_μ is a dimensionless constant. The standard k-ε model then uses the following transport equations for k and ε:

$$\rho\frac{\partial k}{\partial t} + \rho\overline{u_j}\frac{\partial k}{\partial x_j} = \tau_{ij}\frac{\partial \overline{u_i}}{\partial x_j} - \rho\varepsilon + \frac{\partial}{\partial x_j}[(\mu + \mu_t/\sigma_k)\frac{\partial k}{\partial x_j}] \tag{3.11}$$

$$\rho\frac{\partial \varepsilon}{\partial t} + \rho\overline{u_j}\frac{\partial \varepsilon}{\partial x_j} = C_{\varepsilon 1}\frac{\varepsilon}{k}\tau_{ij}\frac{\partial \overline{u_i}}{\partial x_j} - C_{\varepsilon 2}\rho\frac{\varepsilon^2}{k} + \frac{\partial}{\partial x_j}[(\mu + \mu_t/\sigma_\varepsilon)\frac{\partial \varepsilon}{\partial x_j}] \tag{3.12}$$

with closure coefficients: $C_{\varepsilon 1} = 1.44$, $C_{\varepsilon 2} = 1.92$, $C_\mu = 0.09$, $\sigma_k = 1.00$, $\sigma_\varepsilon = 1.3$, and auxiliary relations: $\omega = \varepsilon/(C_\mu k)$ and $\mathrm{l} = C_\mu k^{3/2}/\varepsilon$.

Since there are inevitably regions close to solid walls and other interfaces where the local Reynolds number of turbulence is so small that viscous effects predominate over turbulent ones, the wall-function-method of accounting for these regions is widely used in the $k-\varepsilon$ model. The wall-functions provide for a correction to the $k-\varepsilon$ model in these more viscous, less turbulent regions, because recall the $k-\varepsilon$ model is valid only for fully turbulent flows. At high Reynolds number, the standard $k-\varepsilon$ model avoids the need to integrate the model equations right through to the wall by making use of the universal behavior of near-wall flows. Using the assumption that the rate of turbulence production equals the rate of dissipation and incorporating the eddy viscosity formula, the wall-functions are developed as follow, which relate the local wall shear stress to the mean velocity, turbulence kinetic energy, and rate of dissipation.

$$u^+ = \frac{1}{\kappa}\ln(Ey^+) \qquad k = \frac{\mu_\tau^2}{\sqrt[2]{C_\mu}} \qquad \varepsilon = \frac{\mu_\tau^3}{\kappa y} \tag{3.13}$$

where Von Karman's constant, $\kappa = 0.41$ and the wall roughness parameter E = 9.8 for smooth walls.

Method of Solution

The CFD simulation of the Taylor-Couette flow was performed using the OpenFOAM software package. OpenFOAM is an open source CFD software package that consists of customized numerical solvers, and pre- and post-processing utilities for the solution of computational fluid dynamics. OpenFOAM includes a large range of solvers each designed for a specific class of problem. The equations and algorithms differ from one solver to another so that the selection of a solver involves the user making some initial choices on the modeling for particular case. In the OpenFOAM package, the RANS methodology is included in the software as one of the turbulence models for incompressible/compressible flow. Turbulence models to close the RANS equations are also provided in OpenFOAM. In present work, both 2D and 3D meshes were generated by the OpenFOAM package. Figure 3.1 shows the 3D mesh generated by the package.

The precision of RANS simulations and the economy of the computations are strongly dependent on the grid resolution. Thus, a series of pre-simulations were performed to determine the optimal choice of grid needed to accurately capture the flow physics of the Taylor-Couette flow while keeping computational costs as small as possible. A grid-resolution study for both 2D and 3D simulations using the linear (second order central) scheme for interpolation and Gaussian integration for the velocity gradient was performed. The effect of increasing grid resolution was investigated. A series of simulations with progressively finer grid resolutions were performed, with the final two grid resolutions in 2D simulations being: 50×1400 and 75×2100. In the 3D simulations, the final two grids consisted of a total of 946400and 4258800 cells. In order to test the grid convergence, velocity profiles for the 2D and the 3D simulations for different Reynolds numbers were compared.

Grid Resolution Comparison

Figure 3.2 compares profiles for the three velocity components (radial, axial, azimuthal) in Taylor-Couette flow for the two finest grid resolutions in the 2D simulations. The coarser resolution contains a total of 70000 cells, while the number of cells in the finer resolution is 157500. It can be seen from the figure that the results from both grid resolutions are in close agreement in all the three velocity components, demonstrating that both grid resolutions yield similar simulation results. Since the finer grid requires more computational time than the coarse grid while providing the same results, the coarse grid was selected as a better choice for the 2D simulations in this investigation.

The same three velocity profiles for the two finest 3D grid resolutions are compared in Fig. 3.3. The coarse grid in the 3D simulations contains 946400 cells, while the finer grid consists of 4258800 cells. In this figure, all three velocity profiles for both grid resolutions are nearly an exactly match with each other indicating that same simulation results can be achieved from both grid resolutions and thus the results are converged. The coarse grid saves much time and computational sources compared to the finer grid for the 3D simulations, and thus using the coarse grid is a better choice than using the finer one in these simulations.

In the following section, the presented computational results are found using 70000 cells in the 2D simulations and 946400 cells in the 3D simulations.

Results and Discussion

In this section, the results of the 2D and 3D RANS simulations are compared with the stereo PIV experiments to determine how accurately both RANS models predict the mean velocities, the turbulent velocity statistics turbulent dissipation, and the power spectral density of the turbulent flow. For these comparisons, the RANS simulations run for sufficiently long time to allow for the flow to reach a dynamic steady state.

Velocity Statistics Comparison

Comparisons between the RANS simulations and stereo PIV data have been made for the turbulent Taylor-Couette flow at different Reynolds numbers. The comparisons are most easily made using profile plots of the mean velocity and turbulent statistics. Note that for the 2D simulations, the simulation plane was used for comparison with the PIV data, while for the 3D simulations a single plane was sampled from the simulation volume to compare with the PIV data. When creating the profiles, two different profile locations were chosen. One was chosen along the centerline of the gap, while the other was chosen near the inner cylinder one-eighth of the gap width from the inner cylinder. The profile locations are shown in Fig. 3.4.

A comparison of 2D RANS simulation with PIV data along the gap centerline containing the mean velocity profiles for axial, radial, and azimuthal velocity as well as Turbulent Kinetic Energy (TKE) at $R = 60$ is shown in Fig. 3.5. As in all of the comparison plots, the RANS data in Fig. 3.5 are represented by symbols, and the PIV data are presented using lines. As can be seen in the Fig. 3.5, the axial and radial velocity profiles of simulation match with the PIV data well except for a small difference in the radial velocity at the outflow boundary. In the azimuthal velocity profile comparison, the basic shape and magnitude for both the simulation and PIV data agree with each other. Some small variations in the shape do appear in the comparison of simulation with PIV result. This is because the azimuthal velocity, being the out-of-plane velocity component is relatively more difficult to capture in the experiment. However, the azimuthal velocity also compares well, and thus overall, the mean velocities show remarkable agreement. In the TKE comparison, the simulation agrees very well with the PIV data. These results demonstrate that at this Reynolds number the 2D RANS method using the $k - \varepsilon$ model is very accurate in simulating the Taylor-Couette flow.

As the rotation velocity increases, the azimuthal velocity will increase as a result. In Fig. 3.6, the Reynolds number is increased to $R = 80$. The peak absolute value of

azimuthal velocity in the profiles increases with Reynolds number which corresponds to the increasing angular velocity of rotating inner cylinder. However, the magnitudes of the axial and the radial velocity barely change, suggesting that increasing the rotating velocity of inner cylinder affects mainly the azimuthal velocity and not the axial and radial velocities. The RANS results for all three mean velocity profiles compare well with the PIV data with only the same small difference in radial velocity observed at the outflow boundary. It can also be seen in Fig. 3.6, that the mean magnitude of the TKE increases with the angular velocity of the inner cylinder which represents the flow becoming more turbulent at higher Reynolds number. In the figure, the TKE of the simulation and of the PIV results also agree well with each other, demonstrating the simulation is accurate at this Reynolds number.

In Fig. 3.7, the three mean velocity profiles are compared for R=130 between PIV and simulation. The simulation results once again agree with the PIV data well. The magnitudes of azimuthal velocity and TKE continue changing with the increasing of Reynolds numbers while the other two mean velocities barely change.

For Reynolds number $R = 160$, Fig. 3.8 shows that the absolute magnitude of the peak azimuthal velocity profile increases still higher (as expected) with the increase in Reynolds number, while the velocity profiles in other two directions remain unchanged, and TKE magnitude also continues to rise. As for the lower Reynolds numbers, the RANS simulation predicted the same shape, magnitude, and trends in the profile plots as the PIV data.

As the Reynolds number is increased to $R = 190$, the same trends of increasing magnitude of azimuthal velocity and TKE appear, as shown in Fig. 3.9. The simulation results also have good agreement with the PIV data. In fact, compared with the previous cases, the velocity profiles of the simulation actually agree better with PIV for this highest Reynolds number. This is not unexpected, as the $k - \varepsilon$ model assumes high Reynolds number, fully developed turbulence, and R=190 is the case that most closely approaches

this assumption. Also at $R = 190$, the highly turbulent flow leads to multiple peaks in the experimental TKE plot, while the RANS simulation generates only a single peak corresponding to the unsteady (not turbulent) motion in the flow.

Figures 3.10 through 3.14 are the mean velocity profiles for the axial, radial, and azimuthal velocities and the TKE comparison between PIV and simulation results near the inner cylinder wall (1/8 of the gap distance from the wall). As can be seen in the figures, all the mean velocity and TKE results of the simulation match with the PIV data well. The azimuthal mean velocity and TKE magnitudes also follow the same trends as the comparisons made at the center of the gap.

In addition to the 2D simulations, the three mean velocity profiles and the TKE of the 3D simulations are also compared with PIV data for R=60 in Fig. 3.15. It can been in the figure that all the simulation velocity profiles and TKE compare well with PIV data except for a variation in the radial velocity magnitude. Based on the velocity statistics comparison for cases at different Reynolds numbers, the 2D and 3D simulations with RANS method are accurate in the study of flow. However, since the 2D simulations yield nearly the same results as the 3D simulations and they consume much less time computing the simulation results, the 2D simulation were deemed a better choice in the simulation of Taylor-Couette flow, and thus were used for most of the investigations presented in this thesis.

In addition to the mean velocity profiles and TKE, turbulence dissipation rates have also been compared between PIV and simulation results at the center of the gap at different Reynolds numbers in Figs. 3.16-3.20, and near the wall (1/8 of the gap distance from the wall) in Figs. 3.21-3.25). The peak in the dissipation rate for both PIV and CFD increases as the Reynolds number increases which, of course, is expected since the $k - \varepsilon$ model balances TKE and dissipation. There is a mismatch in the locations of the peaks in TKE and dissipation. The TKE peaks very close to the vortex centers, while the dissipation peaks close to the vortex boundaries (but not at the boundaries), where

velocity gradients are the highest. The shape and magnitude of simulation results are very close to those of the PIV data, demonstrating that the simulations accurately predict the turbulence dissipation rate. The same trend and agreement between simulation and experiment are observed in the dissipation rate comparisons near the cylinder wall.

Reynolds stress Results

Because the PIV results include all three components of instantaneous velocity, it is possible to directly compute Reynolds stresses from these data (the simulation results yields only TKE, not the individual Reynolds stresses). Figs. 3.26-3.28 are the normal stresses along the gap centerline at different Reynolds numbers, and Figs. 3.29-3.31 are the shear stresses along the gap centerline. In these plots, axial position equal to zero is located at outflow boundary. The normal stresses and shear stresses are normalized using the rotating velocity of the inner cylinder. The magnitude of the normalized normal stresses $u'u'$ and $w'w'$ decreases as the Reynolds number increases, while the other normal stress, $v'v'$, increases with increasing Reynolds number. All three normal stresses become more homogeneous with increasing R, suggesting that the Taylor vortex structure in the flow become less pronounced with increasing R. The normalized shear stresses of $u'v'$ and $u'w'$ follow the same trend, with the magnitude decreasing with increasing Reynolds number. However, the shear stress $v'w'$ increases with the inner cylinder accelerating. These shear stresses also become more homogeneous with increasing Reynolds numbers.

Reynolds stresses contribute to the momentum flux transferred in the different directions in the turbulent flow. For example, $u'u'$ represents the u momentum flux transferred in the u direction and $u'v'$ represents the u momentum flux transferred in the v direction. In turbulent Taylor-Couette flow, streamwise momentum flux is mainly transited by the flow structure of the Taylor vortex. As Reynolds number increases, the flow becomes highly turbulent and breaks the structures of toroidal vortices into small turbulent vortex structures which causes the advection of streamwise momentum flux becoming less pro-

nounced in the turbulent Taylor-Couette flow. This explains the phenomenon that both the normal and shear stress in the Taylor-Couette flow appear to be more homogenous with increasing Reynolds number.

The other profile plane, one eight of the gap distance from the inner cylinder wall is the same as the previous velocity profiles investigation, is used in the study of Reynolds stress. Figures 3.32-3.34 are the normalized normal stress at this location, and Figures 3.35-3.37 are the normalized shear stresses at this location. All these results present the same trends as the gap center profiles discussed above.

Power Spectral Density Results

The Power Spectral Density (PSD) describes how the power of a signal or time series is distributed over frequencies. It is useful in analyzing the Taylor-Couette flow, especially for low Reynolds number because it makes it easy to identify and describe unsteady periodic motion in the flow. When the flow becomes turbulent, the power spectrum of the experimental data includes broadband turbulence, making it difficult to identify the contribution due to unsteady motion. The results of the unsteady simulation do not contain turbulence contribution in the PSD, and only contain unsteady flow contributions of the turbulent Taylor-Couette flow.

First, a comparison between the simulation and PIV power spectral densities at Reynolds number $R = 17$ is made in Fig. 3.38. In the previous chapter, where the power spectrum was found from the experimental data, the Reynolds number $R = 17$ was found to be the special case where the traveling azimuthal waves all but disappear in the flow resulting in very weak peaks in the PSD results. The "relative magnitude" in Fig. 3.38 is the ratio between magnitude of the PSD at $R = 17$ to the dominant peak magnitude at $R = 6$, (this is the same normalization used in chapter 2). The result of 2D RANS simulation using $k - \varepsilon$ model agrees well with the PIV power spectrum. The flow at R=17 is mostly laminar, but RANS simulations were performed at this R to determine

if the RANS simulations were sensitive enough to capture the instabilities that lead to the azimuthal wave motion. Both plots have no sharp peaks and two small rises at the same normalized frequency regime which represents the previously found result that the traveling azimuthal waves in the flow at this rotation velocity are extremely weak.

At higher rotational velocities, Taylor-Couette flow becomes turbulent. Figure 3.39 shows the comparison between the PSD of the PIV and simulation results at a Reynolds number of 50. It can be seen in the figure that there are multiple peaks in the PIV plot which results difficulties in defining the wavy motions in turbulent flow. This also is a consequence of the limited amount of PIV data used in this plot. The experimental PSD plot is generated by averaging by together the PSD for individual PIV experiment runs at each Reynolds number, but experimental constraints limit the number of runs available for analysis. In the simulation plot, there is only one dominant peak in the power spectrum which represents an unsteady wavy motion in the turbulent Taylor Couette flow. The normalized frequency of this peak corresponds to the first peak in the PIV results and can be used to help interpret the PIV data. There is also a broadband component due to small scale turbulence in the PIV power spectral density result which does not appear in the simulation results since the turbulence in the simulation is not resolved.

Figure 3.40 presents the comparison between simulation and PIV results at Reynolds number R =55. The peak power spectrum magnitude of the dominant peak both the PIV and simulation results was lower than at R=50 indicating that the unsteady wavy motion is weaker in this case. The one dominant peak which the $k-\varepsilon$ model predicts captures the wave length of the unsteady wave motion and can be observed in the simulation result, while multiple peaks appear in the PIV data. The peak in the simulation corresponds to the first sharp peak in the PIV result. When Reynolds number is further increased to increases to $R = 60$, as shown in Fig. 3.41, the unsteady wave motion captured by the simulation peak once again corresponds to the first peak in the PIV data. If the Reynolds

number is increased still further to $R = 65$ and 70, the power magnitude of the peak in the PSD decreases still further as Reynolds number rises as seen in Figs. 3.42 and 3.43. Here as well, the Power spectral of the simulation still has a single dominant peak representing the unsteady motion, while the broadband turbulent spectrum in the PIV results are not observed in the simulation results. The dominant peak power magnitude increases again following the rise of Reynolds number from 75 to 80 as seen in Figs. 3.44 and 3.45. Just as before, the simulation captured the wave length of the unsteady wavy but not the modeled turbulence. Notice that at each of the Reynolds number, the normalized frequency of the dominant peak in the simulations is 0.07, which was the normalized frequency of the waves that appeared at lower Reynolds numbers in the wavy Taylor vortex regime.

After Reynolds number exceeds 80, the peak in the power magnitude of power spectrum decreases until it reaching a minimum and stays at that level, as can be seen in the Figs. 3.46 to 3.52. For these high Reynolds number cases, the simulation results still capture unsteady wavy motion as can be seen in the power spectral density. All the peaks of the unsteady wave in the simulation match the first sharp peak in the PIV data, and all the turbulent spectrum observed in the PIV results is unresolved in the simulation. Based on all the different Reynolds number cases, 2D RANS simulation using $k-\varepsilon$ model compares well with the unsteady peaks in the PIV data PSD analysis, indicating the RANS method accurately models the unsteady motion in the Taylor-Couette flow.

PSD results for 3D RANS simulations using $k-\varepsilon$ model are compared with PIV data at $R = 60$ and R= 80 in Figs. 3.53 and 3.54. Just as in the 2D simulations, the 3D results also have one dominant peak which captures the wave length of the slow unsteady waves in the turbulent Taylor Couette flow, while the turbulent spectrum is modeled in the simulation and not resolved. The 3D simulation PSD results are compared with 2D simulation PSD results at Reynolds number 60 and 80, as shown in the Figs. 3.55 and 3.56. It can be seen in these comparisons that at the different Reynolds numbers,

the 2D and 3D power spectral density results are almost identical to each other except a very small difference in the magnitude of the dominant peak. Since 3D simulations require much more time and computational sources, the 2D simulation is a better option to analyze the Taylor Couette flow since it inexpensive and faster to solve.

Summary and Conclusion

Reynolds-averaged Navier-Stokes equation simulations using $k - \varepsilon$ model were performed for turbulent Taylor-Couette flow, where the outer cylinder is fixed and the inner cylinder rotates. Particle image velocimetry experiments were performed in an experimental apparatus of the same geometry as the simulations in order to both provide detailed velocity statistics that were used to validate the accuracy of the RANS models used in this investigation. The effects of grid resolution on the velocity statistics using second order central schemes for interpolation and second order Gaussian integration, and explicit non-orthogonal correction as the gradient scheme were studied in order to determine the effect of these parameters on the accuracy of the simulation results. Different grid resolutions were tested for both the 2D and 3D simulations, and the differences observed at the higher resolutions compared to the resolution chosen for the presented simulation were small, demonstrating that grid independence was achieved. The 2D and 3D RANS simulations with the two equations model $k - \varepsilon$ model, and wall-function, using the standard values for the constants at different Reynolds numbers was found to compare very well with velocity statistics for the PIV data, including mean axial, radial, and azimuthal velocities, turbulent kinetic energy, and dissipation rate.

A comparison of the power spectral density over a range of Reynolds numbers showed the RANS simulations appeared to accurately model the unsteady motion. The power spectral density of the RANS simulations displayed the same trends as the PIV data with the changing rotational velocity. The 3D simulation results for power spectral density

were also compared with the 2D results to test the agreement between the different simulation methods. In the comparison, very little difference in the 3D simulation could be found, indicating the 2D simulations were sufficient for capturing the unsteadiness. The excellent agreement observed between both the velocity statistics and the power spectral density of the simulations and the PIV data demonstrate that RANS using the $k - \varepsilon$ model is able to accurately capture the important characteristics in turbulent Taylor-Couette flow. Finally, the excellent agreement between the results of 2D and 3D simulations indicates that 2D RANS with the $k - \varepsilon$ model is a precise and economical method for simulating turbulent Taylor-Couette flow, since the 3D simulations require much more time and computational resources while providing the same outcomes.

Figure 3.1 3D Mesh generated for RANS simulation

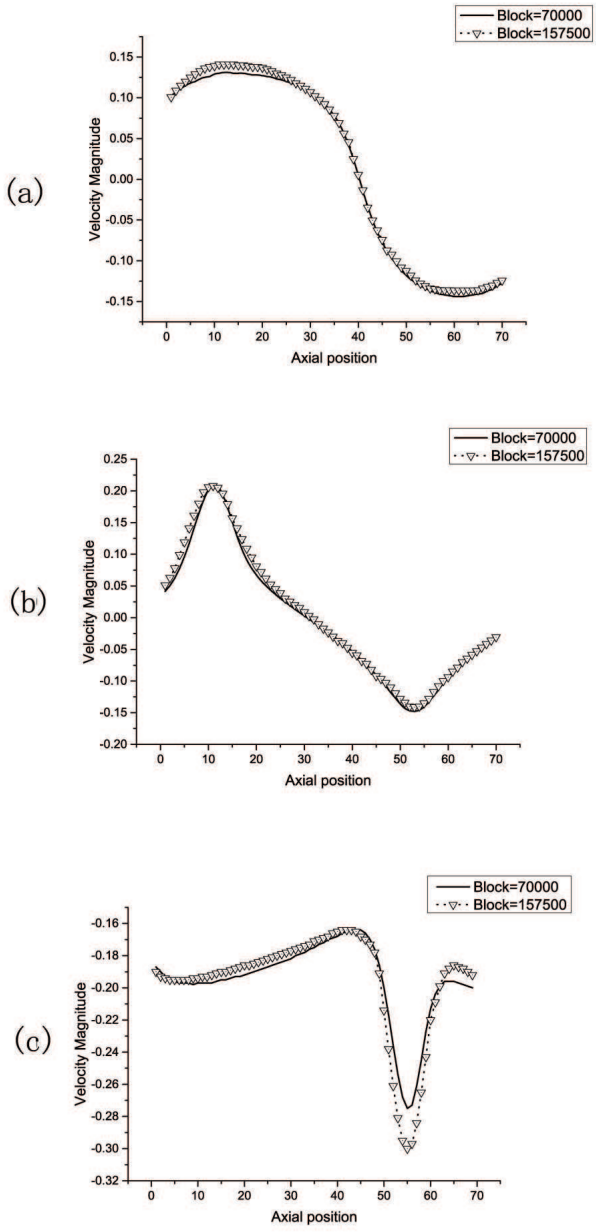

Figure 3.2 Grid resolution comparison of 2D: (a) Axial Velocity (mm/s), (b) Radial Velocity (mm/s), (c) Azimuthal Velocity (mm/s)

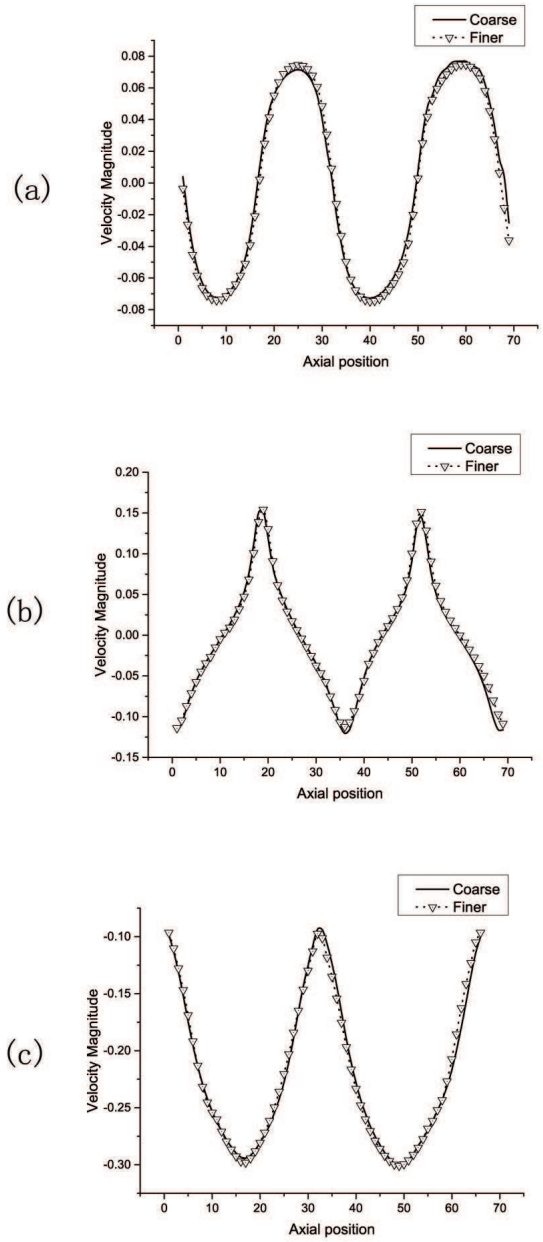

Figure 3.3 Grid resolution comparison of 3D: (a) Axial Velocity (mm/s), (b) Radial Velocity (mm/s), (c) Azimuthal Velocity (mm/s)

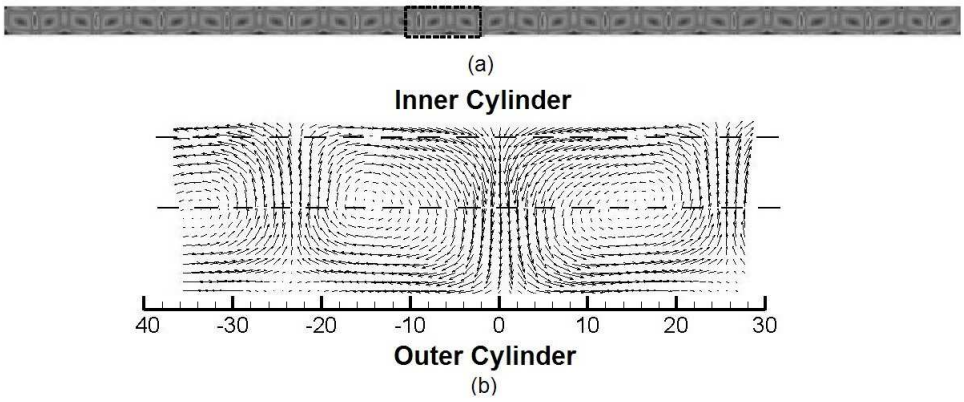

Figure 3.4 Example of simulation mean velocity field. (a) Full mean velocity profile of 2D simulation, (b) Mean velocity profile measurement domain. The axial coordinate is defined such that 0 location corresponds to the outflow boundary.

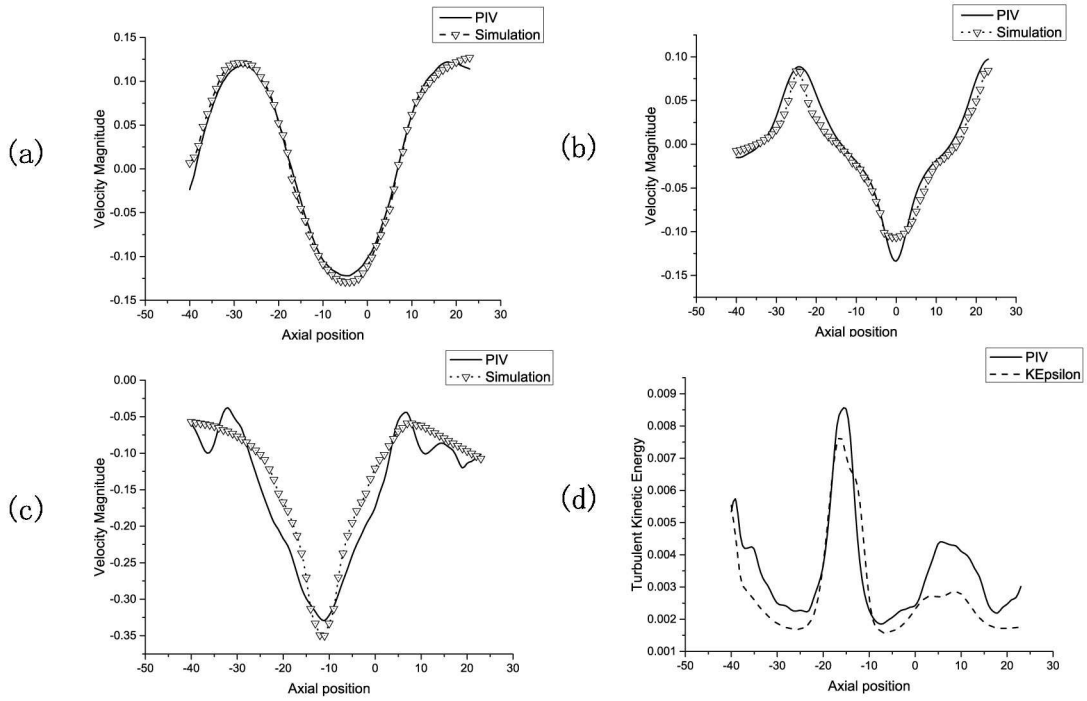

Figure 3.5 2D Velocity Profile and TKE Comparison at $R = 60$: (a) Axial Velocity (mm/s), (b) Radial Velocity (mm/s), (c) Azimuthal Velocity (mm/s), (d) Normalized TKE

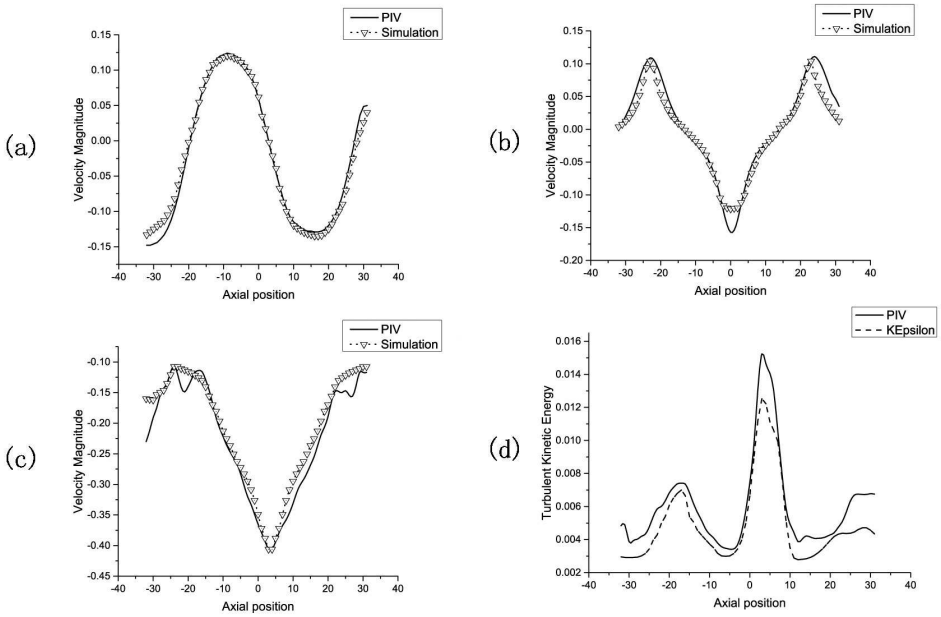

Figure 3.6 2D Velocity Profile and TKE Comparison at $R = 80$: (a) Axial Velocity (mm/s), (b) Radial Velocity (mm/s), (c) Azimuthal Velocity (mm/s), (d) Normalized TKE

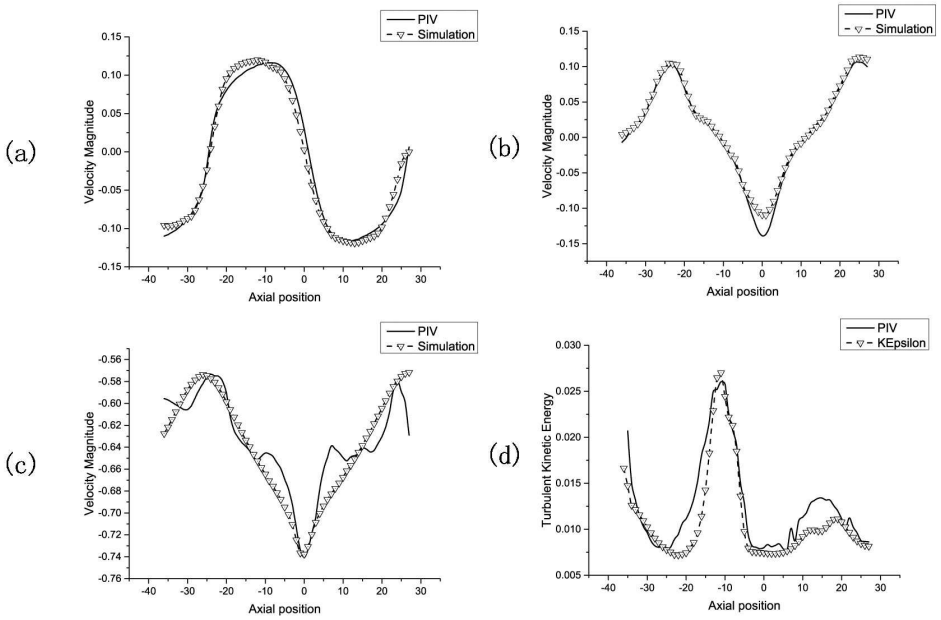

Figure 3.7 2D Velocity Profile and TKE Comparison at $R = 130$: (a) Axial Velocity (mm/s), (b) Radial Velocity (mm/s), (c) Azimuthal Velocity (mm/s), (d) Normalized TKE

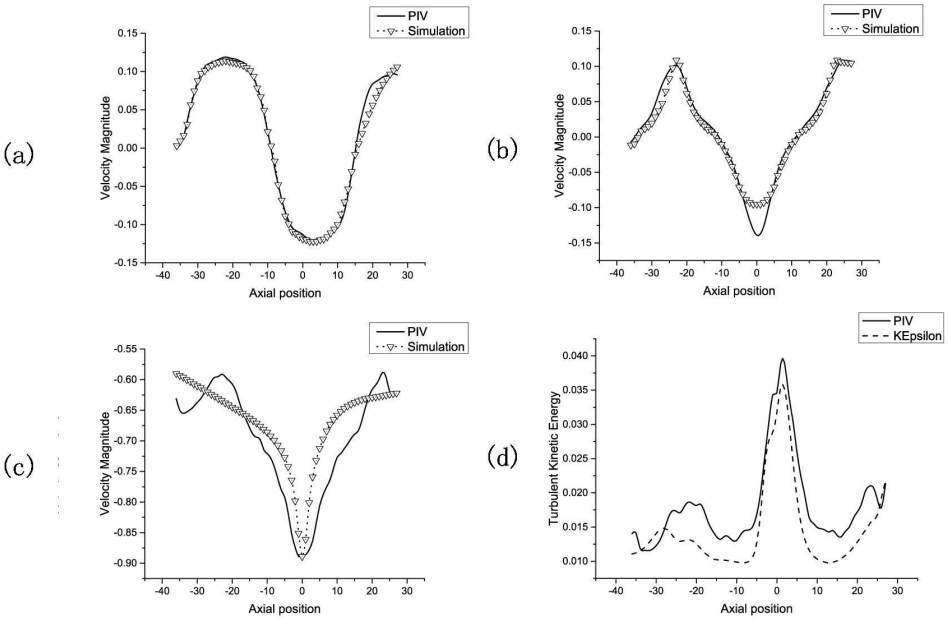

Figure 3.8 2D Velocity Profile and TKE Comparison at $R = 160$: (a) Axial Velocity (mm/s), (b) Radial Velocity (mm/s), (c) Azimuthal Velocity (mm/s), (d) Normalized TKE

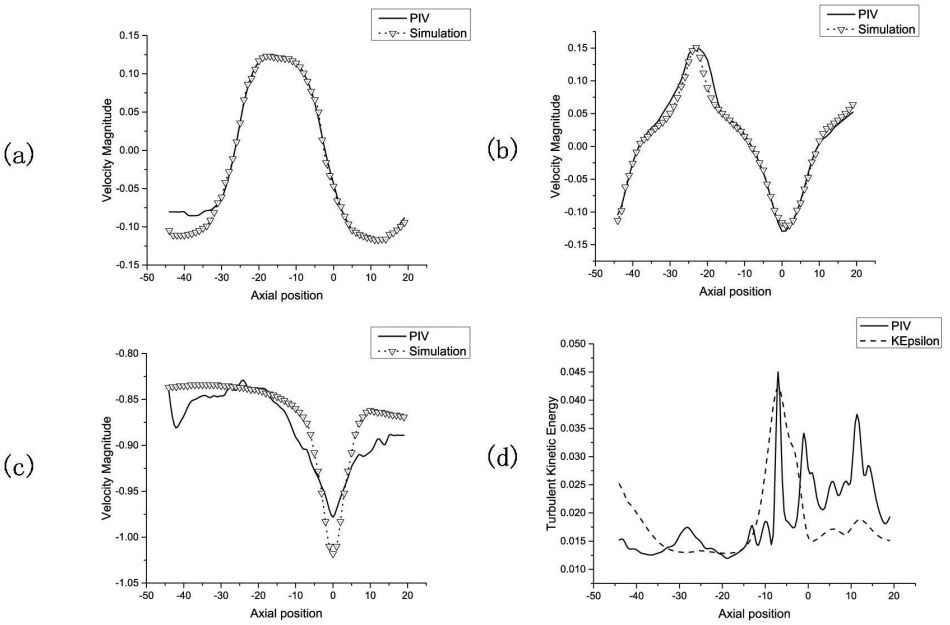

Figure 3.9 2D Velocity Profile and TKE Comparison at $R = 190$: (a) Axial Velocity (mm/s), (b) Radial Velocity (mm/s), (c) Azimuthal Velocity (mm/s), (d) Normalized TKE

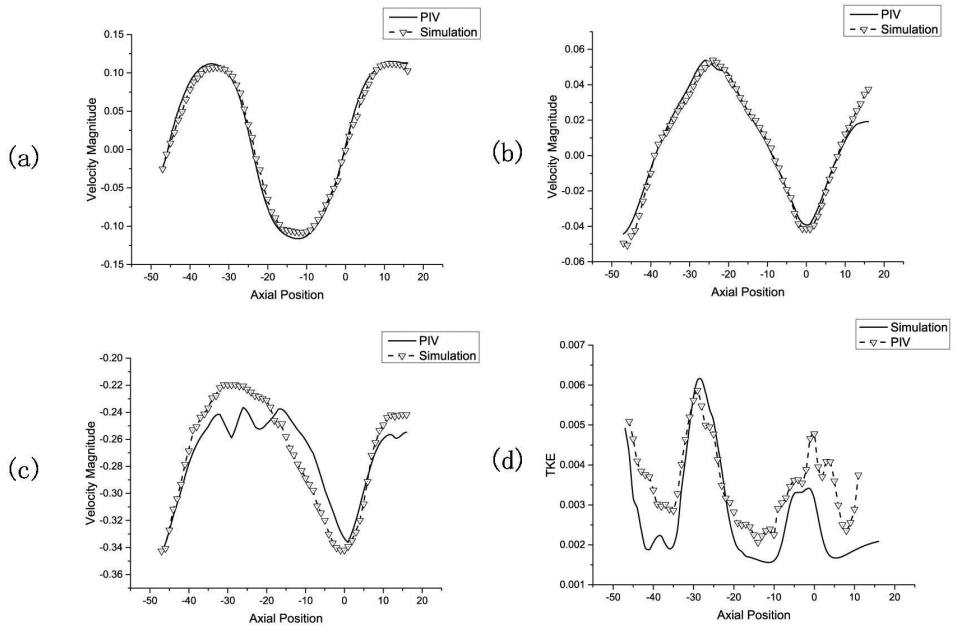

Figure 3.10 2D Velocity Profile and TKE Comparison near wall (1/8 gap distance from cylinder wall) at $R = 60$: (a) Axial Velocity (mm/s), (b) Radial Velocity (mm/s), (c) Azimuthal Velocity (mm/s), (d) Normalized TKE

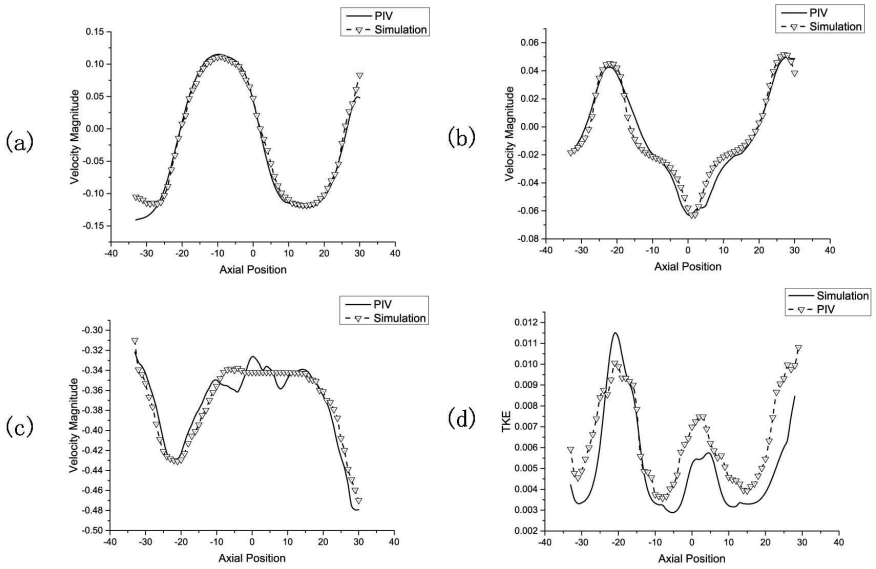

Figure 3.11 2D Velocity Profile and TKE Comparison near wall (1/8 gap distance from cylinder wall) at $R = 80$: (a) Axial Velocity (mm/s), (b) Radial Velocity (mm/s), (c) Azimuthal Velocity (mm/s), (d) Normalized TKE

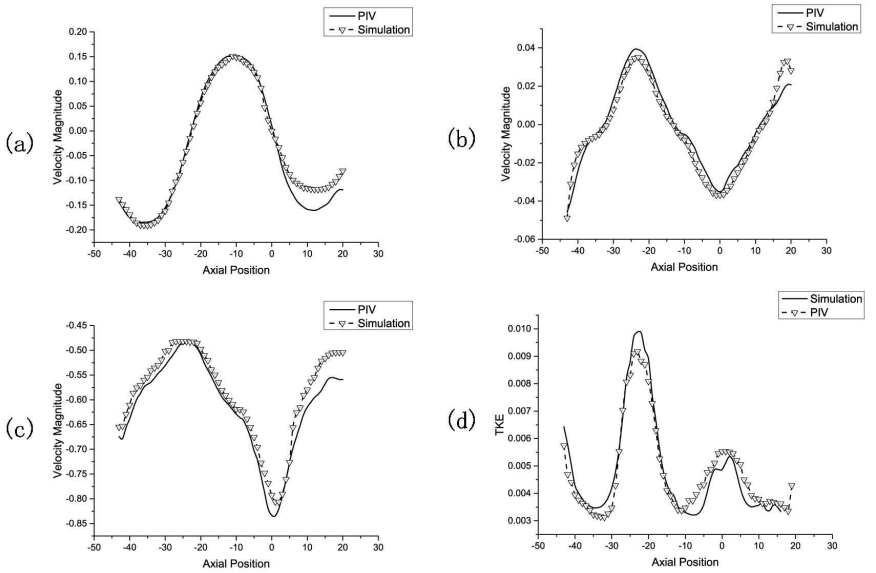

Figure 3.12 2D Velocity Profile and TKE Comparison near wall (1/8 gap distance from cylinder wall) at $R = 130$: (a) Axial Velocity (mm/s), (b) Radial Velocity (mm/s), (c) Azimuthal Velocity (mm/s), (d) Normalized TKE

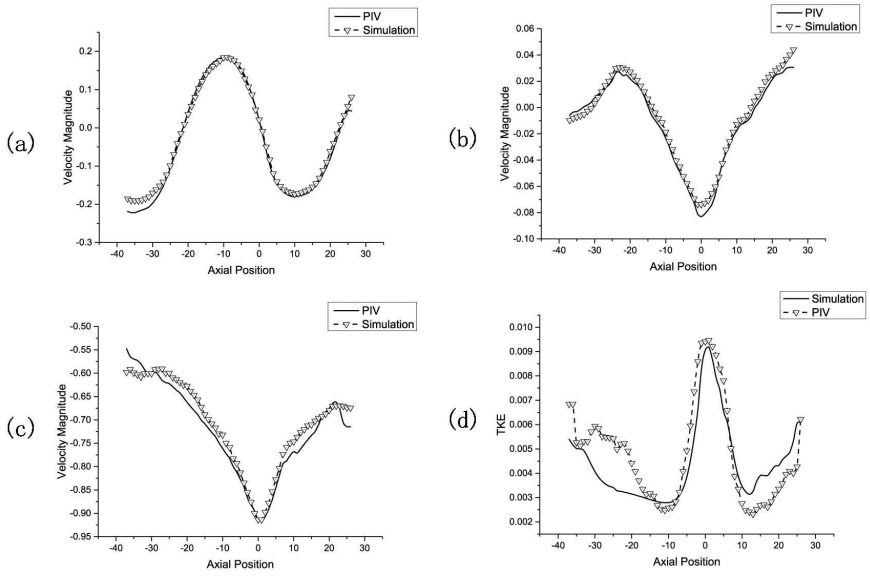

Figure 3.13 2D Velocity Profile and TKE Comparison near wall (1/8 gap distance from cylinder wall) at $R = 160$: (a) Axial Velocity (mm/s), (b) Radial Velocity (mm/s), (c) Azimuthal Velocity (mm/s), (d) Normalized TKE

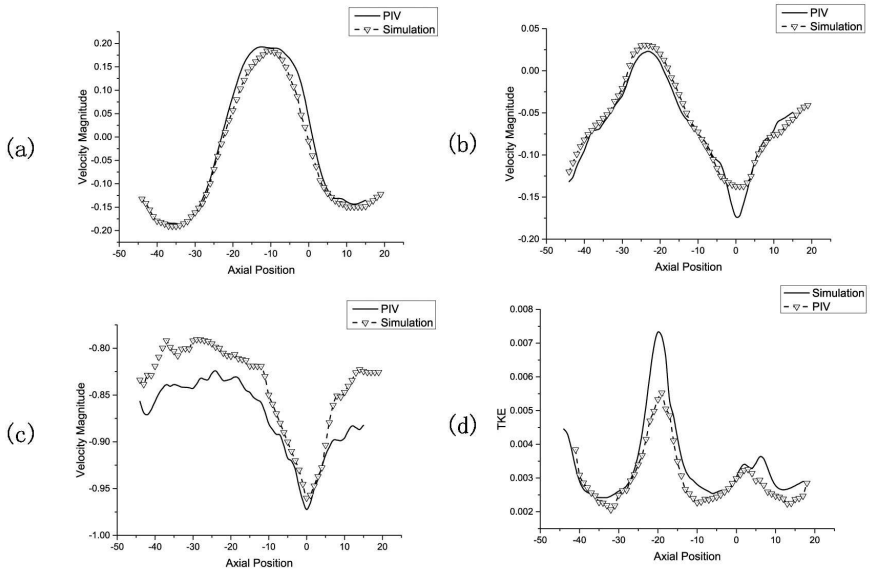

Figure 3.14 2D Velocity Profile and TKE Comparison near wall (1/8 gap distance from cylinder wall) at $R = 190$: (a) Axial Velocity (mm/s), (b) Radial Velocity (mm/s), (c) Azimuthal Velocity (mm/s), (d) Normalized TKE

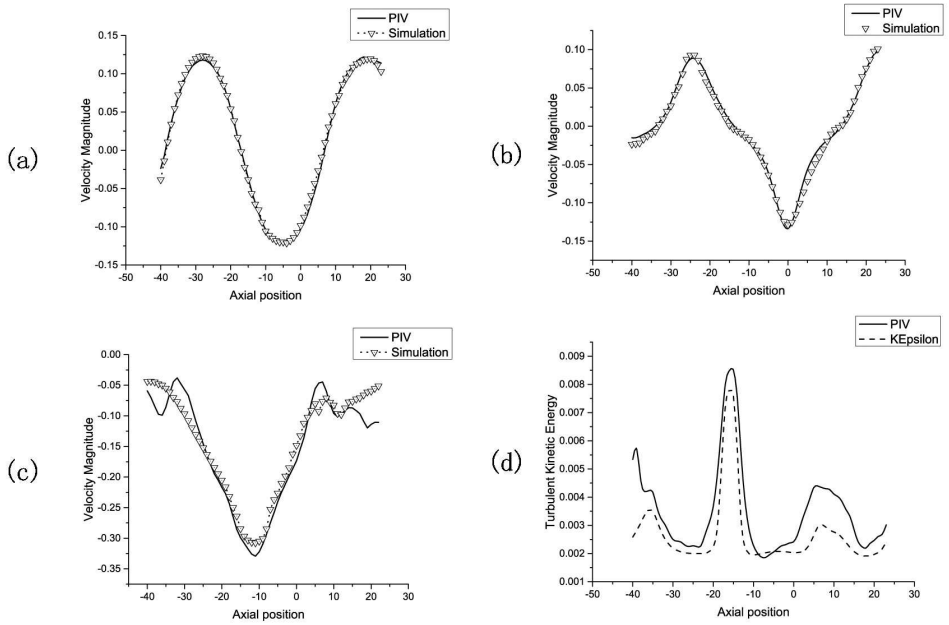

Figure 3.15 3D Velocity Profile and TKE Comparison at $R = 60$: (a) Axial Velocity (mm/s), (b) Radial Velocity (mm/s), (c) Azimuthal Velocity (mm/s), (d) Normalized TKE

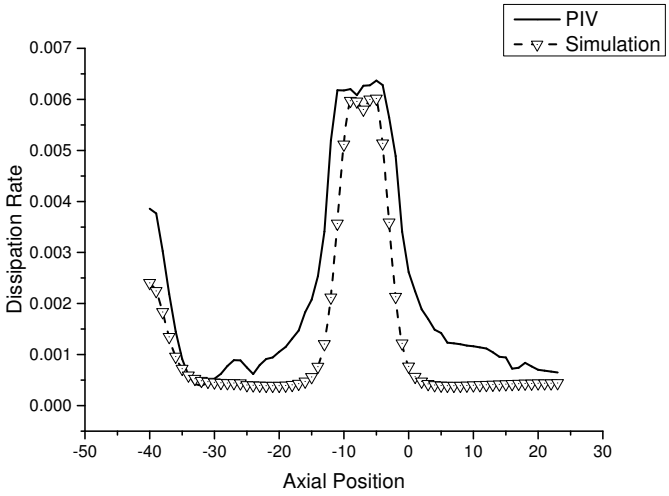

Figure 3.16 Normalized Turbulence Dissipation Rate Comparison between PIV and Simulation at R=60

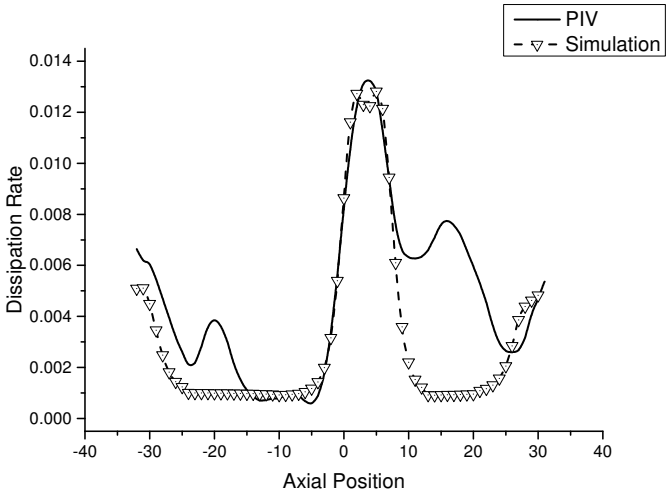

Figure 3.17 Normalized Turbulence Dissipation Rate Comparison between PIV and Simulation at R=80

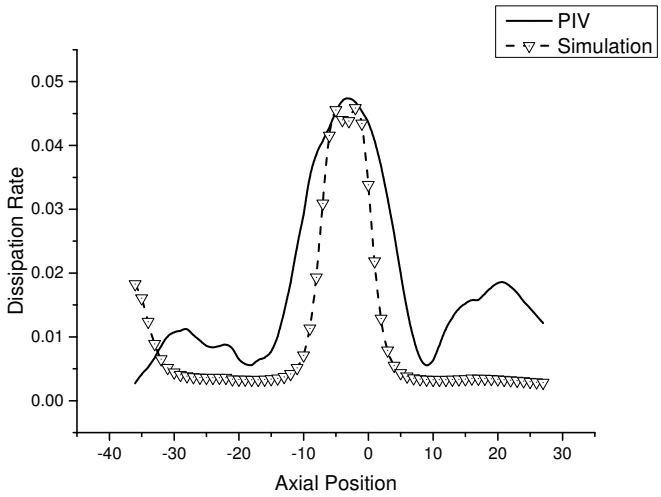

Figure 3.18 Normalized Turbulence Dissipation Rate Comparison between PIV and Simulation at R=130

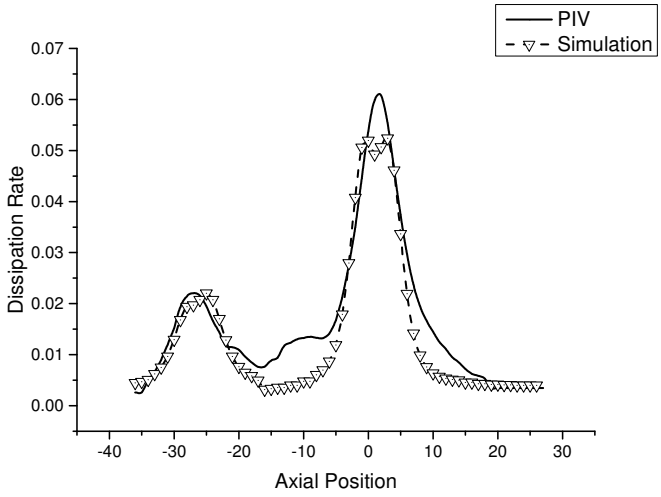

Figure 3.19 Normalized Turbulence Dissipation Rate Comparison between PIV and Simulation at R=160

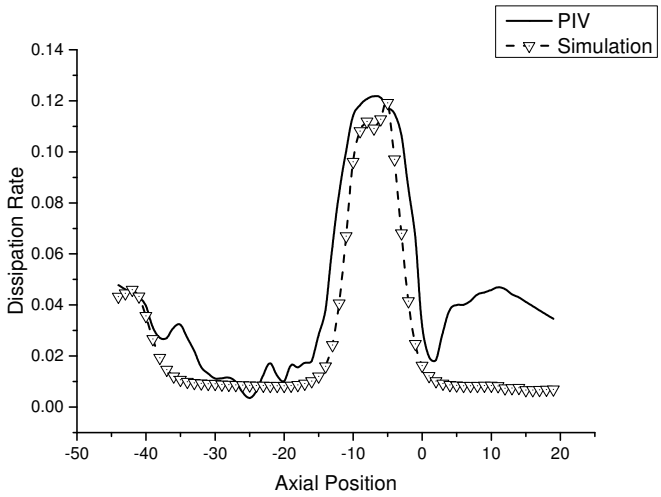

Figure 3.20 Normalized Turbulence Dissipation Rate Comparison between PIV and Simulation at R=190

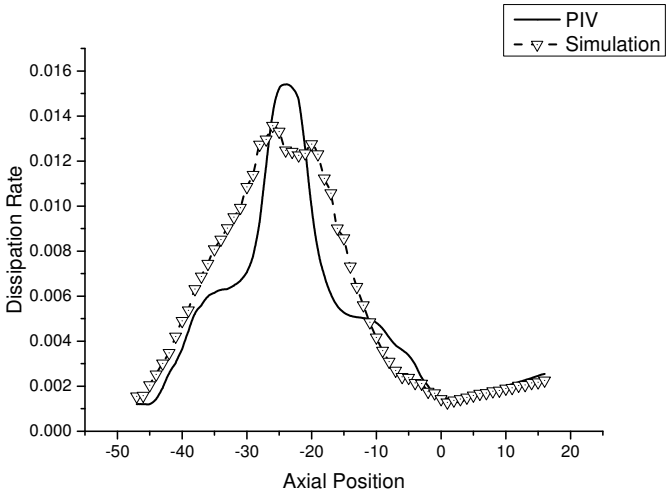

Figure 3.21 Normalized Turbulence Dissipation Rate Comparison near wall (1/8 gap distance from cylinder wall) between PIV and Simulation at R=60

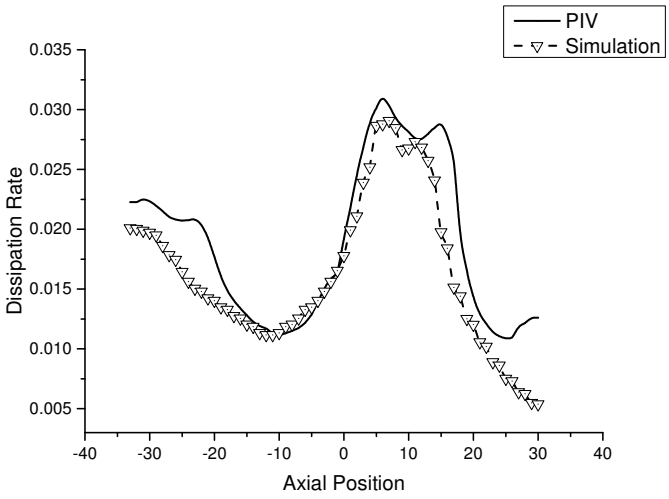

Figure 3.22 Normalized Turbulence Dissipation Rate Comparison near wall (1/8 gap distance from cylinder wall) between PIV and Simulation at R=80

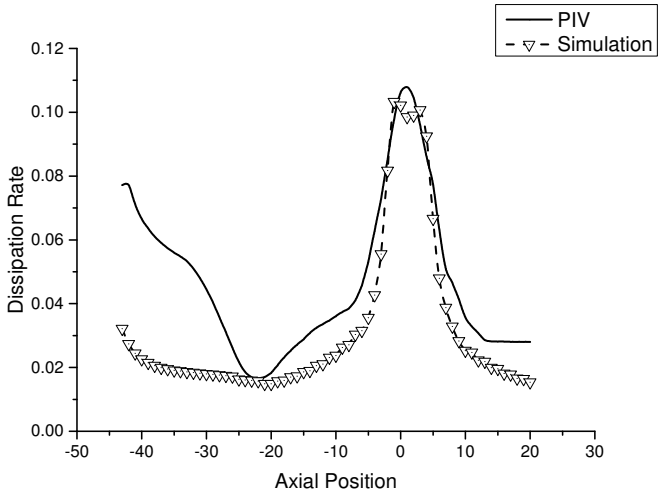

Figure 3.23 Normalized Turbulence Dissipation Rate Comparison near wall (1/8 gap distance from cylinder wall) between PIV and Simulation at R=130

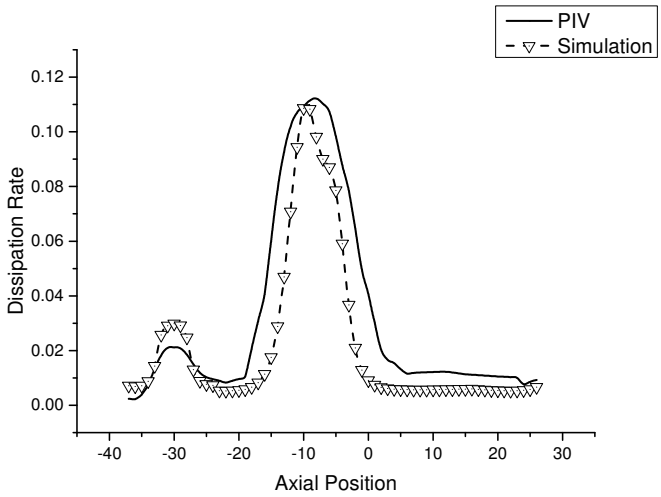

Figure 3.24 Normalized Turbulence Dissipation Rate Comparison near wall (1/8 gap distance from cylinder wall) between PIV and Simulation at R=160

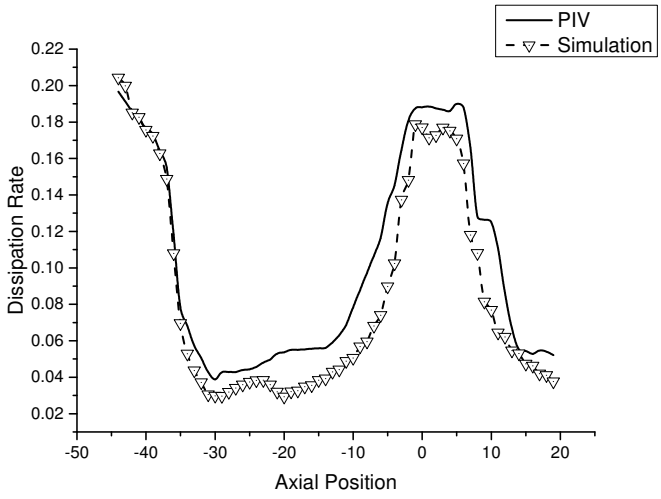

Figure 3.25 Normalized Turbulence Dissipation Rate Comparison near wall (1/8 gap distance from cylinder wall) between PIV and Simulation at R=190

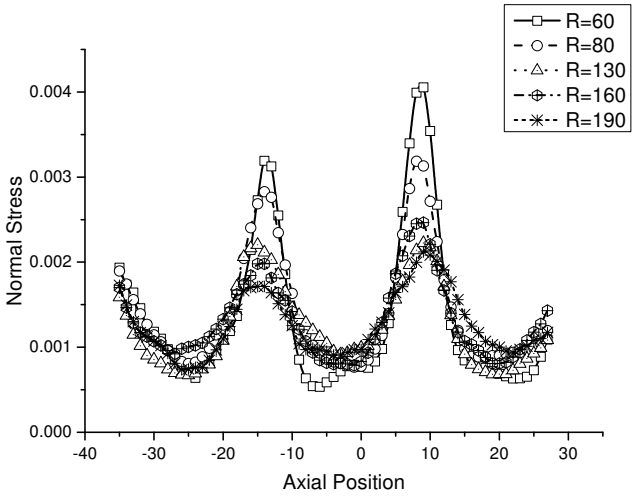

Figure 3.26 Normalized Normal stress (u'u') of PIV data at different Reynolds numbers

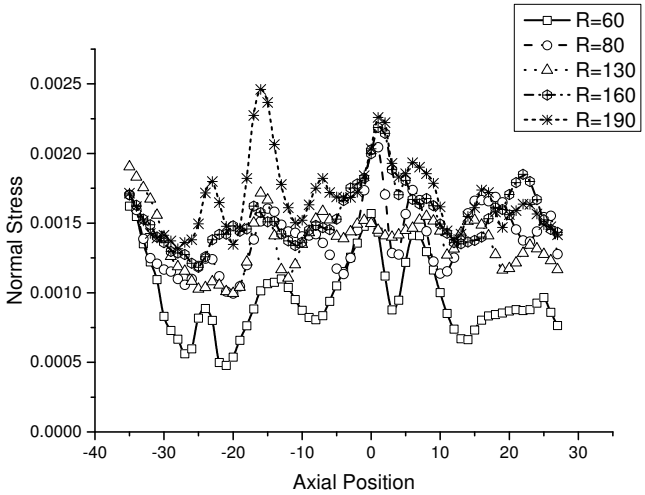

Figure 3.27 Normalized Normal stress (v'v') of PIV data at different Reynolds numbers

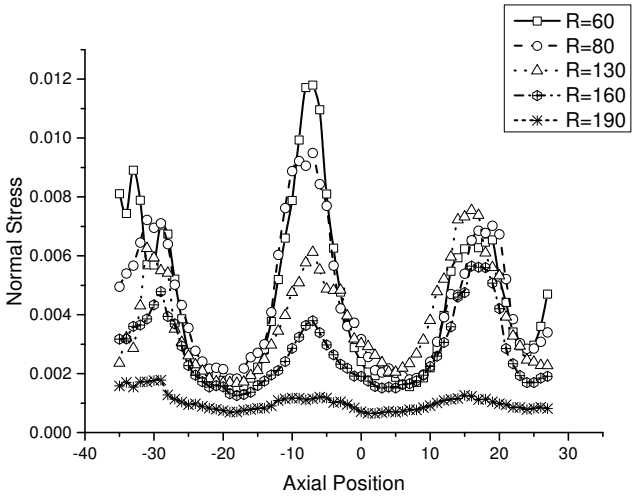

Figure 3.28 Normalized Normal stress (w'w') of PIV data at different Reynolds numbers

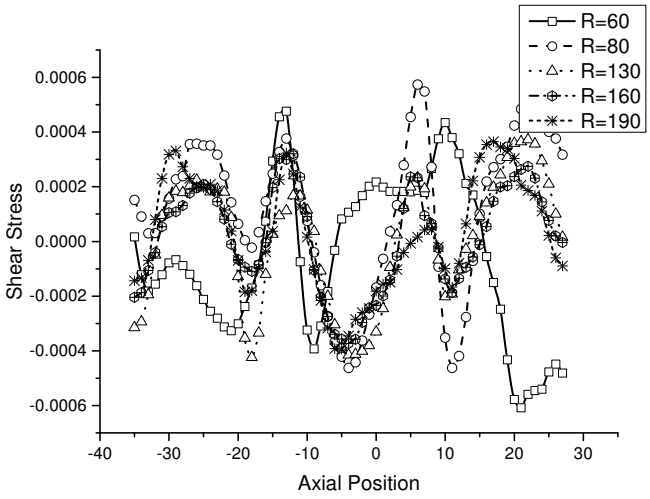

Figure 3.29 Normalized Shear stress (u'v') of PIV data at different Reynolds numbers

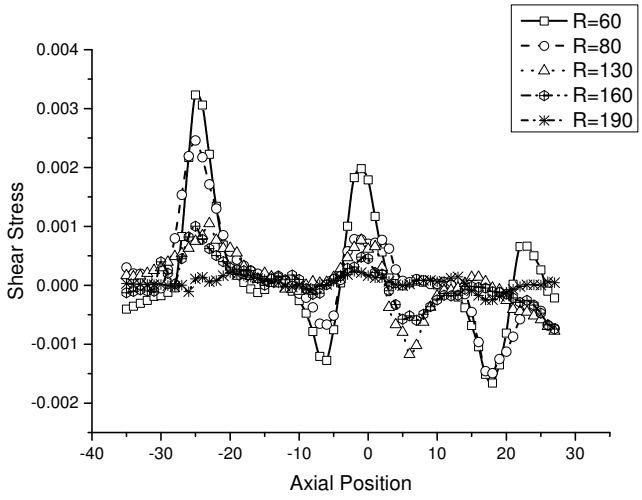

Figure 3.30 Normalized Shear stress (u'w') of PIV data at different Reynolds numbers

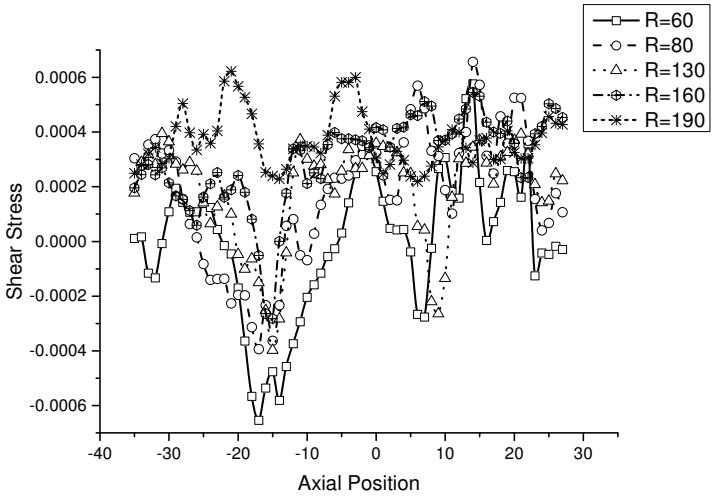

Figure 3.31 Normalized Shear stress (v'w') of PIV data at different Reynolds numbers

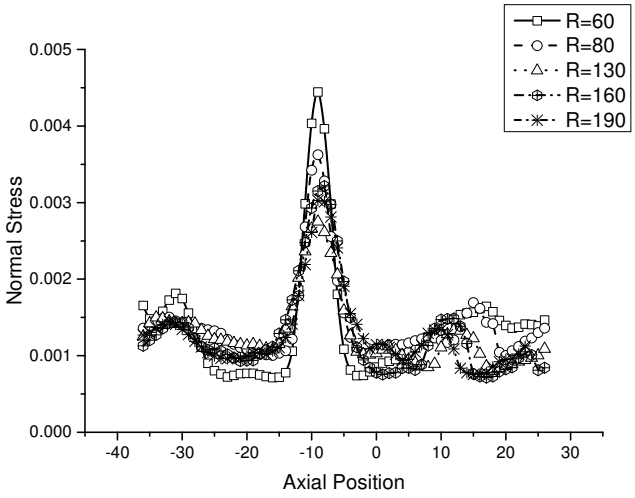

Figure 3.32 Normalized Normal stress (u'u') near wall (1/8 gap distance from cylinder wall) of PIV data at different Reynolds numbers

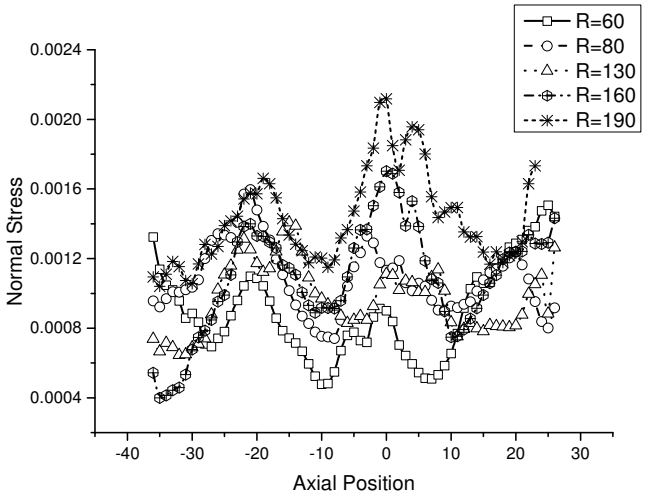

Figure 3.33 Normalized Normal stress (v'v') near wall (1/8 gap distance from cylinder wall) of PIV data at different Reynolds numbers

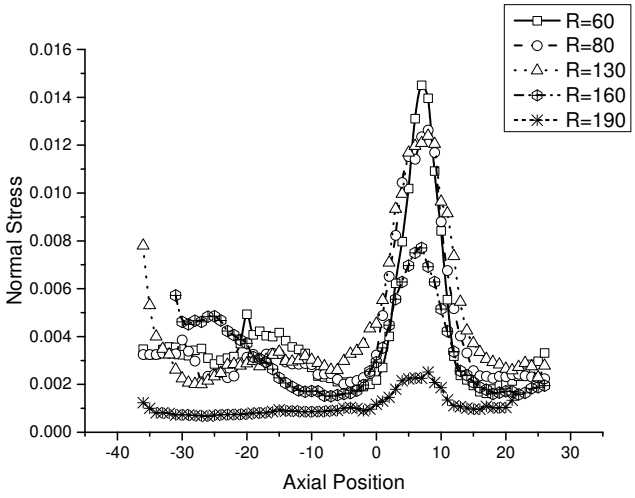

Figure 3.34 Normalized Normal stress (w'w') near wall (1/8 gap distance from cylinder wall) of PIV data at different Reynolds numbers

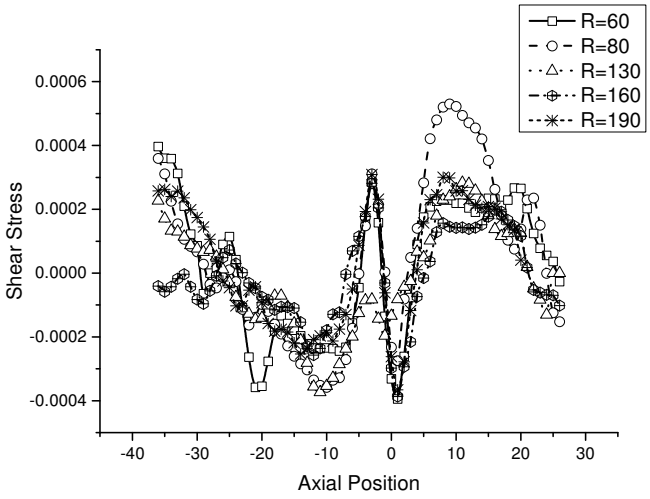

Figure 3.35 Normalized Shear stress (u'v') near wall (1/8 gap distance from cylinder wall) of PIV data at different Reynolds numbers

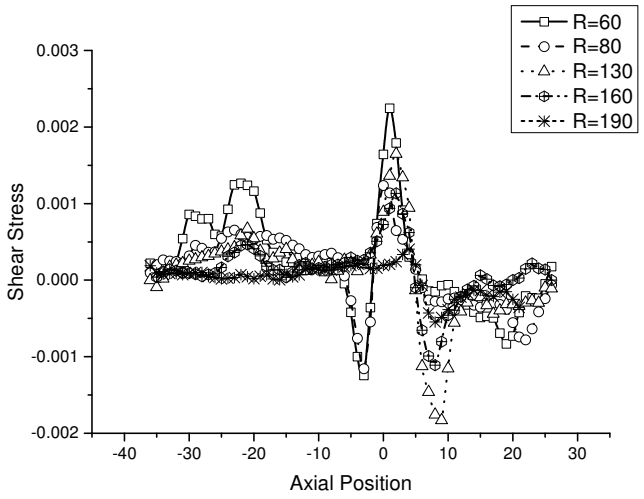

Figure 3.36 Normalized Shear stress (u'w') near wall (1/8 gap distance from cylinder wall) of PIV data at different Reynolds numbers

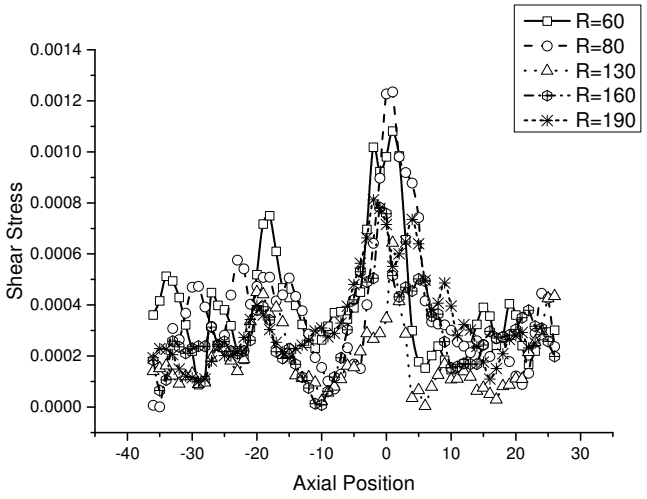

Figure 3.37 Normalized Shear stress (v'w') near wall (1/8 gap distance from cylinder wall) of PIV data at different Reynolds numbers

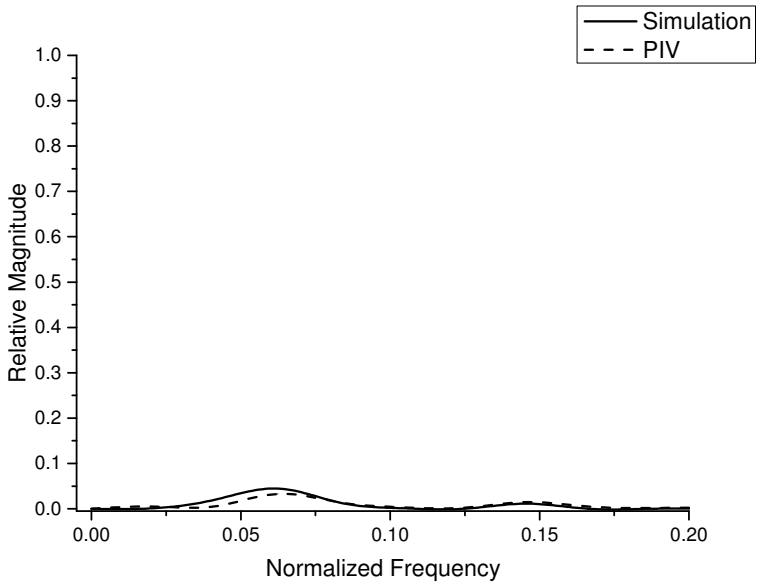

Figure 3.38 2D RANS Power Spectral Density for R=17

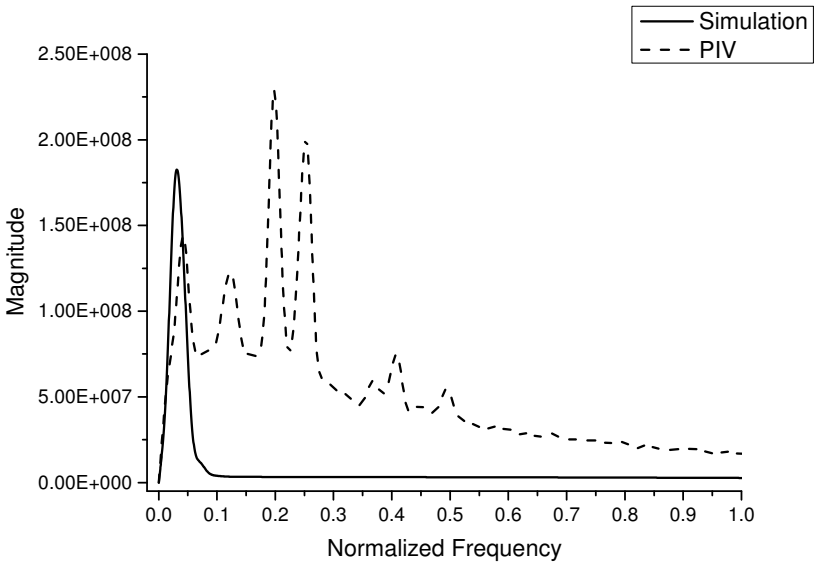

Figure 3.39 2D RANS Power Spectral Density for R=50

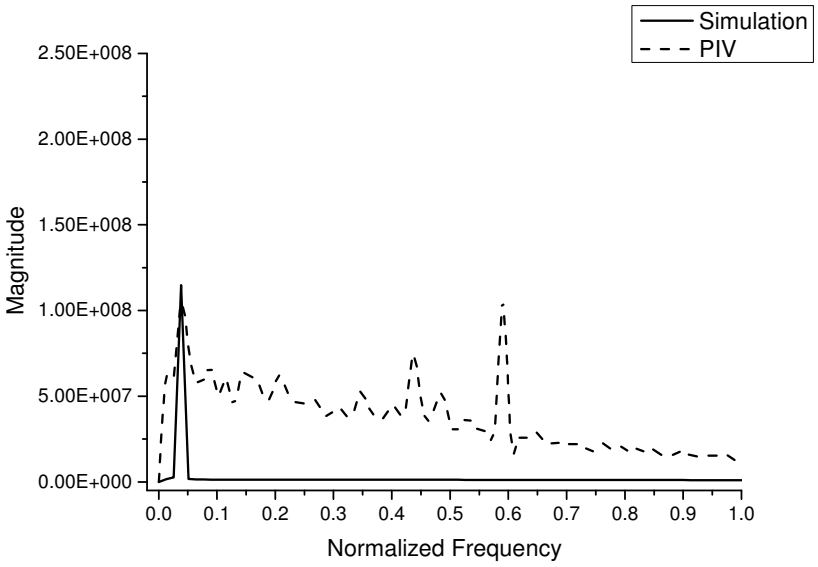

Figure 3.40 2D RANS Power Spectral Density for R=55

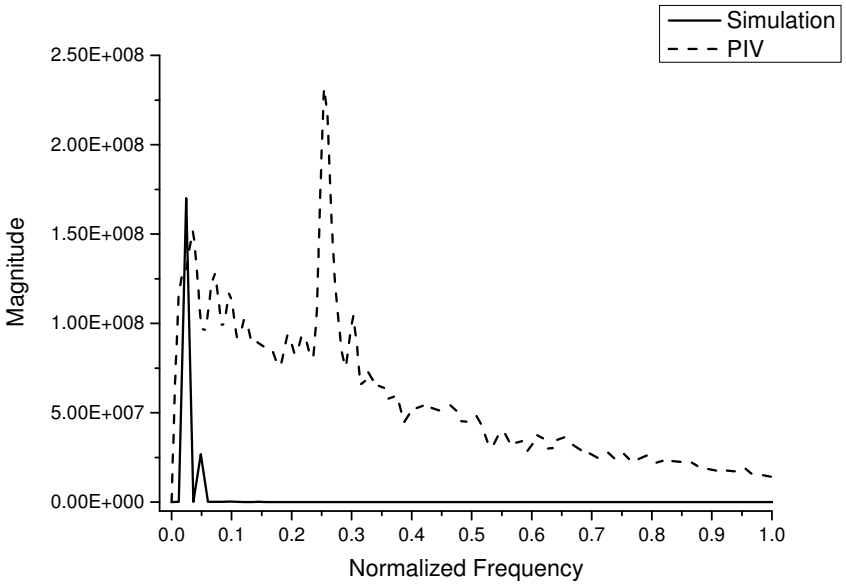

Figure 3.41 2D RANS Power Spectral Density for R=60

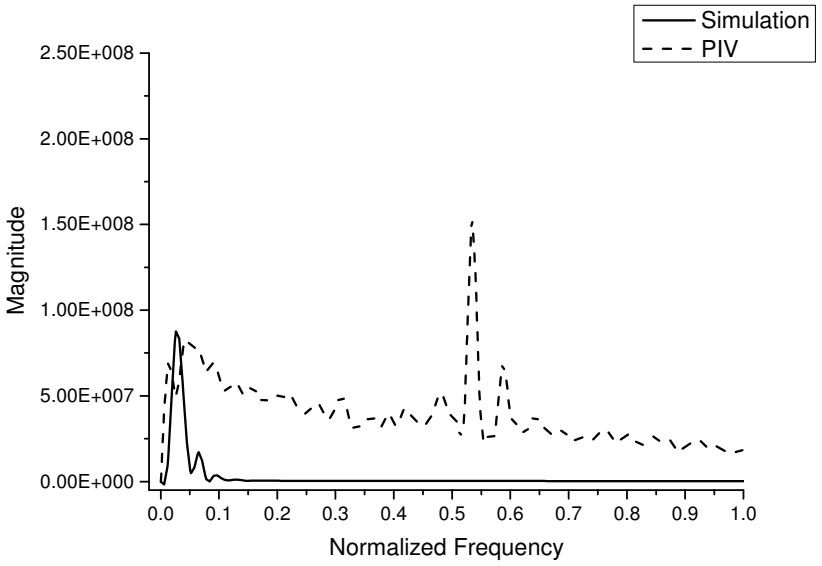

Figure 3.42 2D RANS Power Spectral Density for R=65

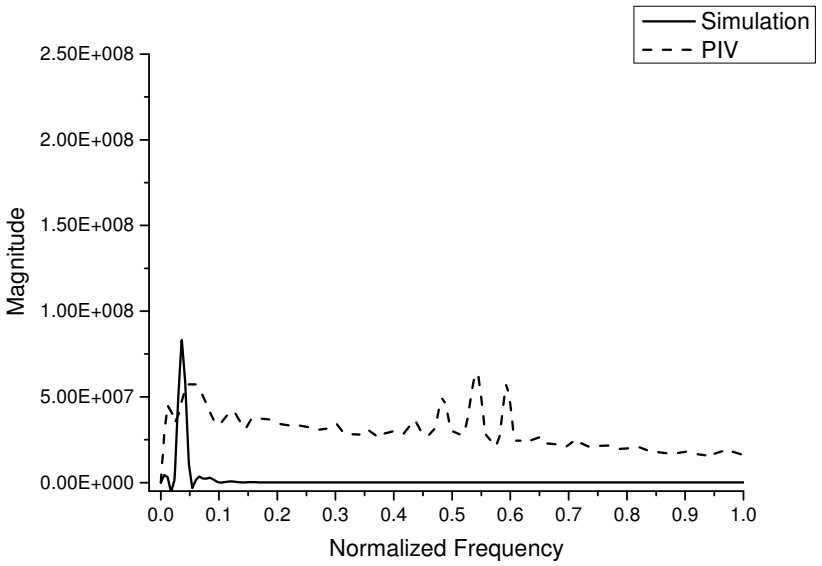

Figure 3.43 2D RANS Power Spectral Density for R=70

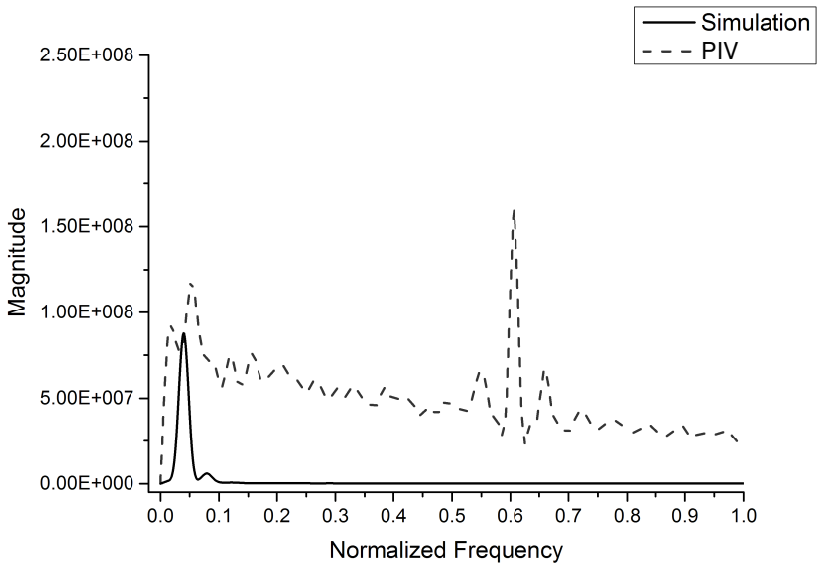

Figure 3.44 2D RANS Power Spectral Density for R=75

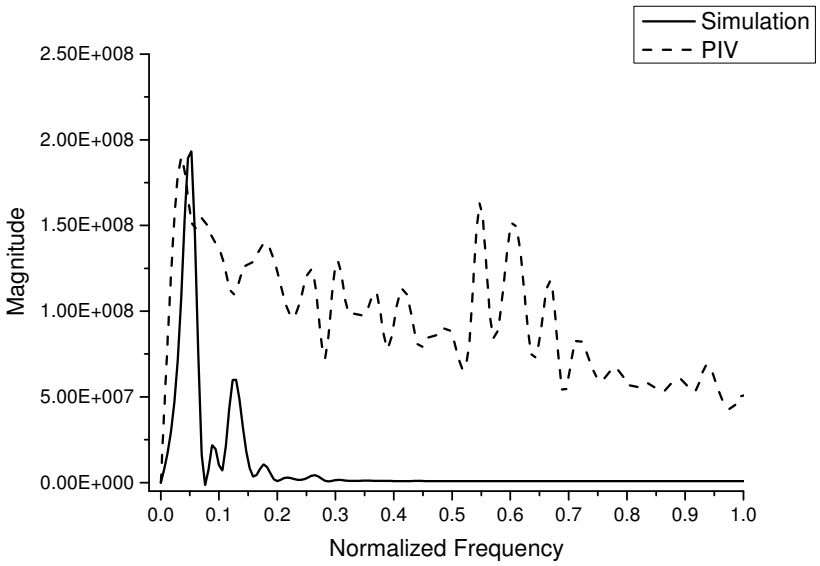

Figure 3.45 2D RANS Power Spectral Density for R=80

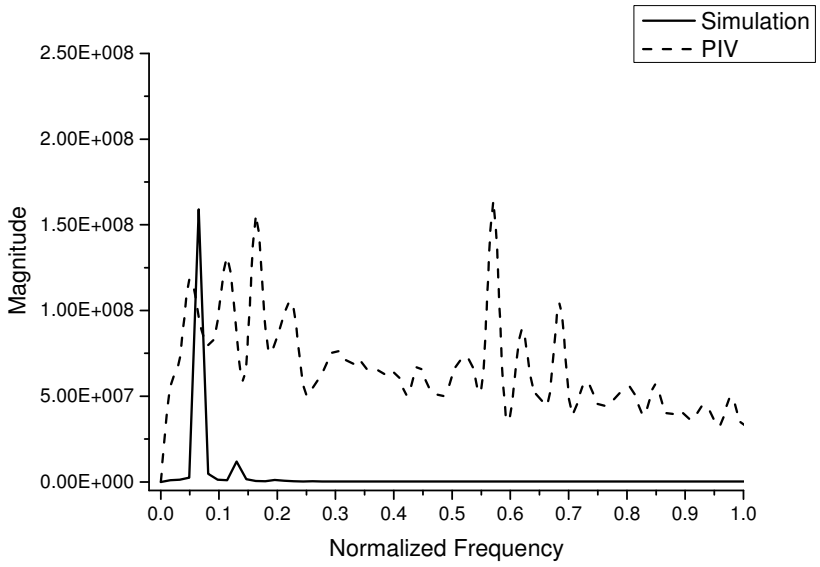

Figure 3.46 2D RANS Power Spectral Density for R=130

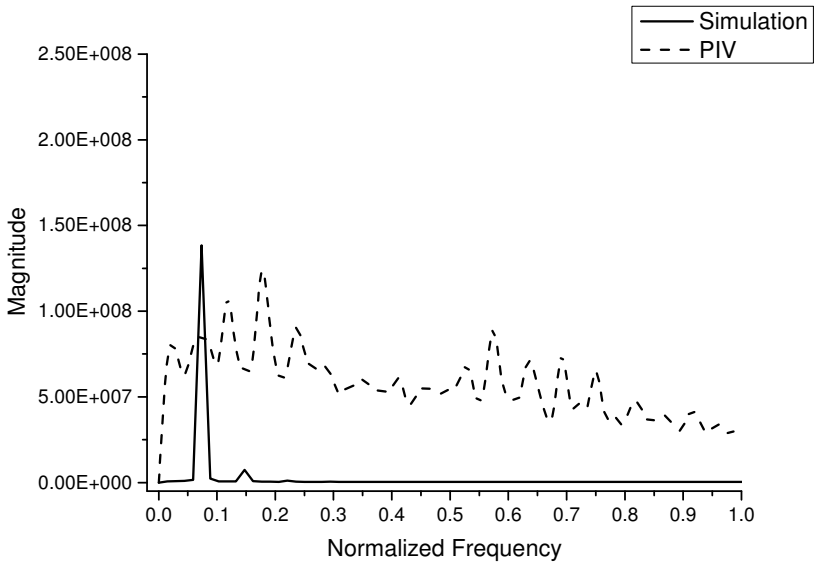

Figure 3.47 2D RANS Power Spectral Density for R=145

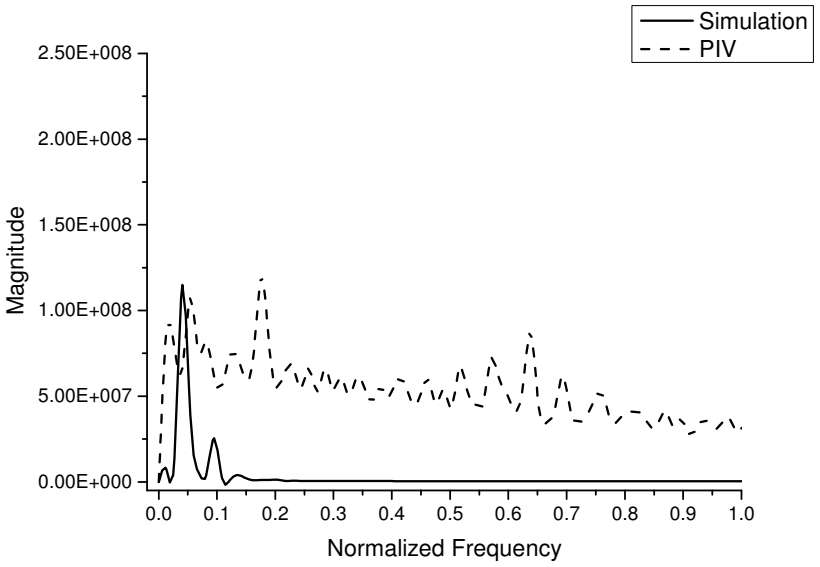

Figure 3.48 2D RANS Power Spectral Density for R=155

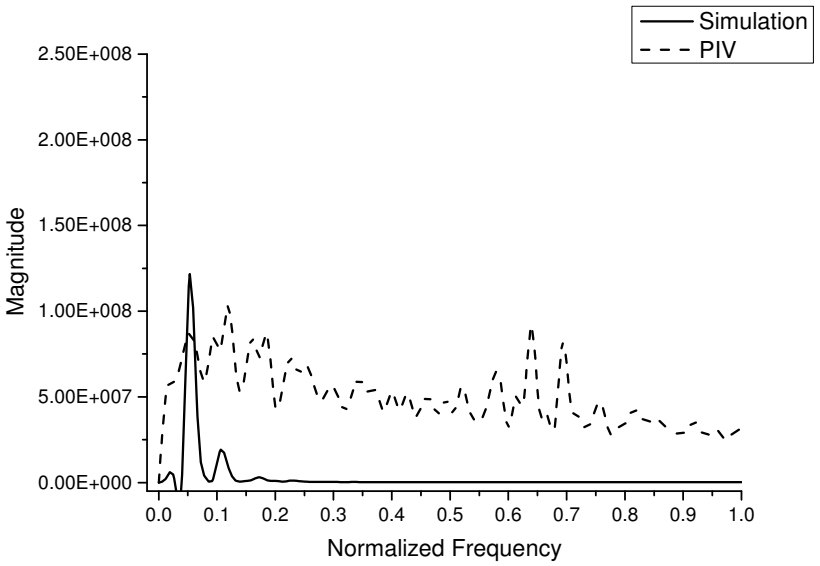

Figure 3.49 2D RANS Power Spectral Density for R=160

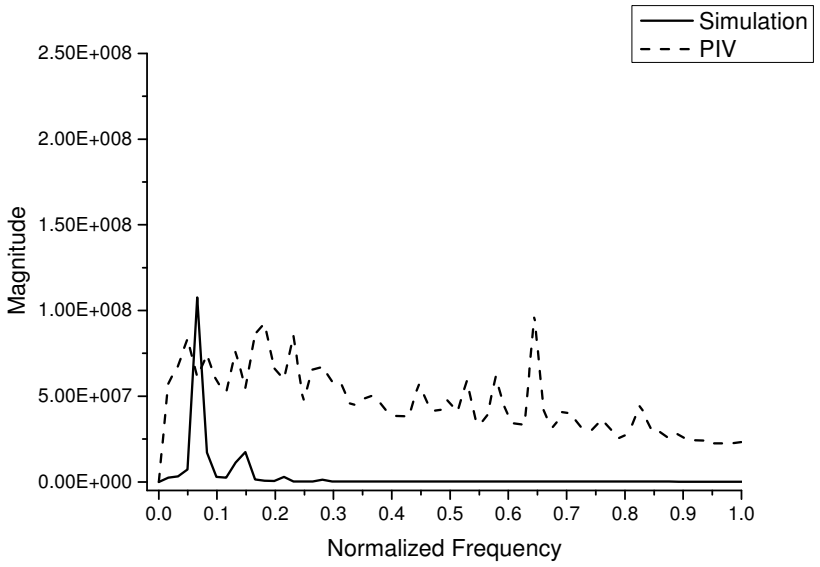

Figure 3.50 2D RANS Power Spectral Density for R=170

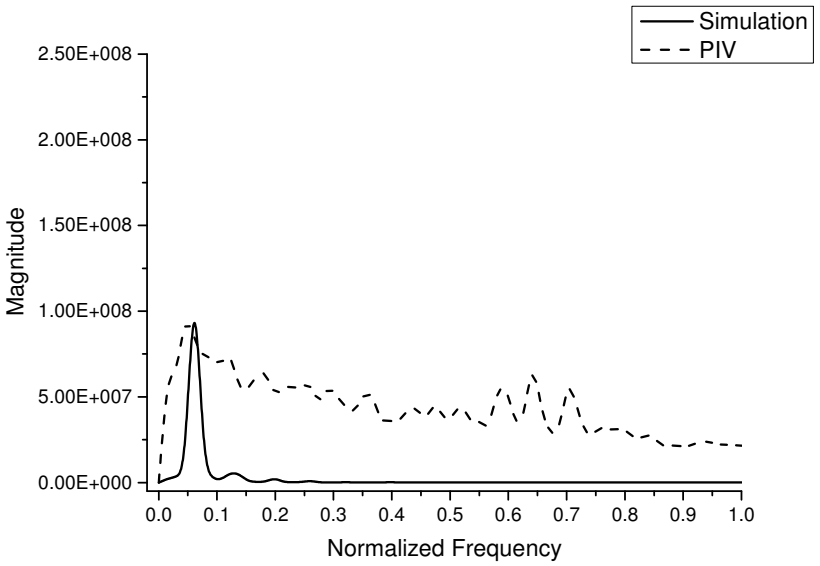

Figure 3.51 2D RANS Power Spectral Density for R=185

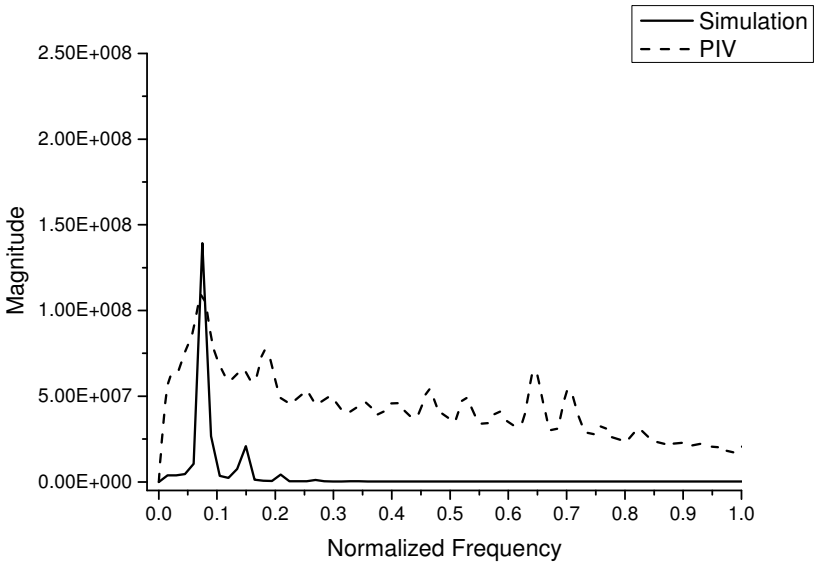

Figure 3.52 2D RANS Power Spectral Density for R=190

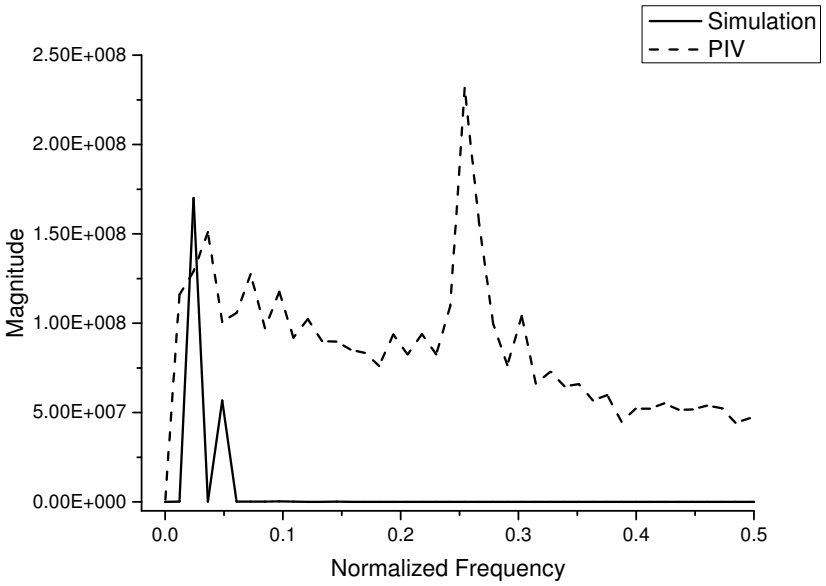

Figure 3.53 3D RANS Power Spectral Density for R=60

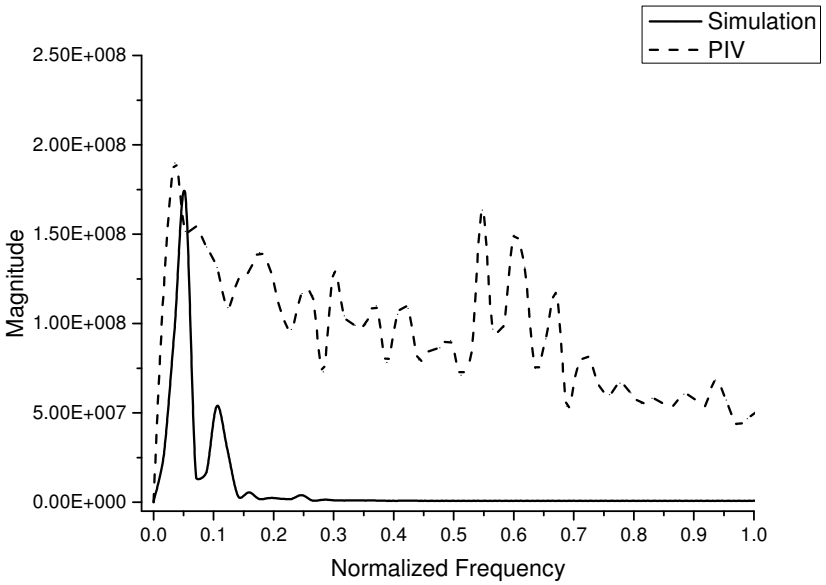

Figure 3.54 3D RANS Power Spectral Density for R=80

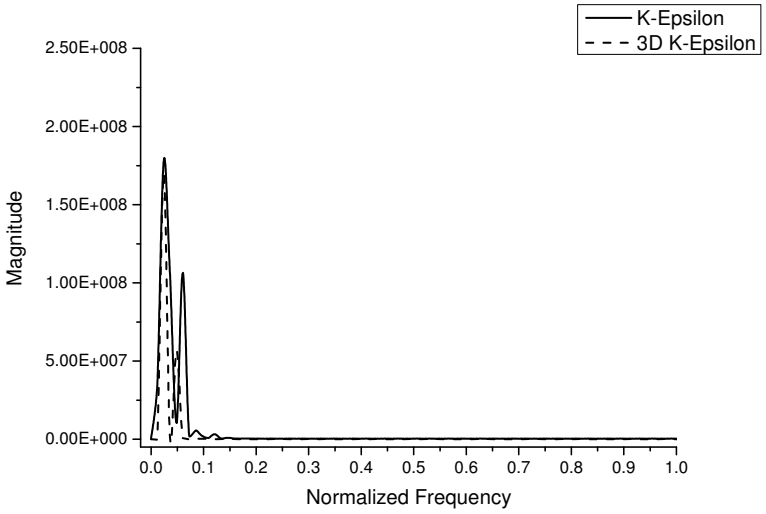

Figure 3.55 2D vs 3D RANS Power Spectral Density for R=60

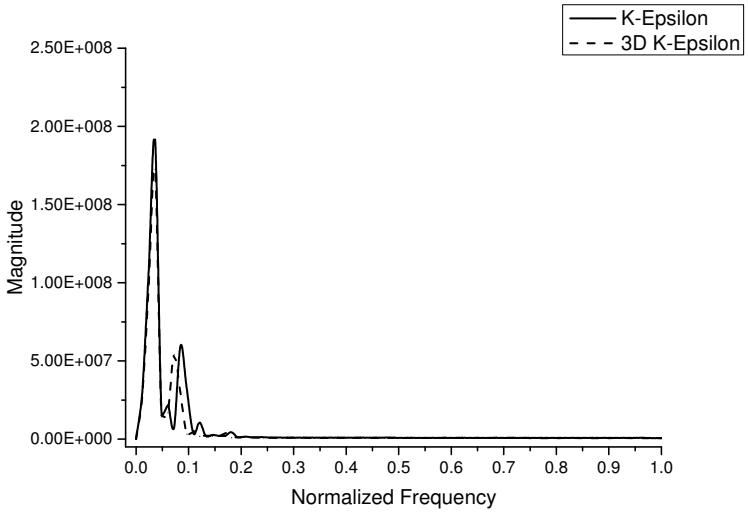

Figure 3.56 2D vs 3D RANS Power Spectral Density for R=80

CHAPTER 4. NUMERICAL INVESTIGATION OF TAYLOR-COUETTE FLOW WITH $k-\omega$ MODEL

A paper in preparation

Abstract

The $k-\omega$ turbulence model was used in 2D and 3D Reynolds-Averaged Navier-Stokes (RANS) Computational Fluid Dynamics (CFD) simulation for a Taylor-Couette flow with a fixed outer cylinder and a rotating inner cylinder. Programs from a finite-volume CFD library, OpenFOAM, were used to discretize and solve the filtered Navier-Stokes equation for unsteady 2D and 3D simulations. The effects of grid resolution were investigated for both the 2D and 3D RANS methods to determine the optimal grid for use in the study. Mean velocities and turbulent kinetic energy predicted using the $k-\omega$ model were compared with stereoscopic particle image velocimetry (stereo PIV) measurements to validate the accuracy of the simulations. Calculation and comparison of the power spectral density demonstrated that the simulation with the $k-\omega$ model accurately captured the important instabilities that lead to azimuthal wave motion in the Taylor-Couette flow. Finally, results using the $k-\omega$ model and the $k-\varepsilon$ model were compared to investigate the differences between the turbulent models in modeling this Taylor-Couette flow.

Introduction

The fluid flow filled in the gap between two concentric cylinders, with either or both cylinder rotating, is known as Taylor-Couette flow. At low velocities, the flow simply circles about the inner cylinder. If the velocity of the rotating cylinder exceeds a certain critical value which is expressed in terms of the Reynolds number ($Re = \omega r_i (r_i - r_o) / \nu$, the ratio of inertial forces to viscous forces), in stabilities form, resulting in the formation of a vortex flow regime. This flow is called Taylor vortex flow and is of great interest since the gentle mixing motion of the vortices provides high values of mass transfer coefficients, which makes Taylor-Couette flow important in many industrial application. For example, investigators have explored the utility of using Taylor-vortex devices as bioreactors, for the cultivation of algae, for membrane separation, and for filtration.

Previous research has shown that as the Reynolds number increases from lower to higher values, the Taylor-Couette flow becomes increasingly complex. With increasing Reynolds number, the flow undergoes a series of transitions first from circular Couette flow to Taylor vortex flow (TVF), then to the state of wavy vortex flow (WVF), progressing to modulated wavy vortex flow (MWVF), and finally to turbulent Taylor vortex flow (TTVF). Because of the complexities that arise in this seemingly simple flow, Taylor-Couettte flow has been studied for over a century. Initially, Taylor-Couette flow was investigated by simple visual observation. AS technology progressed, electric measurements (Davey, 1962; Coles, 1964; Walden and Donnelly, 1979) and then laser Doppler velocimeter (LDV) (Fenstermacher et al., 1979; Brandstater and Swinney, 1987) were used in the measurements resulting in a major advance in the study of the flow. In recent years, Particle Image Velocimetry (PIV) has become a widely-used technology in fluid measurement, because it provides both visual and analytical information in turbulent flows, as PIV can simultaneously measure velocity field data at a large number of points over a two-dimensional or even three-dimensional domain (Wereley and Lueptow, 1998;

Wang et al., 2005; Dutcher and Muller, 2009). By comparison, Laser Doppler velocimetry provides only pointiest data. In chapter two of this thesis, experimental research work was described where stereo PIV was used to investigate the present Taylor-Couette flow. These experimental results are also used for comparison to CFD results in the present chapter.

Computational Fluid Dynamics (CFD) is the analysis of systems involving fluid flow, heat transfer and associated phenomena such as chemical reactions by means of computer-based simulation. The technique is very powerful and spans a wide range of industrial and non-industrial application areas. The numerical study of Taylor-Couette flow has developed rapidly a computer technology has improved in recent decades. Different modeling methods of computational fluid dynamics (CFD) have been developed to study turbulent flows (Swift et al., 1982; Moser et al., 1983; Marcus, 1984; Salhi et al., 2012). Compared to other methods, such as Large Eddy Simulation (LES) where only the smallest turbulent scales are modeled, and Direct Numerical Simulation (DNS) where all the scales of turbulence are directly computed (Kravchenko and Moin, 1997; Liao et al., 1999; Dong, 2007, 2008; Friess et al., 2013), Reynolds-averaged Navier-Stokes (RANS) which models all of the turbulence, consumes less time and computational resources which makes the RANS method the most common and economic method when applicable. Compared to experimental studies, numerical investigations of Taylor-Couette flow in the highly turbulent regimes are lacking. In the present work, turbulent Taylor-Couette flow is investigated using a RANS CFD simulation.

The Power Spectral Density function describes how the power of a signal or time series is distributed over the different frequencies. It is one of the most widely used methods in signal analysis and can be regarded as the analysis of the variance of a time series using sinusoids. The power spectral density can be a powerful tool to study and analyze the various flow regimes and transitions in Taylor-Couette flow. There have been very few numerical studies of Taylor-Couette flow using power spectral density analysis.

Power spectral density analysis of the unsteady CFD simulations for highly turbulent Taylor-Couette flow is presented in this work.

Finally, there are numerous turbulent models that can be used in the RANS methodology. In the previous chapter, the $k-\varepsilon$ was investigated. Another powerful and commonly used two-equation turbulence model used in RANS simulation is the $k-\omega$ model. In order to investigate the difference between two turbulent models of RANS in the simulation of Taylor-Couette flow, simulation results generated using both models are compared in this chapter.

Experimental Section

Experiment Apparatus

The experiments were described in detail in chapter two, so only a brief summary of the experiments is presented here for completeness. The inner cylinder of the Taylor-Couette flow in present work had a diameter of $6.985cm$ while the outer cylinder had a diameter of $9.525cm$, resulting in an annular gap width between cylinders was $1.27cm$. Both cylinders were made of Plexiglas, and the outer cylinder was enclosed in a square Plexiglas box. The length of the cylinders was $43.2cm$. The inner cylinder was driven by a compumotor control system with digital controller.

The working fluid in the apparatus was a mixture which had a refractive index matched with that of the Plexiglas (1.4905). The mixture contained water (90% by volume) and glycerol (10% by volume) with sodium iodide and small quantities of sodium thiosulfate added into the mixture. Silver-coated hollow glass spheres with a density of 1.6 g/cm^3 and an average diameter of 13 μm were used as the PIV seed particles. The density of the working fluid was 1.85 g/cm^3, and the kinematic viscosity of the working fluid was $1.71\times\ 10^{-6}\ m^2/\text{s}$. For this apparatus, the critical value of Reynolds number was $Re_c = 99.53$.

PIV Measurement

The PIV system used in present work was a LaVison Inc. high speed stereoscopic PIV system. A thin laser sheet which was formed by the combination of a spherical plano-convex lens and a cylindrical planoconcave lens was reflected by a mirror and then passed through the outer cylinder in the center. The laser sheet was carefully aligned in the meridional plane to avoid a possible anomalous apparent radial velocity component caused by the azimuthal path of the particles through the laser sheet. PIV image pairs were captured in the illuminated plane at different Reynolds numbers. The images which measured 1024 pixels axially and 1024 pixels radially. The images was divided into interrogation regions measuring 32×32 pixels with 50% overlap between adjacent interrogation regions, and these interrogation regions were used to calculate the velocity vectors in the images. The velocity vector spacing in the resulting velocity fields was $0.4mm$.

At the beginning of experimental measurement, the inner cylinder was accelerated from rest to R=55 at a constant angular acceleration of $0.314rad/s^2$, and then maintained constant at this velocity for half an hour before increasing to higher velocity at a constant angular acceleration of $0.314rad/s^2$ or reducing at a constant angular acceleration of $0.126rad/s^2$. In order to avoid hysteresis effects, the inner cylinder maintained at the prescribed angular velocity for approximately 10 minutes before PIV data were collected.

CFD Methodology

Governing Equations

The general Navier-Stokes equation can be expressed as:

$$\frac{\partial \rho}{\partial t} + \nabla \cdot (\rho V) = 0 \tag{4.1}$$

$$\rho(\frac{\partial V}{\partial t} + V \cdot \nabla V) = -\nabla P + \nabla \cdot T + f \tag{4.2}$$

where V is the fluid velocity vector, ρ is the fluid density, P is the pressure, T is stress tensor, and f represents body forces acting on the fluid.

Since the pseudo random nature of a turbulent flow precludes an economical simulation of the turbulent velocity field through direct numerical solution of the Navier-Stokes equations (except in the limit of lower Reynolds number turbulent flow), Reynolds decomposition is often used to describe turbulent velocity.

$$u(t) = \bar{u} + u'(t) \tag{4.3}$$

Velocity is decomposed into a steady mean value of velocity $\bar{u}$ with a fluctuating component $u'(t)$ superimposed on it. Using Reynolds decomposition, turbulent flow can be characterized in term of mean values of fluid properties, and some statistical properties of their fluctuation and the effects of fluctuations on the mean flow can be investigated. Similarly, the flow variables P can be represented as the sum of a mean and a fluctuating component. The ensemble average is then taken for both the continuity equation and the momentum equations in Navier-Stokes equation resulting in equations for the mean flow. This yields the Reynolds-averaged Navier-Stokes equations, as follows

$$\frac{\partial \rho}{\partial t} + \nabla V = 0 \tag{4.4}$$

$$\frac{\partial \bar{u}}{\partial t} + \nabla \cdot (\bar{u}V) = -\frac{1}{\rho}\frac{\partial P}{\partial x} + \nu \nabla \cdot \nabla \bar{u} + \frac{1}{\rho}[\frac{\partial(-\rho\overline{u'^2})}{\partial x} + \frac{\partial(-\rho\overline{u'v'})}{\partial y} + \frac{\partial(-\rho\overline{u'w'})}{\partial z}] \tag{4.5}$$

$$\frac{\partial \bar{v}}{\partial t} + \nabla \cdot (\bar{v}V) = -\frac{1}{\rho}\frac{\partial P}{\partial x} + \nu \nabla \cdot \nabla \bar{v} + \frac{1}{\rho}[\frac{\partial(-\rho\overline{u'v'})}{\partial x} + \frac{\partial(-\rho\overline{v'^2})}{\partial y} + \frac{\partial(-\rho\overline{v'w'})}{\partial z}] \tag{4.6}$$

$$\frac{\partial \bar{w}}{\partial t} + \nabla \cdot (\bar{w}V) = -\frac{1}{\rho}\frac{\partial P}{\partial x} + \nu \nabla \cdot \nabla \bar{w} + \frac{1}{\rho}[\frac{\partial(-\rho\overline{u'w'})}{\partial x} + \frac{\partial(-\rho\overline{v'w'})}{\partial y} + \frac{\partial(-\rho\overline{w'^2})}{\partial z}] \tag{4.7}$$

where V is the mean flow velocity vector, ρ is the flow density, and P is the pressure. The terms in the square brackets on the right hand side of the momentum equations represents the additional turbulent apparent stress as which result from the velocity fluctuations. These extra turbulent stresses are called the Reynolds stresses. Since no additional equations are available to solve the extra unknown quantities that is, the

Reynolds stresses. it is necessary to develop turbulence models to predict the Reynolds stresses and the scalar transport terms and close the system of mean flow equations in order to be able to compute turbulent flows with the RANS equations.

Turbulence Model

The two-equation models are presently by far the most widely used and validated in the RANS methodology. There are many two-equation models for engineering and environmental flows that are used in practice. Among them are the $k-\varepsilon$ and $k-\omega$ models, which are the two most widely used models. In the $k-\varepsilon$ model the kinematic eddy viscosity ν_t is expressed as the product of a velocity scale $\vartheta = k$ and a length scale $l = k^{3/2}/\varepsilon$. The rate of dissipation of turbulence kinetic energy ε is not the only possible length scale determining variable. Kolmogorov (Kolmogorov, 1942) introduced the first complete model of turbulence, a two-transport-equation $k-\omega$ model solving for kinetic energy k and turbulent frequency ω. In addition to having a modeled equation for the kinetic energy contained in the turbulent fluctuations, k, he introduced a second parameter ε that he referred as "the rate of dissipation of energy in unit volume and time". The reciprocal of ε serves as a turbulence time scale. The most prominent alternative to the $k-\varepsilon$ model is the $k-\omega$ model proposed by Wilcox (Wilcox, 1988, 1993, 1994), which uses the turbulence frequency $\omega = \varepsilon/k$ (dimensions s^{-1}) as the second variable. In the $k-\varepsilon$ model, the eddy viscosity is given by:

$$\mu_t = \rho k/\omega \tag{4.8}$$

As in the $k-\varepsilon$ model that was described in the previous chapter, the Reynolds stresses are calculated as usual for two-equation models by using the Boussinesq expression:

$$\tau_{ij} = 2\mu_t S_{ij} - \frac{2}{3}\rho k \delta_{ij} \tag{4.9}$$

where k, same as in the $k-\varepsilon$ model, is the turbulent kinetic energy per unit mass, μ_t is the turbulent (or eddy) viscosity, $\rho C_\mu \frac{k^2}{\varepsilon}$, and S_{ij} is the mean strain-rate tensor. The

standard $k-\omega$ model (Wilcox, 1988), which is used in OpenFOAM, uses the following transport equations for k and ω:

$$\rho\frac{\partial k}{\partial t}+\rho\overline{u_j}\frac{\partial k}{\partial x_j}=\tau_{ij}\frac{\partial \overline{u_i}}{\partial x_j}-\beta^*\rho k\omega+\frac{\partial}{\partial x_j}[(\mu+\sigma^*\mu_t)\frac{\partial k}{\partial x_j}] \tag{4.10}$$

$$\rho\frac{\partial \omega}{\partial t}+\rho\overline{u_j}\frac{\partial \omega}{\partial x_j}=\alpha\frac{\omega}{k}\tau_{ij}\frac{\partial \overline{u_i}}{\partial x_j}-\beta^*\rho\omega^2+\frac{\partial}{\partial x_j}[(\mu+\sigma\mu_t)\frac{\partial \omega}{\partial x_j}] \tag{4.11}$$

with closure coefficients: $\alpha=5/9$, $\beta=3/40$, $\beta^*=0.09$, $\sigma=1/2$, $\sigma^*=1/2$, and auxiliary relations: $\varepsilon=\beta^*\omega k$.

The differences between the first equation in each model, the k-equations, are generally small. It does not matter whether one is using the $k-\varepsilon$ model or the $k-\omega$ model; both include a production term, a destruction term, and a turbulent and a viscous diffusion term. However, the differences between the second transport equation in the 7 formulations of the $k-\varepsilon$ and $k-\omega$ models are quite significant. The $k-\varepsilon$ model is generally thought of as the more general model, with good predictions for both free shear flows and wall bounded flows. However, it typically performs poorly for complex flows involving severe pressure gradients, boundary layer separation, and strong streamline curvature. The $k-\omega$ model on the other hand, performs better in wall-bounded flows, especially those with adverse pressure gradients. The basic two equations models, the $k-\varepsilon$ and the $k-\omega$ model, are not the exactly same turbulence models, and their accuracy is case-dependent. Just as for the $k-\varepsilon$ model, the "tunability" of the $k-\omega$ model is limited to coefficients and damping functions.

Method of Solution

In the present work, the OpenFOAM (Open Source Field Operation and Manipulation) software package, which is an open source CFD software package for the development of customized numerical solvers, containing pre- and post-processing utilities for the implementation of computational fluid dynamics, is used in the CFD simulation of Taylor-Couette flow. OpenFOAM includes a large range of solvers each designed for a

specific class of problem. The equations and algorithms differ from one solver to another so that the selection of a solver involves the user making some initial choices on the modeling for the particular case of interest. RANS algorithms and codes are part of the OpenFOAM software package as are various turbulence models for incompressible and compressible flows. Users can choose the turbulent models in the package to use to close the RANS equations.

In present work, both 2D and 3D meshes were generated using the OpenFOAM package. In order to optimize the precision and computation economy of RANS simulations, which are strongly dependent on grid resolution, a pre-simulation was carried out to determine the optimal choice of grid resolution for the 2D and 3D simulations of the Taylor-Couette flow. A grid-resolution study for both the 2D and 3D simulations using the linear (second order central) scheme for interpolation and Gaussian integration for velocity gradient was performed. The two finest grid resolutions for case that 2D were investigated were 50×1400 and 75×2100, and the finest grid sizes for 3D case that were investigated contained 946400 and 4258800 cells. The power spectral density was calculated using the same method as was described in chapter two. In order to compare the difference between the predictions for the $k - \varepsilon$ and $k - \omega$ models, comparison of power spectral density for two models is presented and investigated in the present work.

Grid Resolution Comparison

Three velocity profiles for the Taylor-Couette flow, representing the axial, radial, and azimuthal velocity components for the coarse (a cell number which equals to 70000) and the fine (a cell number which equals to 157500) 2 dimensional simulation grid resolutions are compared with each other in Fig. 4.2. It can be seen from the figure that profiles for all three velocity components, different grid resolutions all agree well with each other. This demonstrates that the coarse grid resolution provides the same simulation result as the finer grid resolution. Performing the simulation with the finer grid would con-

sume much more time and computer resources than the coarse grid while providing the same result. Based on these comparison, the coarse grid is the better choice for the 2D simulation investigation.

Three profiles at different 3D simulation grid resolutions for the radial, axial, azimuthal velocities are compared in Fig. 4.3. In this 3D simulation grid comparison, two grid resolutions were compared, a coarse grid which had 946400 cells, and a finer grid which had 4258800 cells. All three velocity profiles for the coarse grid resolutions exactly matched with the finer grid results, demonstrating that the same simulation results can be achieved from both grid resolutions. Just as for the 2D simulation, the coarse grid saves time and computational sources compared to the finer grid, so using the coarse grid is a better choice than using the finer one.

Based on the grid resolution study, the coarse grids for both the 2D (with 70000 cells) and the 3D (with 946400 cells) simulations were chosen for simulations performed in the present work.

Results and Discussion

In this section, mean velocities, turbulence statistics, and the power spectral density results of the RANS simulations using the $k-\omega$ model are compared with the results from PIV experiments to determine how accurately the RANS model predicts the turbulent Taylor-Couette flow. Then, the difference between the power spectral density results for the $k-\omega$ model and the $k-\varepsilon$ model reported in Chapter 3 are compared. For all of these comparisons, the RANS simulations were run for sufficiently long times to allow for the flow to reach a dynamic steady state.

Mean Velocity and Velocity Statistic Results

In this section, mean velocities and velocity statistics for turbulent Taylor-Couette flow at different Reynolds numbers are compared between the RANS simulations and PIV data. Velocities and turbulent statistics are compared along in a line segment located at the center of the gap between the cylinders. In 2D simulations, the simulation plane was the one captured in the PIV data, while for 3D simulation a plane was cut from the simulation results to match the PIV data.

The mean velocity profiles for axial, radial, and azimuthal velocity components and Turbulent Kinetic Energy (TKE) along the gap centerline at Reynolds number, $R = 60$, are compared bewteen the 2D RANS simulation using the $k-\omega$ model and the PIV data, in Fig. 4.4. It can be seen in the figure that the axial and radial velocity profiles of simulation, which were represented by symbols, matched very well with the PIV data, which were presented using lines, except for very small variations in the axial velocity near the outflow boundary. Excellent agreement is also seen between simulation and experiment for the azimuthal velocity (which is more difficult to measure experimentally). In general, at $R = 60$ velocity profiles predicted by the $k-\omega$ model agreed with the experimental data better than those predicted by model the $k-\varepsilon$ model that were presented in the last chapter. In the TKE comparison, the $k-\omega$ model agreed with the PIV data at $R = 60$ except for a small underprediction in the peak magnitude. At Reynolds number 60, it is apparent that the 2D RANS method with the $k-\omega$ model accurately simulates the turbulent Taylor-Couette flow.

In order to more generally verify the accuracy of the $k-\omega$ model, the rotation velocity of inner cylinder was increased to test the $k-\omega$ model at higher Reynolds numbers. In Fig. 4.5, comparisons are made for $R = 80$. As the rotational velocity increases, the magnitude of the azimuthal velocity that is directly driven by the angular velocity of the rotating inner cylinder is seen to increase while the magnitudes of the axial and radial velocities remain unchanged. The $k-\omega$ model results for all three mean velocity

profiles compare well with the experiment data. In the comparison of turbulent kinetic energy, the magnitude of the TKE had the same trend as was mentioned in the last chapter, namely that it increases with increasing angular velocity of the inner cylinder demonstrating that the flow becomes more turbulent with higher Reynolds number. The TKE of the simulation and the PIV results agree well, and demonstrate the simulation's accuracy at this Reynolds number.

In Fig. 4.6, the mean velocity profiles are compared at R=130 between PIV and simulation. Once again, the simulation results agree with the PIV data well. Also, the magnitude of the azimuthal velocity and the TKE increase with increasing of Reynolds numbers, while the other two mean velocities barely change.

As Reynolds number is increased even higher to $R = 160$ and $R = 190$, the $k - \omega$ simulation results continue to have good agreement with the experiment data, as shown in Figs. 4.7 and 4.8. The same trends of increasing magnitude of azimuthal velocity and TKE are observed, while the velocity profiles for the other two components remain almost unchanged. The RANS simulation results capture the same shape, magnitude, and trends as the PIV data. Compared with lower Reynolds numbers cases, the velocity profiles for the simulation actually matched better with experiment for the high Reynolds numbers, especially in the azimuthal velocity profile. In the previous chapter, the velocity profiles results for the $k - \varepsilon$ model at high Reynolds numbers had some small variations in the azimuthal velocity profile compared with PIV. The $k-\omega$ model did a better job in simulating the velocity statistics of turbulent Taylor-Couette flow than the $k - \varepsilon$ model at higher Reynolds numbers.

For both low and high Reynolds numbers, the $k-\omega$ model presents a better simulation of the Taylor-Couette flow than the $k - \varepsilon$ model. This is not surprising since the $k - \omega$ model has several advantages compared to the $k-\varepsilon$ model for this flow. In the region of low turbulence when both k and ε approach to zero, the $k-\varepsilon$ model has difficulty dealing with this situation. In Equation 3.12, the rate of dissipation of the ε term includes ε^2/k.

Thus as k goes to zero, numerical problems appear even if ε also goes to zero. In the turbulent flow, k and ε should go to zero in this ratio at low Reynolds number. However, there is no such problem in the $k-\omega$ model. It can be seen in the $k-\omega$ model equations, if k goes to zero the turbulent diffusion term simply goes to zero. The $k-\omega$ model also achieves higher accuracy for boundary layers with adverse pressure gradient. Pressure gradient plays an important role in interpreting the instabilities in the Taylor-Couette flow (Karman, 1934). Higher accuracy in the presence adverse pressure gradients in the boundary layers results in an advantage of the $k-\omega$ model in simulating turbulent Taylor-Couette flow.

Figures 4.9 through 4.13 are the mean velocity profiles for axial, radial, and azimuthal velocity and TKE with comparison between PIV and simulation results near the inner cylinder wall (1/8 of the gap distance from the wall). As can be seen in the figures, all the mean velocities and TKE results for the simulation agree well with the PIV data. Just as at the gap center, the azimuthal and TKE magnitudes follow the same trend where they increase as Reynolds number is increased, while the axial and radial velocities remain unchanged.

In Fig. 4.14, profiles of the mean axial, radial, and azimuthal velocity and TKE along the gap center for the 3D simulation using the $k-\omega$ model are compared with experiment results at $R = 60$. All the simulation mean velocity profiles and the TKE profile agreed well with PIV data with only very small discrepancies. Based on the mean velocity statistics and velocity comparisons at different Reynolds numbers, both the 2 dimensional and the 3 dimensional simulations using the $k-\omega$ model are accurate in the modelling of turbulent Taylor-Couette flow (TTVF). As mentioned in the previous chapter, the 2D simulations require much less time and computer resources in computing the flowfield while yielding almost the same results as the 3D simulations. For this reason, the 2D simulations in present work are a better choice for modelling turbulent Taylor-Couette flow.

In addition to the mean velocity profiles and TKE, turbulence dissipation rates in the flow can also be compared between the PIV and simulation results. These are presented for profiles at the center of the gap for different Reynolds numbers in Figs. 4.15-4.19, and for profiles near the wall (1/8 of the gap distance from the wall) in Figs. 4.20-4.24. The peak in the dissipation rates for both the PIV and CFD results increases as the Reynolds number increases just as the TKE increases. This is expected since the $k-\omega$ model balances TKE production and dissipation. The shape and magnitude of simulation results are very close to those of the PIV data, demonstrating that the simulations accurately model the turbulence dissipation rate. The same trends and agreement between simulation and experiment are found in the dissipation rate results near the inner cylinder wall.

Power Spectral Density Study

The Power Spectral Density (PSD) is one of the most widely used methods in data analysis and can be regarded as the analysis of the variance of a time series using sinusoids. PSD can be helpful in analyzing Taylor-Couette flow. As presented in chapter two, if the flow becomes turbulent, unsteady features in the PSD can be difficult to identify if they become overwhelmed by the broadband turbulent spectrum. However, the results in chapter three indicated that analysis of data from the RANS simulation could provide a better case for using PSD to identify unsteady features in the turbulent Taylor-Couette flow since the turbulence is modelled, not resolved. In this section, the $k-\omega$ model is used in the RANS simulations to verify if the $k-\omega$ model is adequate to model unsteady motions in turbulent Taylor-Couette flow.

First, the PSD is used to analyze the simulation results at Reynolds number $R = 17$, where the traveling azimuthal waves all but disappear in the flow, and the resulting peaks in the PSD are very small. The reults from the RANS simulations and PIV data are plotted in the Fig. 4.25. The relative magnitudes in Fig. 4.25 are the ratio between

power spectrum magnitude at $R = 17$ and the dominant peak magnitude that occurs at $R = 6$. It can be seen in the figure that the result using the $k - \omega$ model is same as the PIV power spectrum. No sharp peak was found in the plot, suggesting no strong traveling azimuthal waves are present in the flow at this rotation velocity, and all the small peaks that are observed at the same normalized frequency in the simulations and the experiments.

Figure 4.26 shows the comparison between the PSD of PIV data and simulation at Reynolds number 50. In the PIV result, there were several peaks which made it difficult to define the wavy motions in turbulent flow. Only one dominant peak occurs in the power spectrum of the simulation which represents an unsteady wavy motion in the turbulent flow. In Fig. 4.26, the dominant peak of the simulation corresponds to the first peak of the PIV result.

The power spectral density of flow at Reynolds numbers $R = 60$, 70, and 80 were shown in Figs. 4.27, 4.28, and 4.29 respectively. The results of the simulation have the same trends that were observed in the PSDs of the simulations using the $k - \varepsilon$ model that were presented in the last chapter. The power magnitude decreases as Reynolds number increases to 70 before increasing following the rise of Reynolds number to 80. One dominant peak is observed in the $k - \omega$ model results that agrees well with the first peak seen in the PIV results. In the simulation results, the turbulent spectrum was modeled and not resolved and thus only unsteady motion contributes to the PSD. Thus, in the simulations of the Taylor-Couette flow, the changes in the unsteady wavy motion with changes in Reynolds number could be identified with the help of power spectral density analysis, and these results could be used to help interpret the PIV results.

As Reynolds number is increased still higher, the peak power magnitude decreased from the value at R=80 before remaining at a lower level as shown in Figs. 4.30 through 4.33. For these high Reynolds number cases, the simulation results using the $k - \omega$ model still captured an unsteady wavy motion in the power spectral density represented

by one dominant peak, which matched with the first sharp peak in the PIV data, and the turbulent spectrum in PIV was of course, unresolved in the simulation. In summary, the 2D RANS simulations using the $k-\omega$ model did suggest that unsteady wave motion exists in turbulent Taylor-Couette flow, as shown in the power spectral density analysis.

In Fig. 4.34, the results from the 3D RANS simulation using the $k-\omega$ model was compared with PIV data at $R = 60$. The 3D results also had one dominant peak that captured the wave length of the unsteady waves in the turbulent Taylor Couette flow. The turbulent spectrum was modeled in the simulation and not resolved, just as in the 2D simulations. A comparison between the 3D and 2D power spectral density results at Reynolds number 60 is presented in the Fig. 4.35. The shapes of power spectral density were the same in the 2D and 3D results. Only a very small difference in the magnitude of the peak was observed. Since the 2D simulations take much less time and computational resources than the 3D, 2D simulations are a better option to analyze the turbulent Taylor Couette flow, since they are inexpensive and faster to solve.

Comparison between $k-\omega$ and $k-\varepsilon$ model in the Power Spectral Density Study

The results from the $k-\omega$ and $k-\varepsilon$ model simulations were compared using power spectral density analysis. In Fig. 4.37, the two models are compared at Reynolds number $R = 60$. It can be seen in the figure that both models have the same PSD shape, with a single dominant peak in the power spectrum. There was no difference between two models in the normalized frequency corresponding to the dominant peak location in the PSD. The only variation was in the power magnitude of the dominant peak, but the difference was small. A comparison of the two models at Reynolds number $R = 70$ is presented in Fig. 4.38. The shapes of the PSD for both simulations are were still identical to each other, while a small variation in the power magnitude of the dominant peak is still observed. However, the normalized frequencies corresponding to the dominant peak

were different. When compared with Fig. 4.28 (the PSD of the experiment data at R = 70), it can be seen that the peak using the $k-\omega$ model is closer to the first peak in the PIV results. This suggests that the $k-\omega$ model is more accurate than $k-\varepsilon$ model in this case. For $R = 80$, the same observation, as $R = 70$ is found that is the $k-\omega$ model and $k-\varepsilon$ model results have identical shapes and magnitudes, and a difference in the peaks normalized frequencies. Using Fig. 4.39 as a reference, the $k-\omega$ model is a the better choice in this case since its peak matched exactly with the first peak of the PIV data. At Reynolds number 130, the $k-\omega$ and $k-\varepsilon$ model had the same power spectrum shape and peak frequency, but a variation in the peak magnitude. Figs. 4.41, 4.42, and 4.43 are compared at Reynolds numbers 145, 160, and 190, respectively. All the figures show similar features, with the same shape and magnitude of the power spectrum, and difference in the dominant peaks normalized frequency. When compared with PIV results, although the difference between two models was small, the $k-\omega$ model had an advantage in the power spectrum calculation.

Summary and Conclusion

In this chapter, Reynolds-averaged Navier-Stokes equation simulations using the $k-\omega$ model turbulence model were performed for turbulent Taylor-Couette flow, and compared with particle image velocimetry experiments data which were captured in an experimental apparatus of the same geometry as the simulations. The $k-\varepsilon$ model and the $k-\omega$ model are the most common turbulent models used in RANS simulations. The $k-\varepsilon$ model was validated in the previous chapter, and shown to be accurate in simulating velocity statistics and power spectral density for turbulent Taylor-Couette flow. In order to test the $k-\omega$ model, all the same procedures are done in this chapter as were done for the $k-\varepsilon$ model. The effect of different grid resolutions on the velocity statistics using second order central schemes for interpolation and second order Gaussian integration,

and explicit non-orthogonal correction as the gradient scheme were studied in order to determine the effect of these parameters on the accuracy of the simulations. A coarse grid and a finer grid were investigated for both 2D and 3D simulations in order to find the appropriate resolution for using the investigation. The low resolution grid showed both efficiency and accuracy when compared with the high resolution grid results. Using the coarse grid, mean velocity profiles for the axial, radial, and azimuthal components and the turbulent kinetic energy using the $k-\omega$ model were compared with PIV data. The comparison showed both the 2D and 3D RANS methods using the $k-\omega$ model accurately simulated the turbulent Taylor-Couette flow.

A study of power spectral density was also presented for the $k-\omega$ model. 2D PSD results had the same trends as those found for the $k-\varepsilon$ model and agreed well with PIV results. 3D results were compared with 2D results and PIV data and showed the similar accuracy as the 2D simulations, demonstrating that the 2D simulation was a good option since it was inexpensive and fast compared to the 3D simulations while yielding similar results. The good comparison of both velocity statistics and power spectral density between the simulations and PIV data indicated that RANS with the $k-\omega$ model was able to accurately capture the important characteristics of all the turbulent Taylor-Couette flow.

In the end, a comparison of the PSD results for the $k-\omega$ model and the $k-\varepsilon$ model was made to find which was the better choice in predicting the PSD. Power spectral density results of the $k-\omega$ model and $k-\varepsilon$ model were almost identical to each other, except for small differences in the normalized frequency which corresponded to the single dominant peak. Since the $k-\omega$ model peaks in PSD matched with PIV data better than the $k-\varepsilon$ model peaks, the $k-\omega$ model was deemed the better option for PSD analysis.

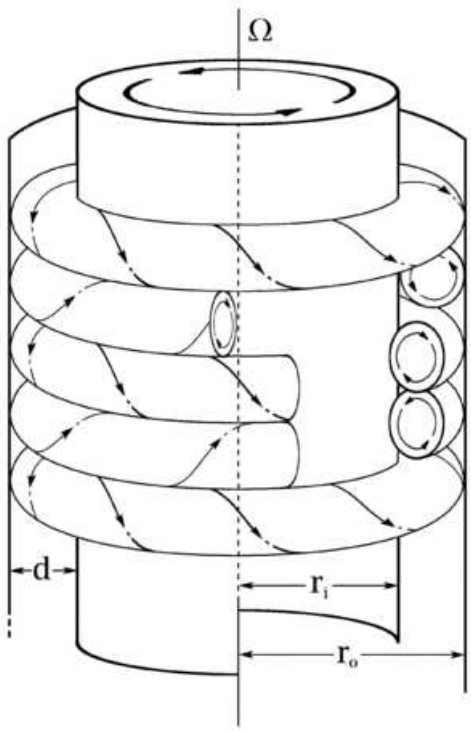

Figure 4.1 Vortex formation of Taylor-Couette Flow (©2000, Mike Minbiole and Richard M. Lueptow)

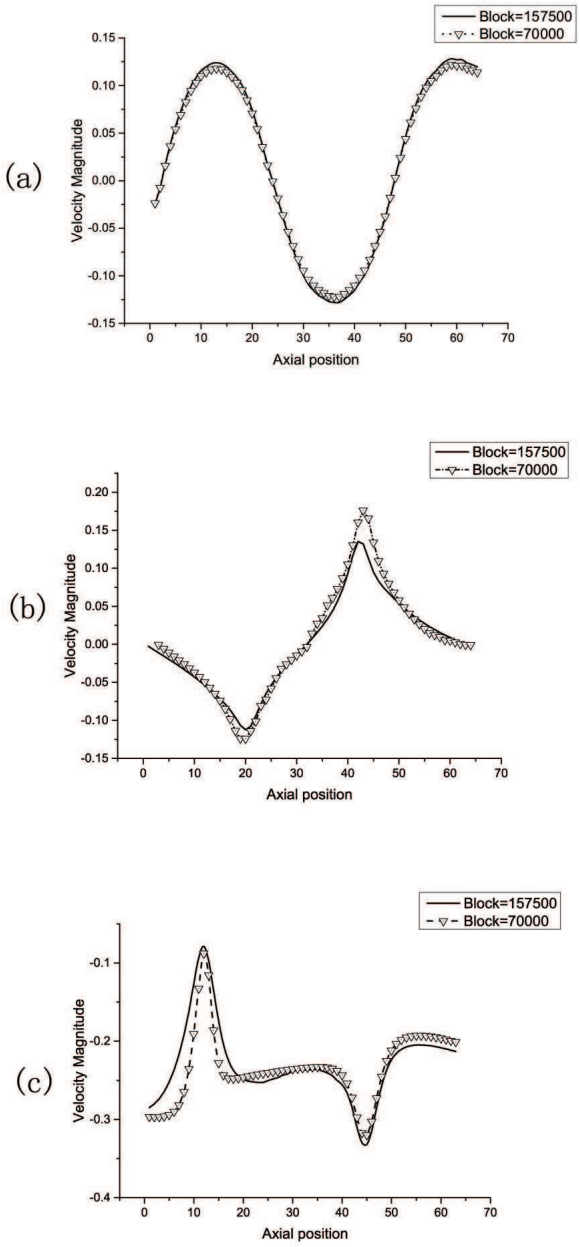

Figure 4.2 Grid resolution comparison of 2D: (a) Axial Velocity (mm/s), (b) Radial Velocity (mm/s), (c) Azimuthal Velocity (mm/s)

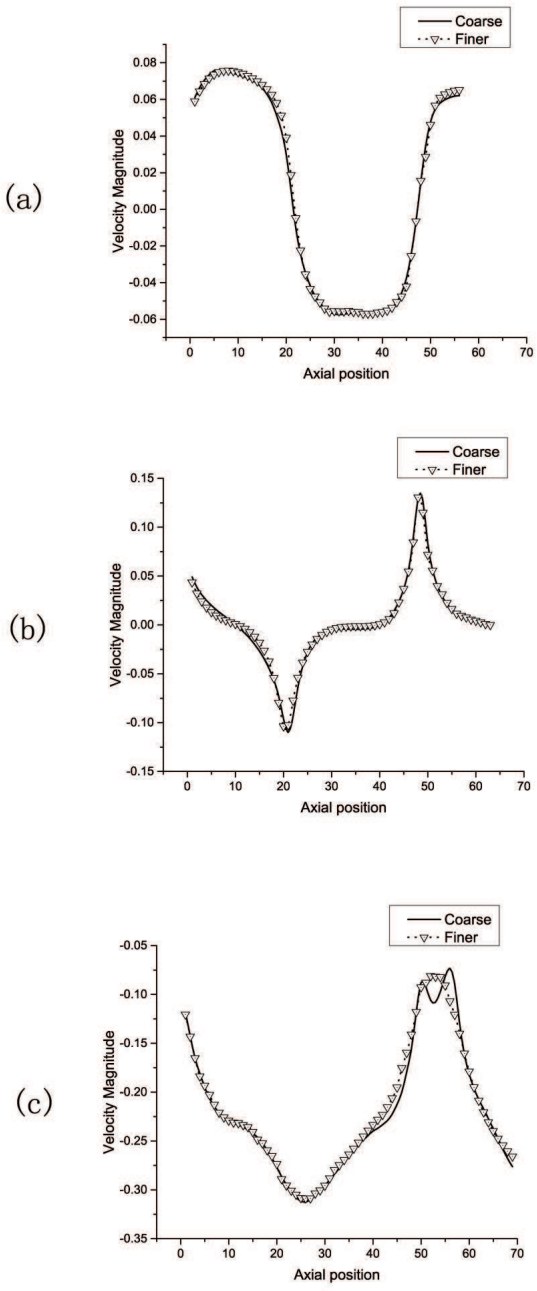

Figure 4.3 Grid resolution comparison of 3D: (a) Axial Velocity (mm/s), (b) Radial Velocity (mm/s), (c) Azimuthal Velocity (mm/s)

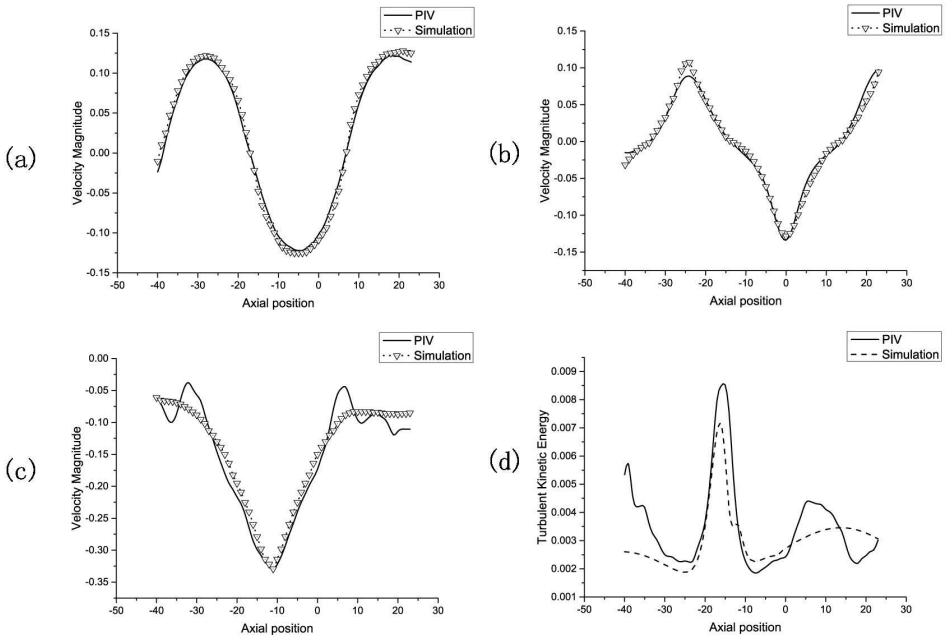

Figure 4.4 2D Velocity Profile and TKE Comparison at $R = 60$: (a) Axial Velocity (mm/s), (b) Radial Velocity (mm/s), (c) Azimuthal Velocity (mm/s), (d) Normalized TKE

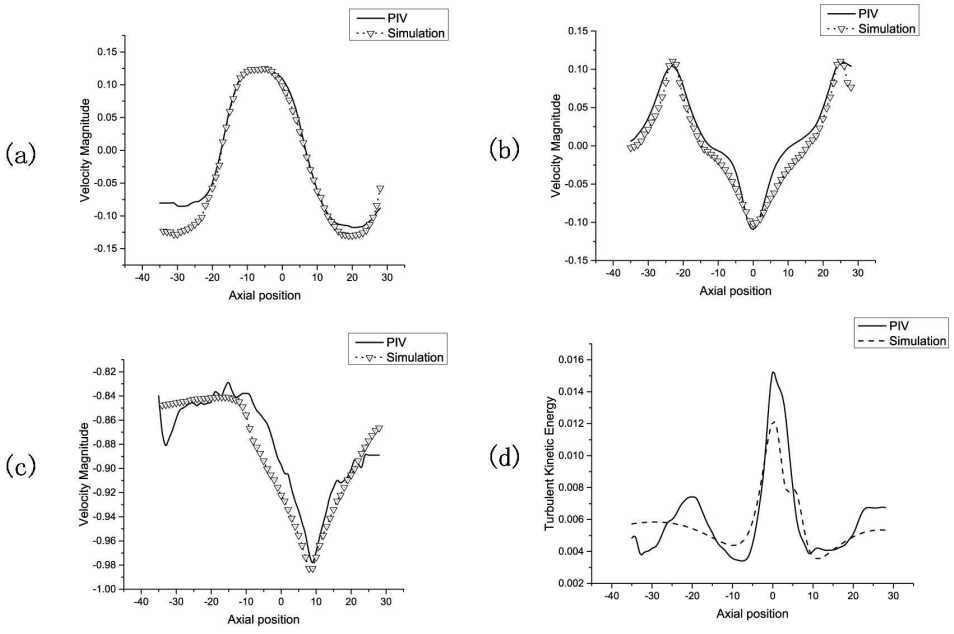

Figure 4.5 2D Velocity Profile and TKE Comparison at $R = 80$: (a) Axial Velocity (mm/s), (b) Radial Velocity (mm/s), (c) Azimuthal Velocity (mm/s), (d) Normalized TKE

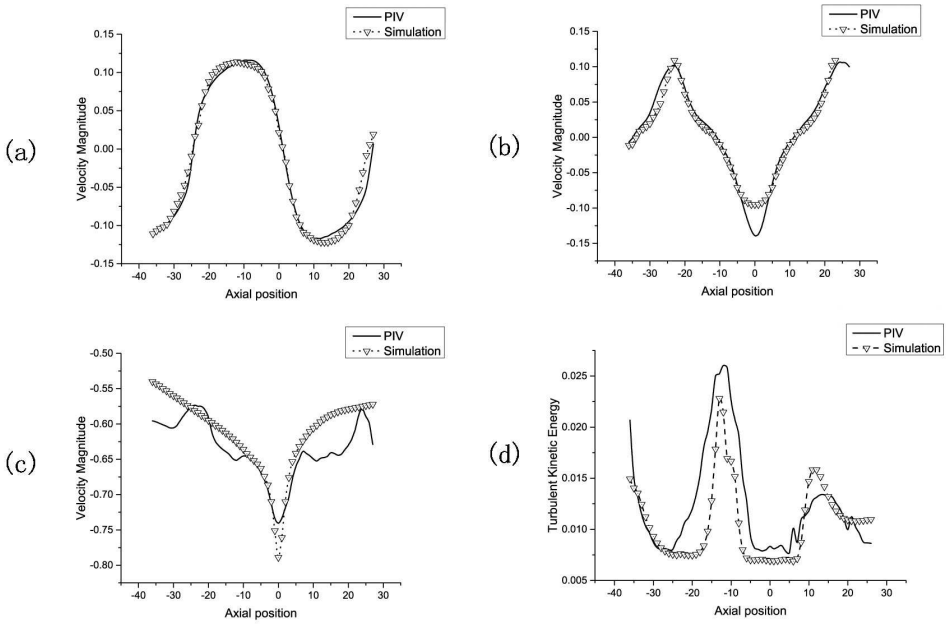

Figure 4.6 2D Velocity Profile and TKE Comparison at $R = 130$: (a) Axial Velocity (mm/s), (b) Radial Velocity (mm/s), (c) Azimuthal Velocity (mm/s), (d) Normalized TKE

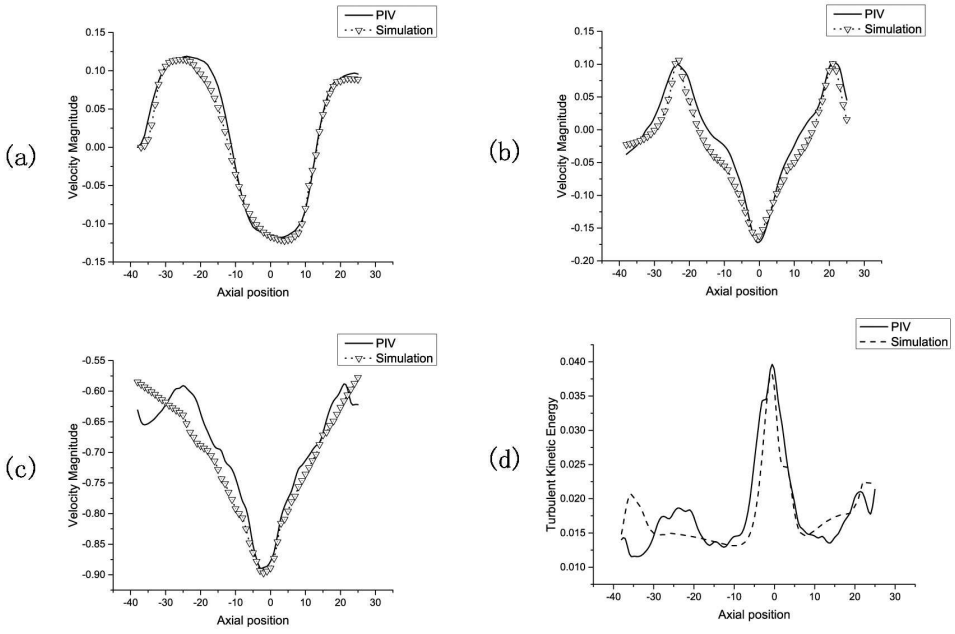

Figure 4.7 2D Velocity Profile and TKE Comparison at $R = 160$: (a) Axial Velocity (mm/s), (b) Radial Velocity (mm/s), (c) Azimuthal Velocity (mm/s), (d) Normalized TKE

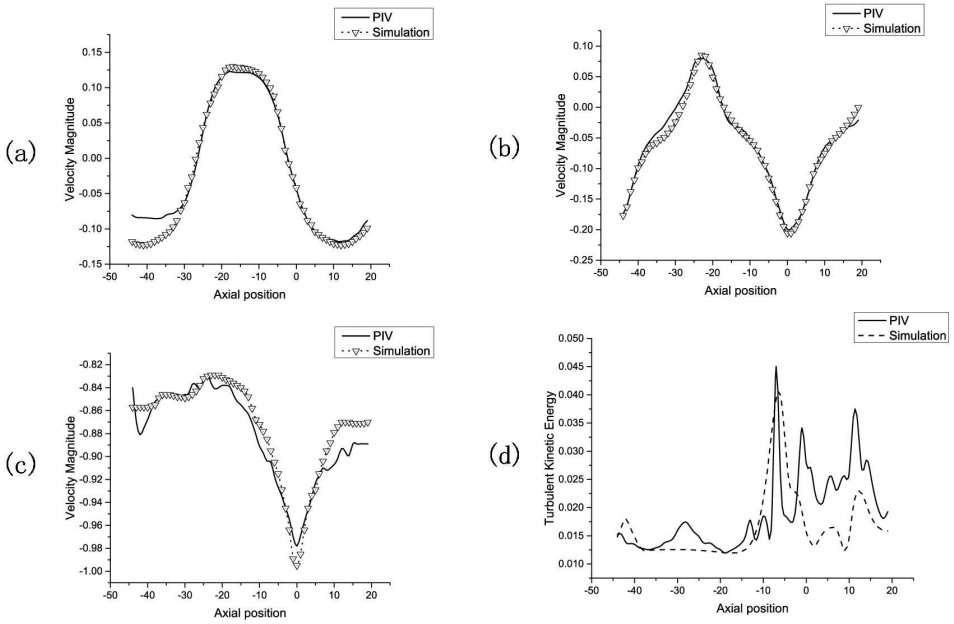

Figure 4.8 2D Velocity Profile and TKE Comparison at $R = 190$: (a) Axial Velocity (mm/s), (b) Radial Velocity (mm/s), (c) Azimuthal Velocity (mm/s), (d) Normalized TKE

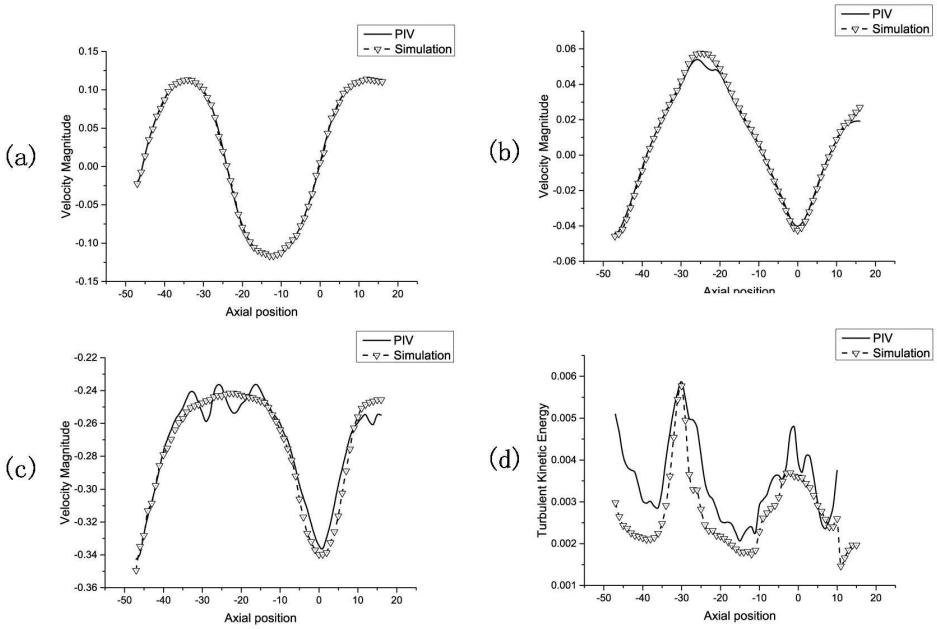

Figure 4.9 2D Velocity Profile and TKE Comparison near wall (1/8 gap distance from cylinder wall) at $R = 60$: (a) Axial Velocity (mm/s), (b) Radial Velocity (mm/s), (c) Azimuthal Velocity (mm/s), (d) Normalized TKE

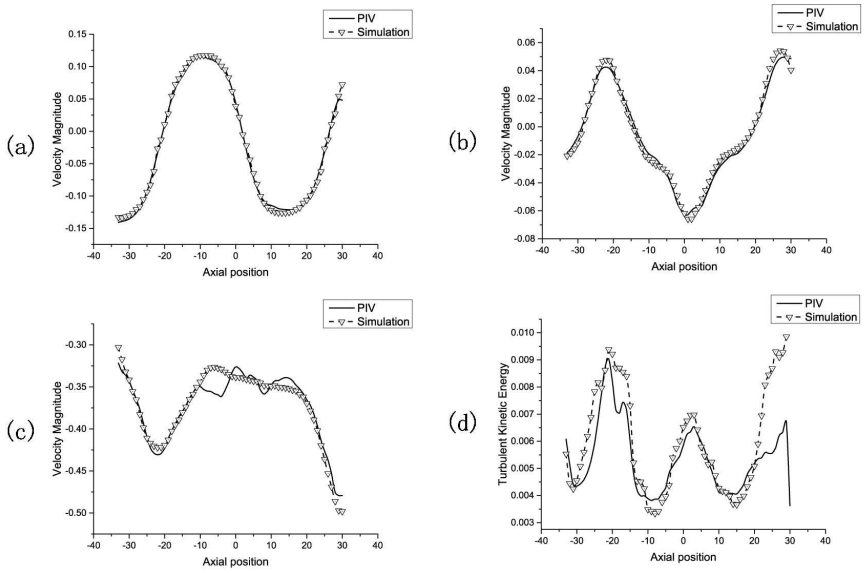

Figure 4.10 2D Velocity Profile and TKE Comparison near wall (1/8 gap distance from cylinder wall) at $R = 80$: (a) Axial Velocity (mm/s), (b) Radial Velocity (mm/s), (c) Azimuthal Velocity (mm/s), (d) Normalized TKE

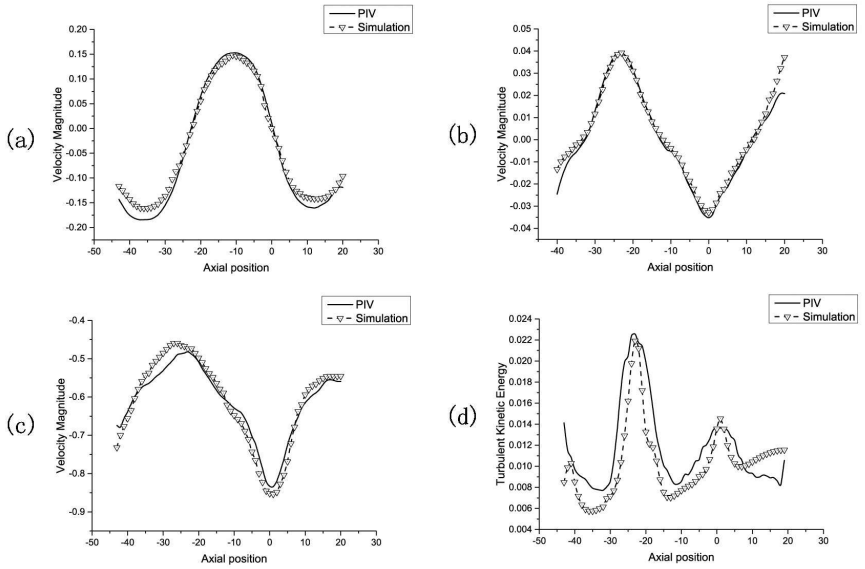

Figure 4.11 2D Velocity Profile and TKE Comparison near wall (1/8 gap distance from cylinder wall) at $R = 130$: (a) Axial Velocity (mm/s), (b) Radial Velocity (mm/s), (c) Azimuthal Velocity (mm/s), (d) Normalized TKE

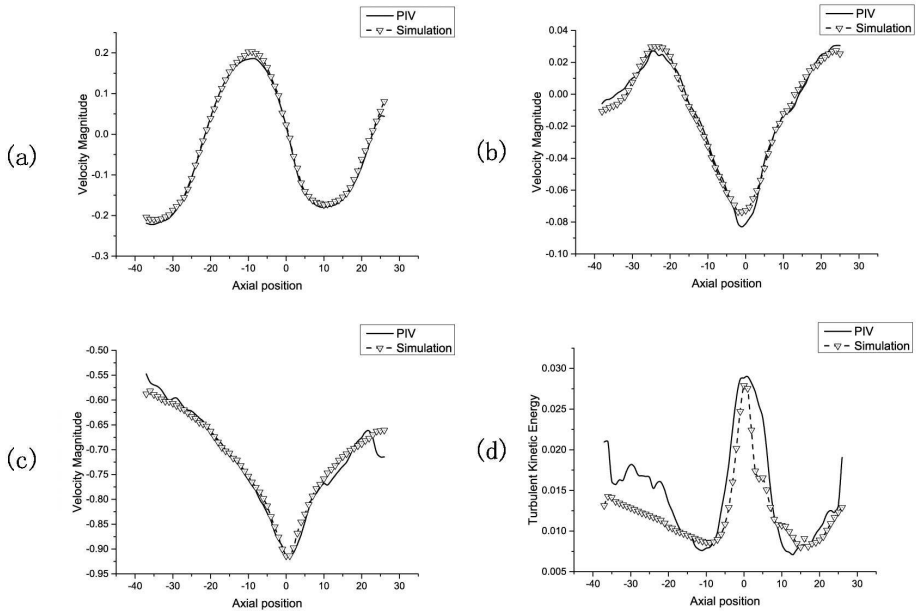

Figure 4.12 2D Velocity Profile and TKE Comparison near wall (1/8 gap distance from cylinder wall) at $R = 160$: (a) Axial Velocity (mm/s), (b) Radial Velocity (mm/s), (c) Azimuthal Velocity (mm/s), (d) Normalized TKE

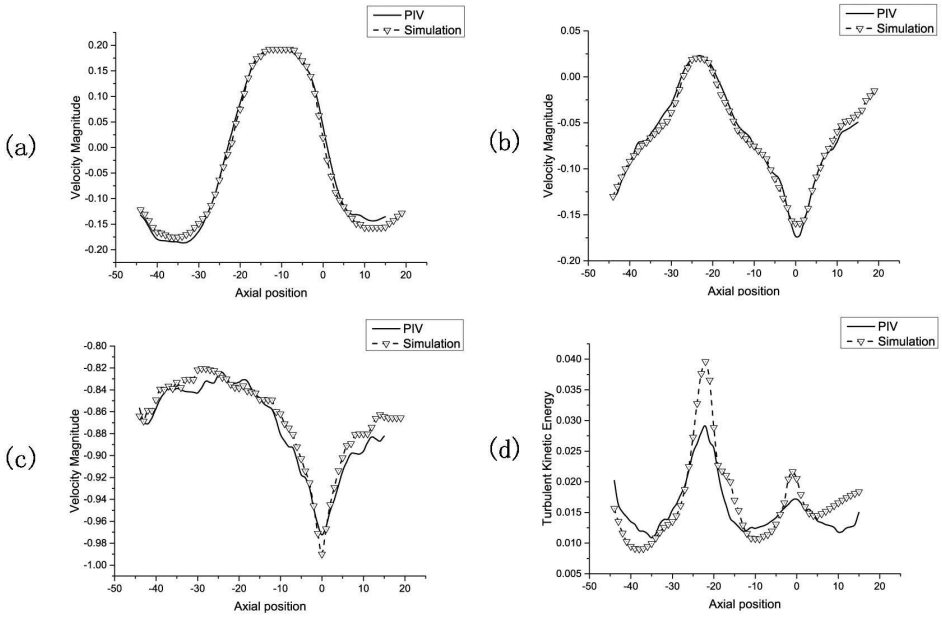

Figure 4.13 2D Velocity Profile and TKE Comparison near wall (1/8 gap distance from cylinder wall) at $R = 190$: (a) Axial Velocity (mm/s), (b) Radial Velocity (mm/s), (c) Azimuthal Velocity (mm/s), (d) Normalized TKE

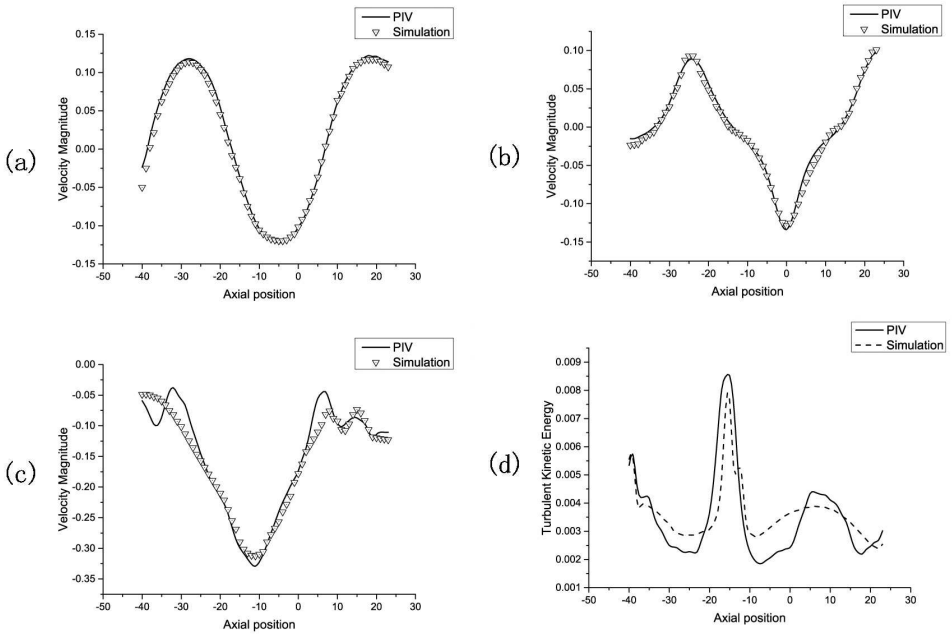

Figure 4.14 3D Velocity Profile and TKE Comparison: (a) Axial Velocity (mm/s), (b) Radial Velocity (mm/s), (c) Azimuthal Velocity (mm/s), (d) Normalized TKE

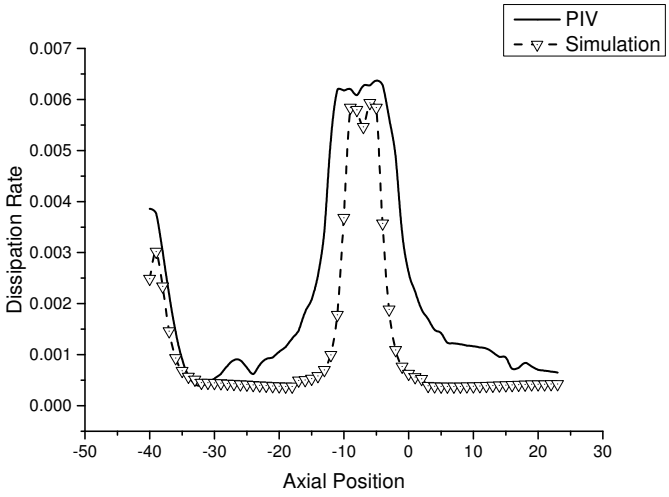

Figure 4.15 Normalized Turbulence Dissipation Rate Comparison between PIV and Simulation at R=60

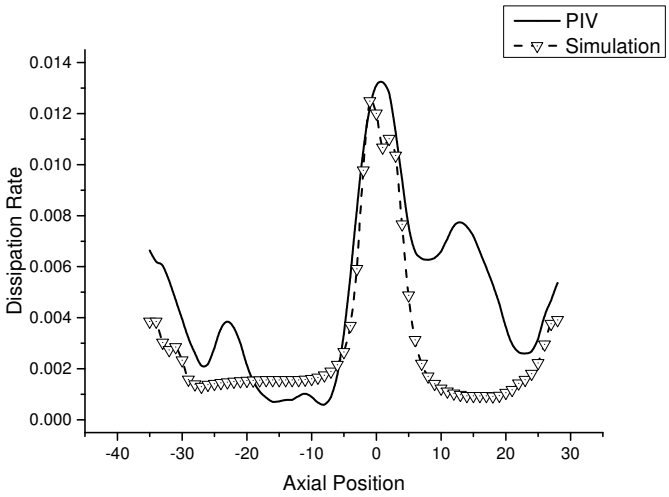

Figure 4.16 Normalized Turbulence Dissipation Rate Comparison between PIV and Simulation at R=80

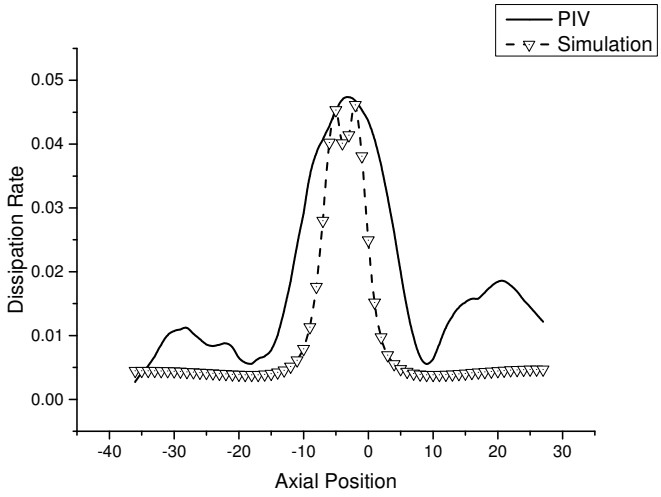

Figure 4.17 Normalized Turbulence Dissipation Rate Comparison between PIV and Simulation at R=130

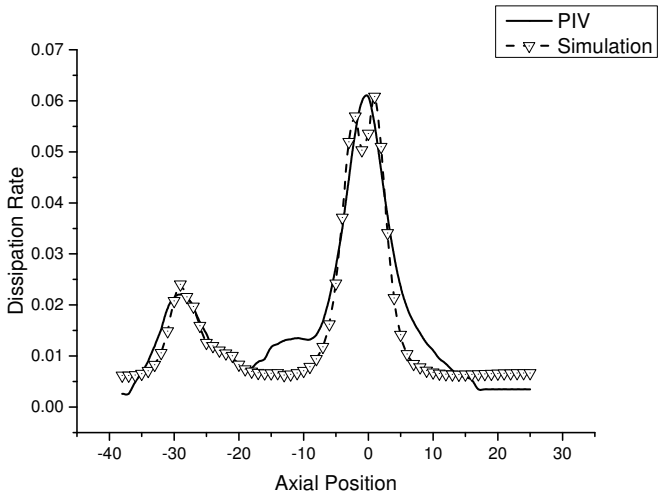

Figure 4.18 Normalized Turbulence Dissipation Rate Comparison between PIV and Simulation at R=160

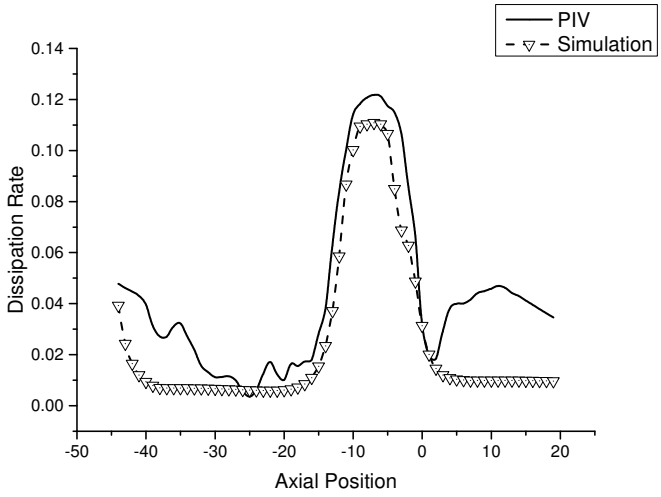

Figure 4.19 Normalized Turbulence Dissipation Rate Comparison between PIV and Simulation at R=190

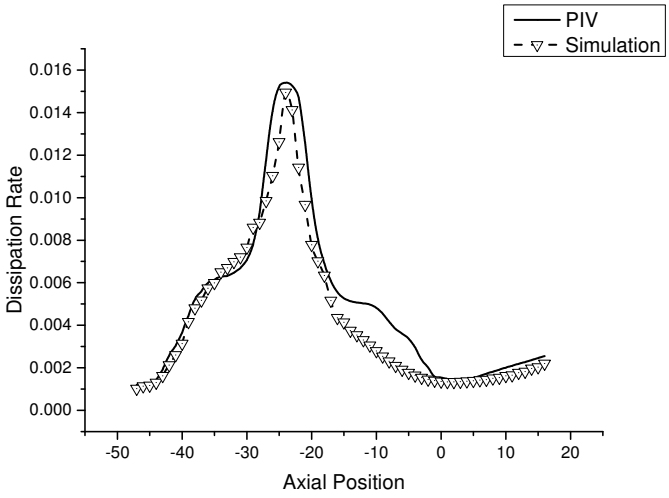

Figure 4.20 Normalized Turbulence Dissipation Rate Comparison near wall (1/8 gap distance from cylinder wall) between PIV and Simulation at R=60

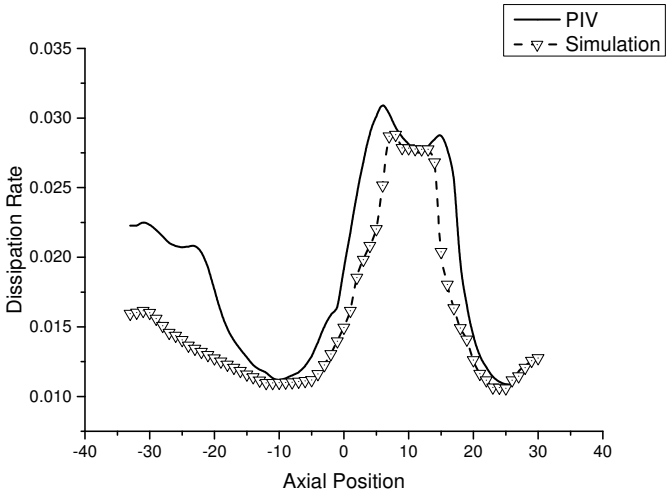

Figure 4.21 Normalized Turbulence Dissipation Rate Comparison near wall (1/8 gap distance from cylinder wall) between PIV and Simulation at R=80

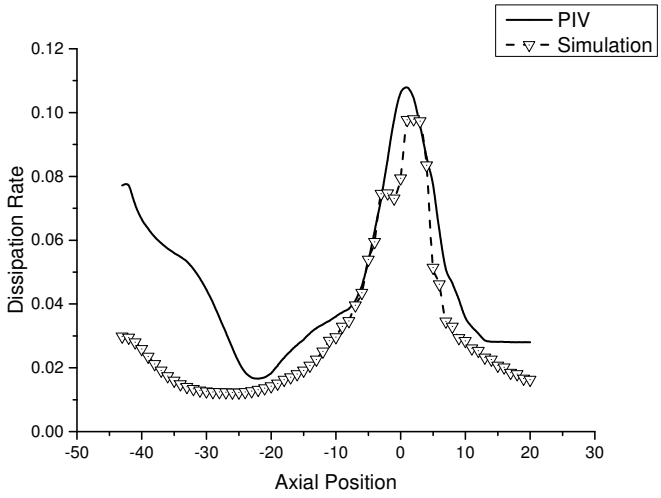

Figure 4.22 Normalized Turbulence Dissipation Rate Comparison near wall (1/8 gap distance from cylinder wall) between PIV and Simulation at R=130

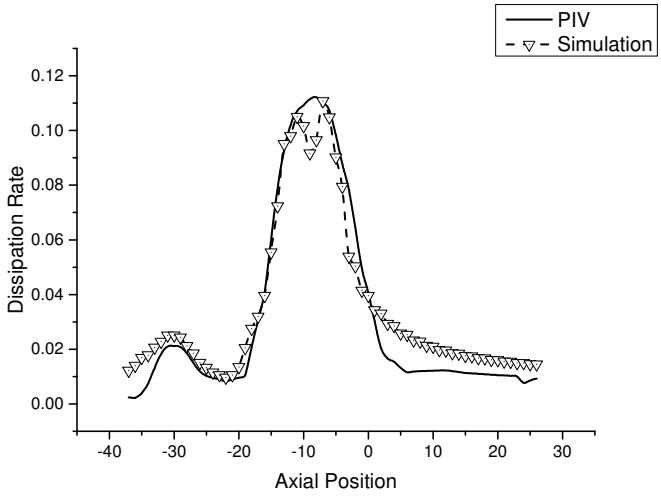

Figure 4.23 Normalized Turbulence Dissipation Rate Comparison near wall (1/8 gap distance from cylinder wall) between PIV and Simulation at R=160

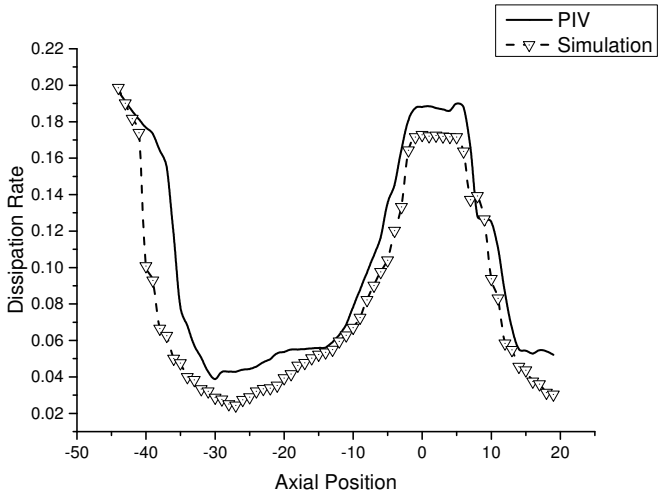

Figure 4.24 Normalized Turbulence Dissipation Rate Comparison near wall (1/8 gap distance from cylinder wall) between PIV and Simulation at R=190

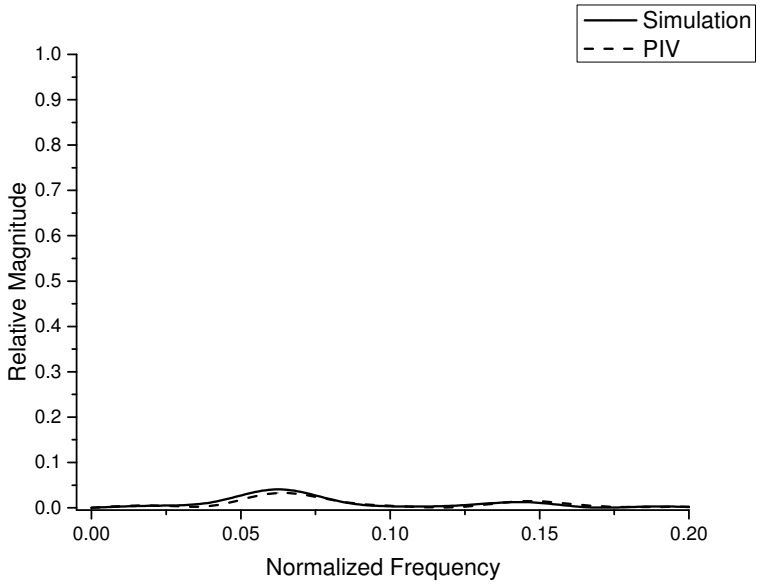

Figure 4.25 2D RANS with $k-\omega$ Power Spectral Density for R=17

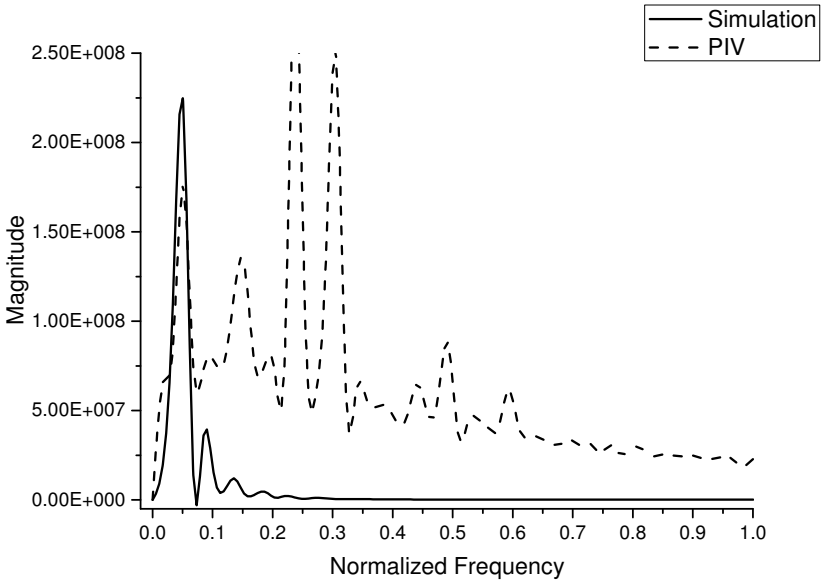

Figure 4.26 2D RANS with $k-\omega$ Power Spectral Density for R=50

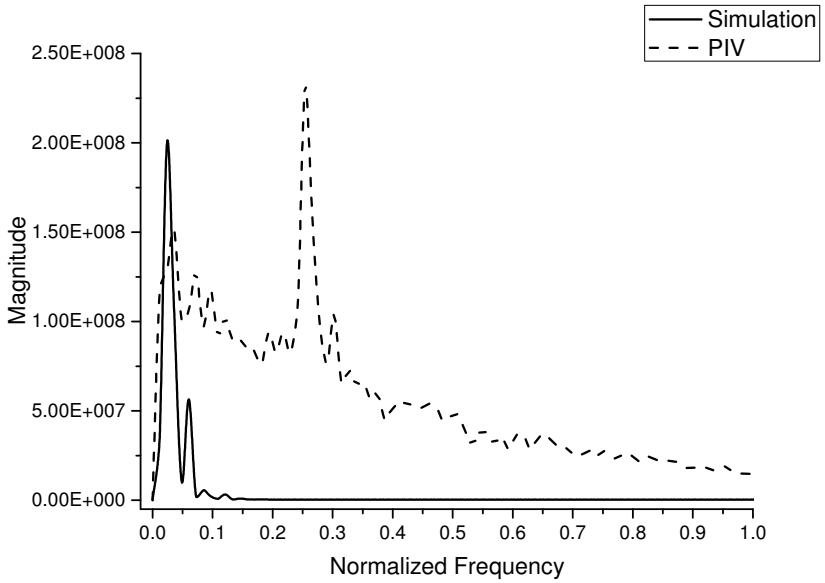

Figure 4.27 2D RANS with $k-\omega$ Power Spectral Density for R=60

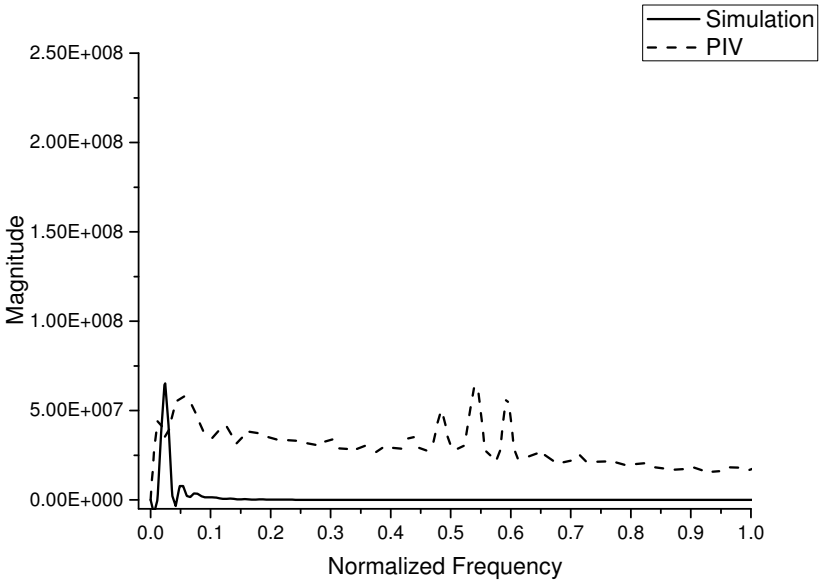

Figure 4.28 2D RANS with $k-\omega$ Power Spectral Density for R=70

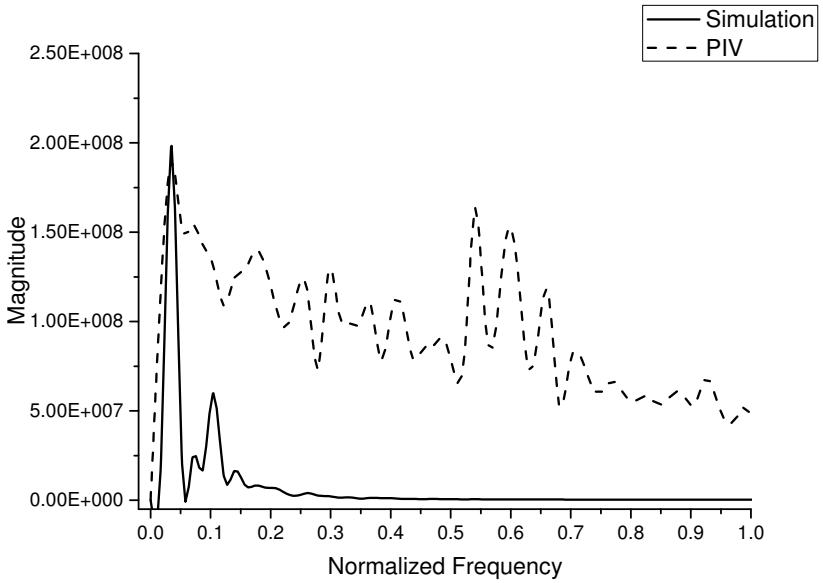

Figure 4.29 2D RANS with $k-\omega$ Power Spectral Density for R=80

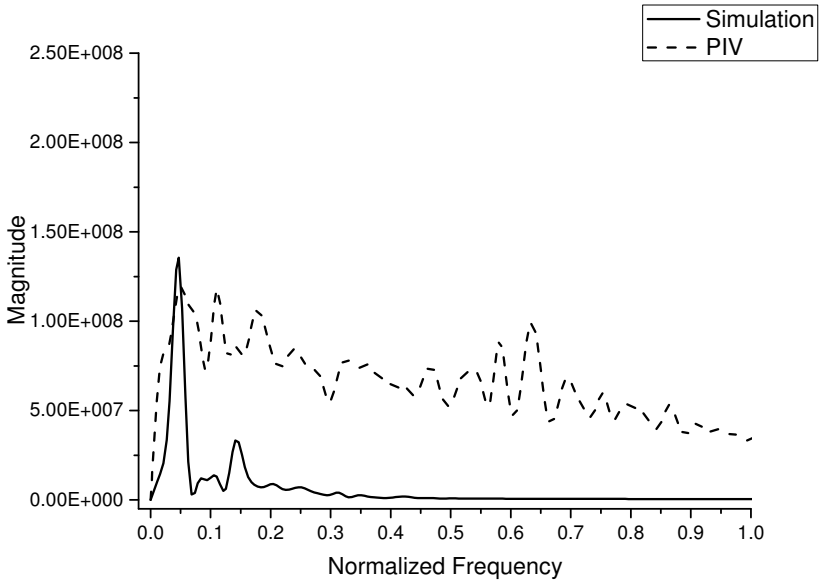

Figure 4.30 2D RANS with $k-\omega$ Power Spectral Density for R=130

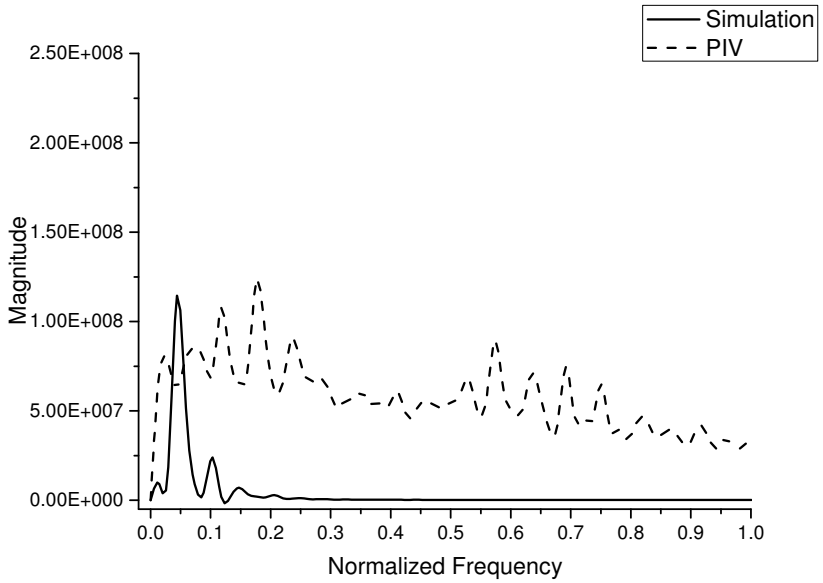

Figure 4.31 2D RANS with $k-\omega$ Power Spectral Density for R=145

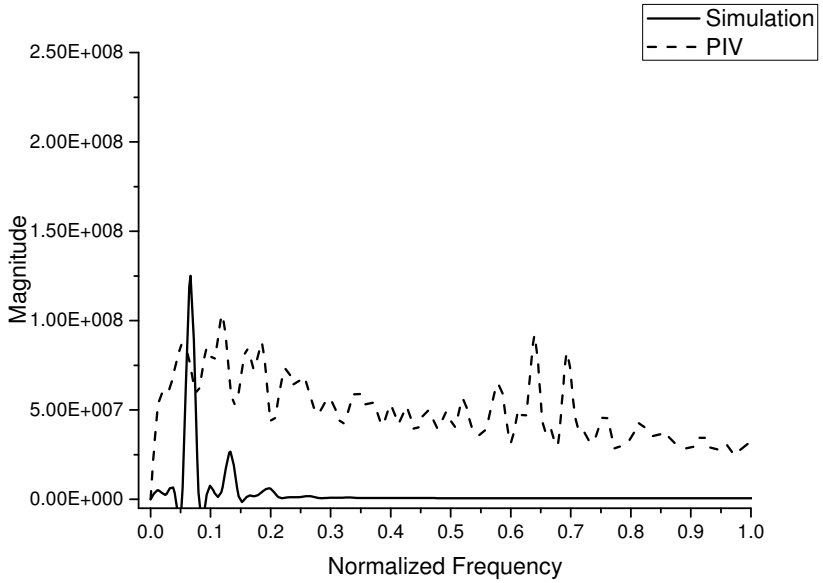

Figure 4.32 2D RANS with $k-\omega$ Power Spectral Density for R=160

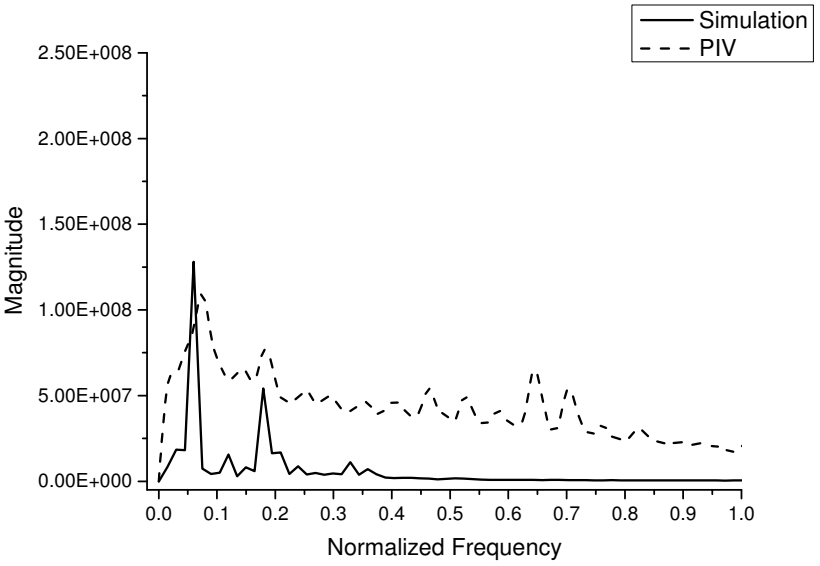

Figure 4.33 2D RANS with $k-\omega$ Power Spectral Density for R=190

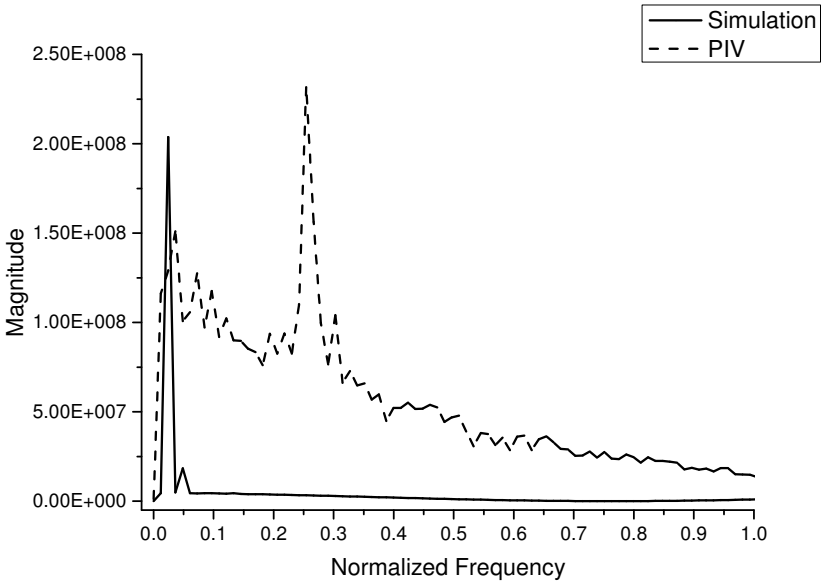

Figure 4.34 3D RANS with $k-\omega$ Power Spectral Density for R=60

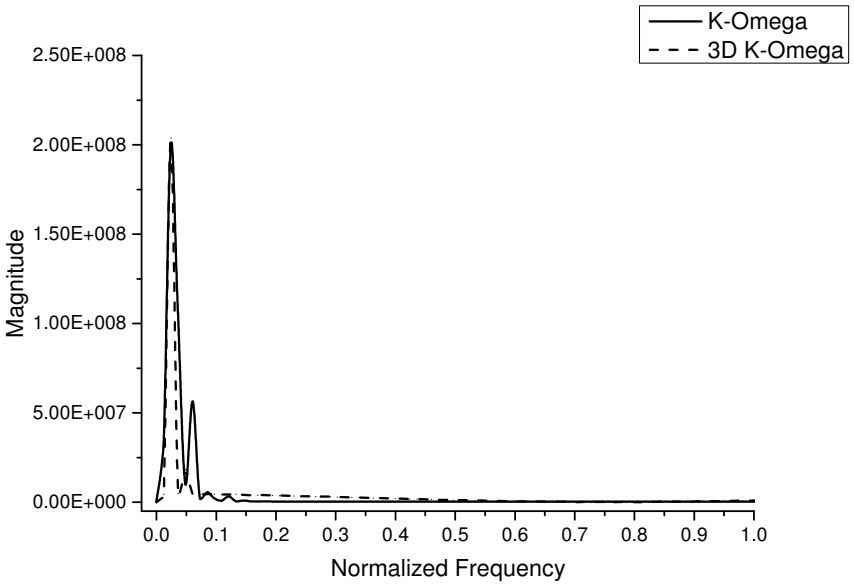

Figure 4.35 2D vs 3D RANS with $k-\omega$ Power Spectral Density for R=60

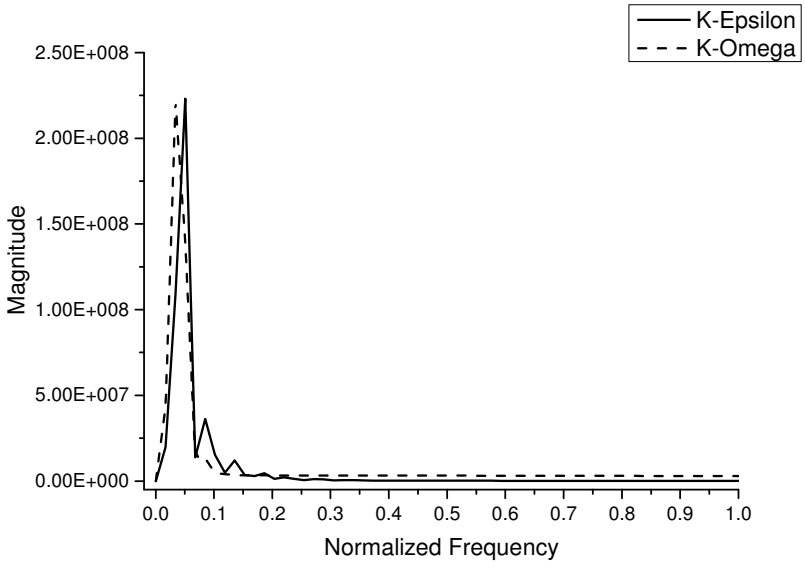

Figure 4.36 Power Spectral Density comparison between $k-\omega$ and $k-\varepsilon$ model for R=50

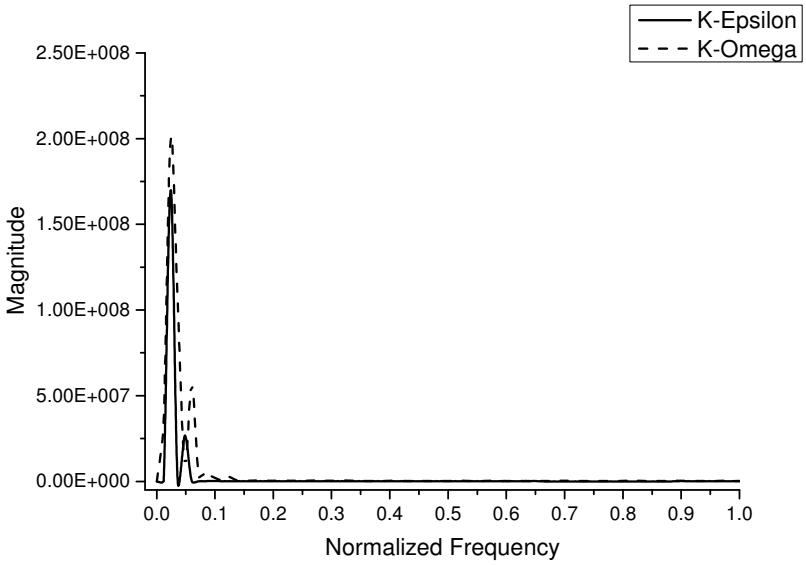

Figure 4.37 Power Spectral Density comparison between $k-\omega$ and $k-\varepsilon$ model for R=60

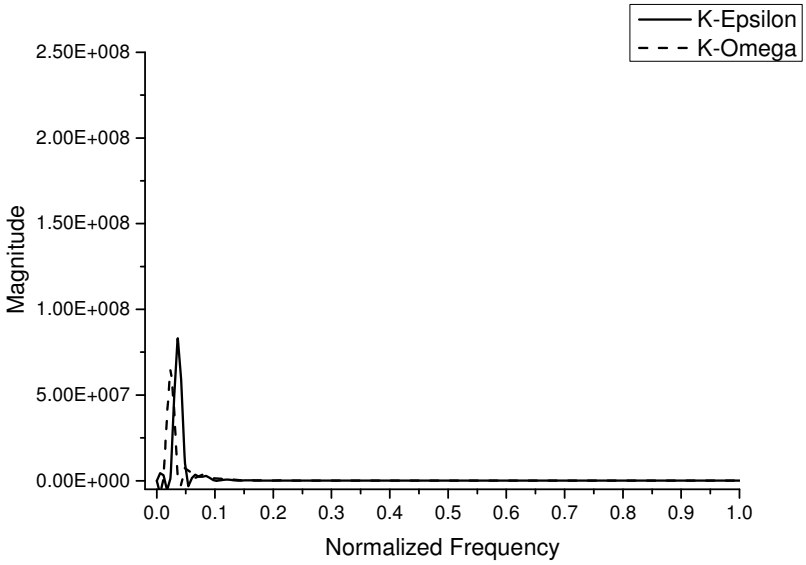

Figure 4.38 Power Spectral Density comparison between $k-\omega$ and $k-\varepsilon$ model for R=70

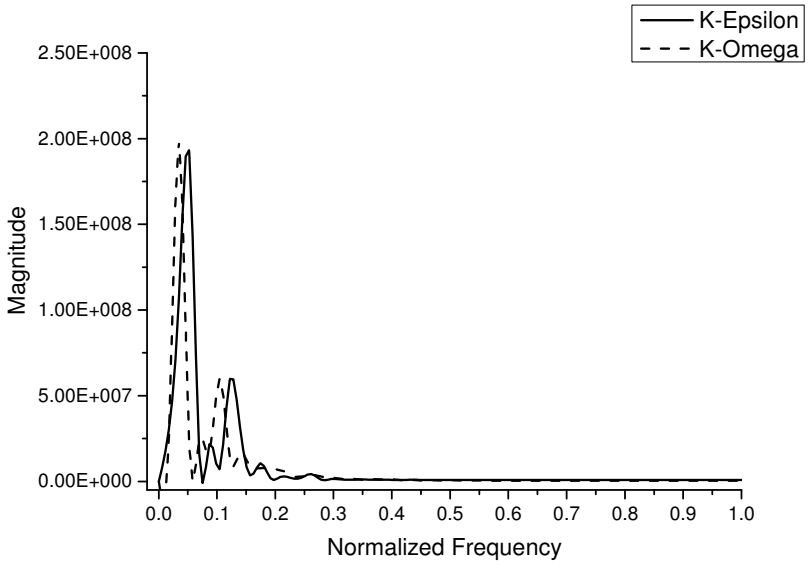

Figure 4.39 Power Spectral Density comparison between $k-\omega$ and $k-\varepsilon$ model for R=80

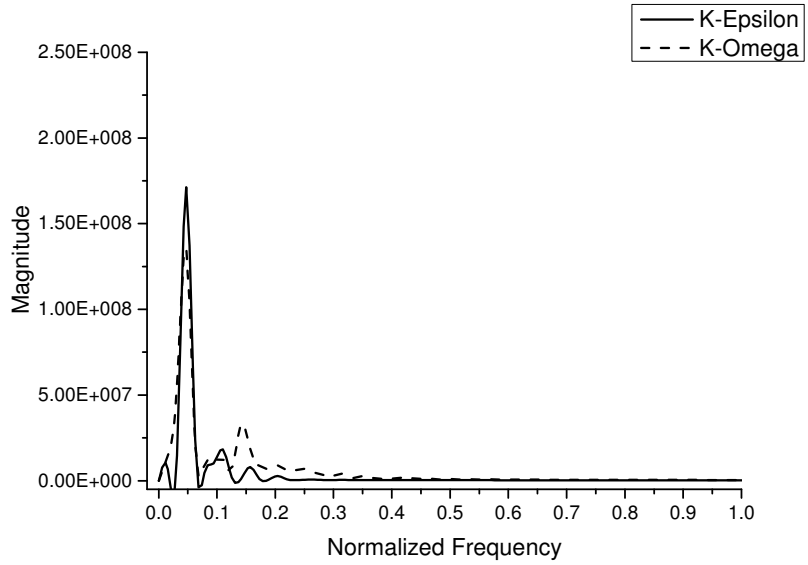

Figure 4.40 Power Spectral Density comparison between $k-\omega$ and $k-\varepsilon$ model for R=130

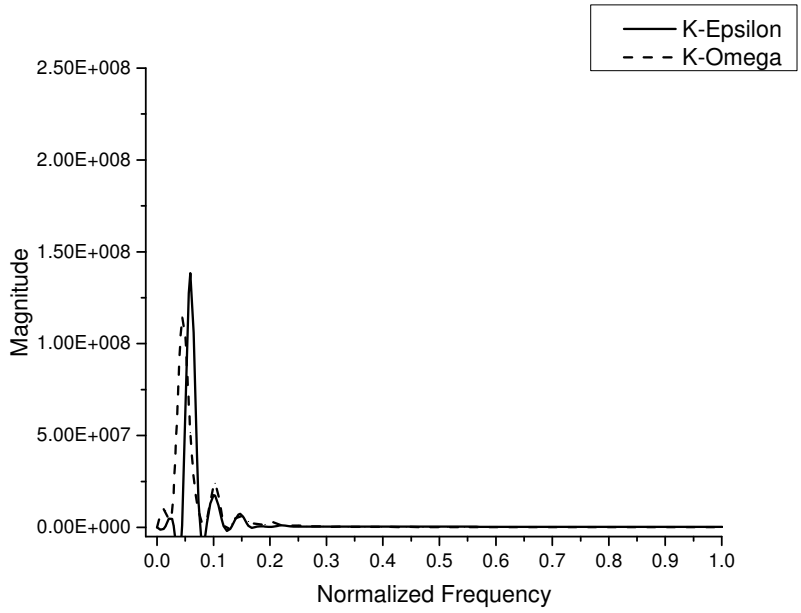

Figure 4.41 Power Spectral Density comparison between $k-\omega$ and $k-\varepsilon$ model for R=145

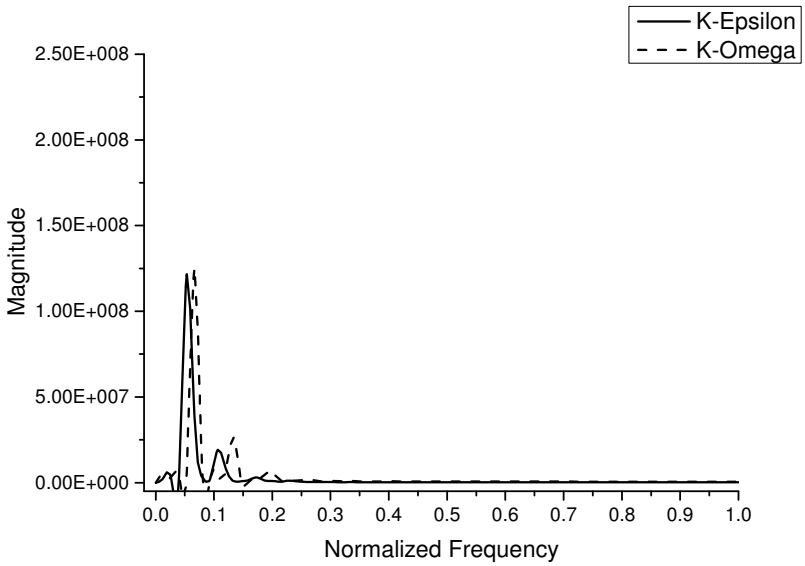

Figure 4.42 Power Spectral Density comparison between $k-\omega$ and $k-\varepsilon$ model for R=160

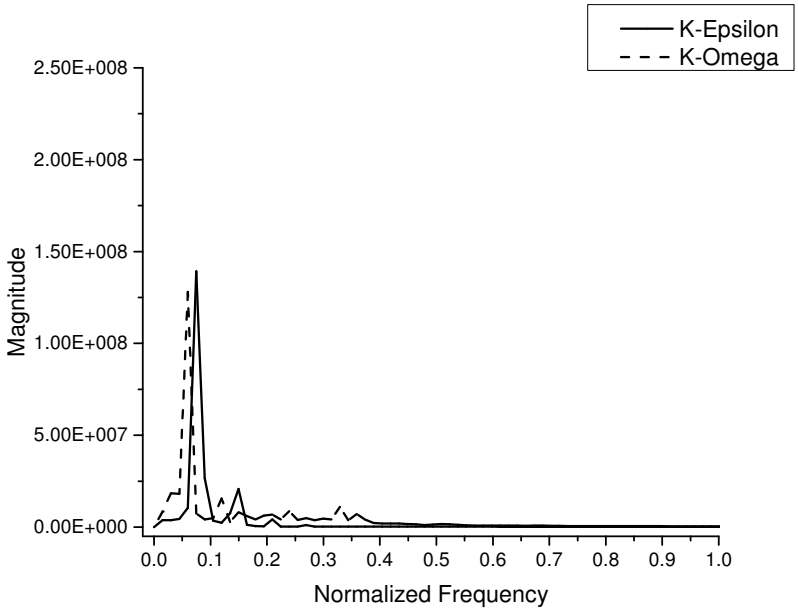

Figure 4.43 Power Spectral Density comparison between $k-\omega$ and $k-\varepsilon$ model for R=190

CHAPTER 5. CONCLUSION AND FUTURE DIRECTIONS

In this chapter, important findings and the conclusions from this thesis work are drawn from the data and are summarized. Future directions for experimental and computational investigation of the Taylor-Couette flow are also identifieds.

Summary and Discussion

Analysis of Taylor-Couette flow with the power spectral density method

Experiments using stereoscopic PIV were designed to investigate Taylor-Couette flow. The results confirm that wavy vortex flow first appears once the Reynolds number increases above the critical value, followed by modulated wavy vortex flow as Reynolds number is increased. As the rotating velocity of inner cylinder accelerates causing the Reynolds number of the flow to increase, the Taylor-Couette flow transitions to turbulent vortex flow. Travelling azimuthal waves cause the wavy motion in the Taylor-Couette flow. Velocity field results from the PIV experiments indicate that the azimuthal wavy motion in the wavy vortex flow becomes weaker as the Reynolds number increases before disappearing completely at R= 17. The travelling azimuthal wave then reappear in the flow if the rotating velocity further increases beyond R=17. The reappearance of the azimuthal wave is not easy to identify in the instantaneous velocity fields obtained by PIV, so a power spectral density technique has been developed to assist in the analysis.

Power spectral density can be used as an analysis method for the azimuthal wave since it describes how the power of a signal or time series is distributed over frequencies.

PSD is calculated based on the velocity data for all three components captured by PIV. The analysis of the power spectrum results in the same findings for azimuthal waves in wavy vortex flow as was observed in the PIV velocity fields; the intensity of the traveling azimuthal waves gets weaker with increasing Reynolds number.

In the PSD plots, a single dominant peak corresponds to the azimuthal wave; the magnitude of the peak represents the intensity of the wave, and the normalized frequency of the peak is used to identify the wave. For the special case, $R = 17$, where no movement of the vortex boundaries and the vortex center were observed in the velocity fields, the single dominant peak in the PSD disappears, meaning no azimuthal waves exist in the flow, a finding that corresponds to the observation in the PIV. At higher Reynolds number, the single peak reappears in the PSD indicating the reappearance of the azimuthal waves in the Taylor-Couette flow. Unlike the PIV results, in which it is difficult to identify the reappeared wavy motion and its intensity, the power spectrum can easily identify the reappeared azimuthal wave.

Based on the PSD analysis, the reappearance of the wavy motion differs from the original waviness. The peak in the PSD has a fixed normalized frequency location in the wavy vortex flow until disappearing, indicating the same traveling azimuthal wave phenomenon affects the flow. Also, in the modulated wavy vortex flow the original peak keeps diminishing while a new peak arises at another higher frequency. The new peak that is attributed to a modulated frequency of the fundamental azimuthal wave had the same trend as the original one, the magnitude of peak decreases with increasing Reynolds number. The azimuthal waves that reappear beyond R=17 appear at the normalized frequency corresponding to the earlier observed modulation.

Reynolds number $R = 24$ is another case where the single dominant peak disappears once again. This suggests that the reappeared traveling azimuthal waves vanishes as Reynolds number increases and the flow becomes turbulent. In the turbulent flow regime, the power spectral density of the PIV data has multiple peaks and a broadband

background spectrum. The turbulent velocity data captured by PIV show many turbulent structures in the flow which makes the power spectral density method less useful to identify highly azimuthal waves in turbulent Taylor-Couette flow.

Reynolds-averaged Navier-Stokes simulation of Taylor-Couette flow

The Reynolds-averaged Navier-Stokes (RANS) technique was used to simulate turbulent Taylor-Couette flow using two of the most commonly used turbulence models, the $k-\varepsilon$ model and the $k-\omega$ model.

$k-\varepsilon$ model used in turbulent Taylor-Couette flow simulation

The $k-\varepsilon$ model is the most common turbulent model used in RANS simulations. 2D and 3D unsteady RANS simulations using the $k-\varepsilon$ model were performed for the Taylor-Couette flow. Particle image velocimetry experiments were performed in an experimental apparatus of the same geometry as the simulations in order to provide detailed velocity statistics that could be used to validate the accuracy of the RANS models used in this investigation. The effects of grid resolution on the velocity statistics using second order central schemes for interpolation and second order Gaussian integration, and explicit non-orthogonal correction as the gradient scheme were studied in order to determine the effect of these parameters on the accuracy of simulation results. Two final grid resolutions, a coarse grid and a finer grid, were tested for both the 2D and 3D simulations. Since the improvement using the higher resolution compared to the resolution chosen for the presented simulation is rather small, the grid was considered converged. 2D and 3D RANS simulations with the two equations model, the $k\varepsilon$ model, and wall-functions, using the standard values for the constants at different Reynolds numbers was found to compare very well with the velocity statistics for PIV data, including axial, radial, and azimuthal velocities, turbulent kinetic energy, and turbulent dissipation. The 2D simulation was found to be highly accurate based on the comparison.

A comparison of power spectral density over a range of Reynolds numbers shows excellent agreement between RANS and PIV results for both 2D and 3D simulation. Note that the PSD for the simulations show only unsteady fluctuation, because the turbulence is modeled and not resolved in the simulations. Power spectral density of the RANS simulations shows the same trends as the PIV data in that with the changing of rotation velocity, the magnitude of the peak changes with increasing the Reynolds number. The 3D results of the power spectral density are also compared with the 2D results to investigate the accuracy between different simulation methods. In the comparison, very little improvement in using the 3D simulation could be found which indicated 2D power spectrum results are sufficient for the investigation. The excellent agreement observed between both the velocity statistics and the power spectral density of the simulation and PIV data demonstrates that RANS with the $k-\varepsilon$ model is able to accurately capture the important characteristics of the turbulent Taylor-Couette flow. Also, the outstanding comparison between the results of 2D and 3D methods indicates that 2D RANS with the $k-\varepsilon$ model is an accurate and economical method for simulating turbulent Taylor-Couette flow, since the 3D simulation requires much more time and computational sources while provides the same outcomes.

$k-\omega$ model used in turbulent Taylor-Couette flow simulation

The $k-\omega$ model is another common turbulent model used in RANS simulations. 2D and 3D unsteady RANS simulations using the $k-\omega$ model were performed for the turbulent Taylor-Couette flow. The simulation results were compared with particle image velocimetry data which are captured in an experimental apparatus of the same geometry. The $k-\omega$ model was validated to be accurate in simulating velocity statistics and power spectral density for both 2D and 3D simulations. In order to test the $k-\omega$ model, all same procedures are repeated for the $k-\omega$ model as were done for the $k-\varepsilon$ model. The effect of different grid resolutions on the velocity statistics using second order

central schemes for interpolation and second order Gaussian integration, and explicit non-orthogonal correction as the gradient scheme were studied in order to determine the effect of these parameters on the accuracy of the simulations. A coarse grid and a finer grid are investigated for both 2D and 3D methods in order to find the appropriate resolution for study. The higher grid resolution, the finer grid, showed relatively small improvement compared to the resolution of the coarse grid, which was chosen for the rest of study. Using the coarse grid, velocity profiles for the axial, radial, and azimuthal components and turbulent kinetic energy turbulent dissipation using the $k-\omega$ model were compared with PIV data. The comparison showed both the 2D and 3D RANS simulations using the $k-\omega$ model were precise in simulating the turbulent Taylor-Couette flow. However, the 2D simulation can save time and computer resources compared to the 3D simulation, so it is a better option.

The same study of the power spectral density was presented for $k-\omega$ model. A comparison of the power spectral density over a range of Reynolds numbers shows excellent agreement between the RANS and PIV results for both the 2D and 3D simulation. The 2D PSD results have the same trend as those for the $k-\varepsilon$ model and the PIV results with the change of rotation velocity. 3D results are compared with 2D results and PIV data and show very little improvement over the 2D simulation, which suggests that the 2D simulation was the better option since it requires much less time and resources to get the same results. Good comparison of both velocity statistics and power spectral density between simulation and PIV data indicated that RANS simulations using the $k\omega$ model were able to accurately capture the important characteristics of the turbulent Taylor-Couette flow.

Since the $k-\varepsilon$ model and the $k-\omega$ model are the most common turbulent models used with the RANS method, it is important to compare the two models. A comparison between the $k-\omega$ model and the $k-\varepsilon$ model was made to find the difference between the two models and the better turbulent model choice in the RANS simulations. Power

spectral density results of the $k-\omega$ model and the $k-\varepsilon$ model are compared with each other. The shapes of the PSD at different Reynolds numbers are almost identical to each other except some variations in the magnitude for some Reynolds number cases. The main differences between two models are variations in the normalized frequency which corresponds to the single dominant peak. Although the variations in the frequency are relatively small, the $k-\omega$ model peaks in the PSD matched with PIV data slightly better than the $k-\varepsilon$ model, suggesting that the $k-\omega$ model would be a better option in simulations.

Future Directions

First, to investigate strongly turbulent Taylor-Couette flow, PIV data for higher Reynolds number cases are needed for both experimental and computational study. As can be seen in the turbulent Taylor vortex flow, small vortex structures appear near inner and outer cylinder walls. More higher Reynolds number cases would be helpful to analyze and understand the behavior and characteristic of these small vortex structures. Also, the simulation velocity profiles matches better with PIV data for the high Reynolds numbers cases. This is true for the $k-\omega$ model. Moreover, a larger range of Reynolds numbers with PIV data is useful in the future to study different simulation methods and models.

The RANS method with the $k-\varepsilon$ model and the $k-\omega$ model were used in the present thesis for computational study. More turbulence models can be investigated in the numerical investigation of Taylor-Couette flow. The two models used in this thesis are the two most common two-equation models of linear eddy viscosity models which are derived from Boussinesq approximation. Some other linear eddy viscosity models, such as one-equation model and the $k-\omega$ SST model, are important and useful in the study of simulation of Taylor-Couette flow. Also, the Reynolds stress model (RSM) is another

important turbulence model for RANS that closes the Reynolds-averaged Navier-Stokes equations by solving transport equations for the Reynolds stresses, together with an equation for the dissipation rate. It would beneficial for future studies to investigate the using the RSM in Taylor-Couette flow.

Third, the RANS methodology used in the thesis is the the oldest approach to turbulence modeling, but not most accurate method. RANS is inexpensive and easy. But it also has some disadvantages compared to other CFD methods. Large eddy simulation (LES) in which the smallest scales of the flow are removed through a filtering operation, and their effect modeled using subgrid scale models, and Direct numerical simulation (DNS) that resolves the entire range of turbulent length scales are two other simulation methods widely used in CFD. These two simulation methods can provide more precise results than RANS, although they are much more expensive. DNS is extremely expensive, while LES requires greater computational resources than RANS methods, but is far cheaper than DNS. In the present thesis, the RANS method has been proved to be accurate in the simulation of Taylor-Couette flow. However, some small variations between simulation and experiment in velocity statistics and power spectrum can still be observed. Thus, a thorough computational study of Taylor-Couette flow should investigated the different CFD turbulence models. In the future, simulations using LES and DNS methods are needed. Based on the comparison between PIV data and different simulation outputs, conclusions can be drawn as to if the RANS method is the most appropriate method for simulating Taylor-Couette flow with the consideration of time and resources cost.

Finally, in Taylor vortex flow the motion of individual particle needs to be investigated in detail. With the help of PIV experimental data, CFD simulations of Taylor-Couette flow could be used in the study of particle tracking for wavy vortex and fully turbulent flow. RANS, LES, and DNS methods can be used in the simulation of particle tracking in order to investigate the accuracy and influence of different turbulence models.

BIBLIOGRAPHY

Adachi, Y., Stuart, M. A. C., and Fokkink, R. (1994). Kinetics of turbulent coagulation studied by means of end-over-end rotation. *J. Colloid Interface Sci.*, *165*, 310–317.

Adler, P. M. (1981). Heterocoagulation in shear flow. *J. Colloid Interface Sci.*, *83*(1), 106–115.

Aider, A. A., Skali, S., and Brancher, J. P. (2005). Laminar-turbulent transition in Taylor-Dean flow. *J. of Physics: Conference Series*, *14*, 118–127.

Akonur, A. and Lueptow, R. M. (2003). Three-dimensional velocity field for wavy Taylor-Couette flow. *Phys. Fluids*, *15*, 947–960.

Al-Rashed, M. H. and Jones, A. G. (1999). CFD modelling of gas-liquid reactive precipitation. *Chem. Eng. Sci.*, *54*, 4779–4784.

Andereck, C. D., Liu, S. S., and Swinney, H. L. (1986). Flow regimes in a circular couette system with independently rotating cylinders. *J.of Fluid Mech.*, *164*, 155–183.

Aoun, M., Plasari, E., David, R., and Villermaux, J. (1996). Are barium sulphate kinetics sufficiently known for testing precipitation reactor models. *Chem. Eng. Sci.*, *51*(10), 2449–2458.

Aoun, M., Plasari, E., David, R., and Villermaux, J. (1999). A simultaneous determination of nucleation and growth rates from batch spontaneous precipitation. *Chem. Eng. Sci.*, *54*, 1164–1180.

Armentante, P. M. and Kirwan, D. J. (1989). Mass transfer to microparticles in agitated system. *Chem. Eng. Sci.*, *44*, 2781–2796.

Bagnold, R. (1954). Experiments on a gravity-free dispersion of large solid spheres in a Newtonian fluid under shear. *Proc. R. Soc. Lond. A*, *225*, 49–63.

Baldyga, J. and Orciuch, W. (2001). Barium sulphate precipitation in a pipe - an experimental study and CFD modeling. *Chem. Eng. Sci.*, *56*, 2435–2444.

Bandyopadhyaya, R., Kumar, R., and Gandhi, K. S. (2001). Modelling of CaCOg nanoparticle formation during overbasing of lubrication oil additives. *Langmuir*, *17*, 1015–1029.

Barenghi, C. F., Park, K. and Donnelly, R. J. (1980). Subharmonic destabilization of Taylor vortices near an oscillating cylinder. *Phys. Lett. A*, *72*, 152–154.

Barrett, J. C. and Webb, N. A. (1998). A comparision of some approximate methods for solving the aerosol general dynamic equation. *J. Aerosol Sci.*, , 31–39.

Batten, W. M. J., Bressloff, N. W., and Turnock, S. R. (2002). Numerical simulations of the evolution of Taylor cells from a growing boundary layer on the inner cylinder of a high radius ratio Taylor-Couette system. *hys. Rev. E*, *66*, 066302.

Berkooz, G., Holmes, P., and Lumley, J. L. (1993). The proper orthogonal decomposition in the analysis of turbulent flows. *Annual Review of Fluid Mech.*, *25*, 539–575.

Berland, T., Jssang, T., and Feder, J. (1986) An experimental study of the connection between the hydrodynamic and phase-transition descriptions of the CouetteTaylor instability. *Phys. Scripta*, *34*, 427–431.

Bi, W., Sugii, Y., Okamoto, K., and Madarame, H. (2003). Time resolved proper orthogonal decomposition of the near field flow of a round jet measured by dynamic particle image velocimetry. *Meas. Sci. Technol.*, *14*, L1–L5.

Bilson, M. and Bremhorst, K. (2007). Direct numerical simulation of turbulent Taylor-Couette flow. *J. Fluid Mech.*, *579*, 227–270.

Brandstater, A., Swift, J., Swinney, H. L., Wolf, A., Farmer, J. D., Jen, E., and Crutchfield, P. J. (1983). Low-dimensional chaos in a hydrodynamic system. *Phys. Rev. Lett.*, *51*, 1442–5.

Brandstater, A., Swift, J., Swinney, H. L., and Wolf, A. (1984). A strange attractor in a Couette-Taylor experiment. *Turbulence and Chaotic Phenomena in Fluids*, 179–84.

Brandstater, A. and Swinney, H. L. (1987). Strange attractors in weakly turbulent Couette-Taylor flow. *Phys. Rev. A*, *35*(5), 2207–2220.

Burkhalter, J.E., and Koschmieder, E.L. (1974). Steady supercritical Taylor vortices after sudden starts. *Phys. Fluids*, *17*, 1929.

Coles, D. (1965). Transition in circular Couette flow. *J. of Fluid Mech.*, *21*(3), 385–425.

Costa, P. and Trevissoi, C. (1972a). Reactions with non-linear kinetics in partially segregated fluids. *Chem. Eng. Sci.*, *27*, 2041.

Costa, P. and Trevissoi, C. (1972b). Some kinetics and thermodynamics features of reactions between partially segregated fluids. *Chem. Eng. Sci.*, *27*, 653.

Couette, M. M. (1890). tudes sur le frottement des liquides. *Ann. Chim. Phys.*, *6*(Ser. 21), 433–510.

Coughlin, K. T., Marcus, P. S., Tagg, R. P., and Swinney, H. L. (1991). Distinct Quasiperiodic Modes with Like Symmetry in a Rotating Fluid. *Phys. Rev. Lett.*, *66*, 1161–1164.

Coughlin, K. T. and Marcus, P. S. (1991). Vortices in Quasiperiodic Taylor-Couette Flows. *Lectures in Applied Mathematics*, *28*, 119–129.

Cui, J., Patel, V. C., and Lin, C. L. (2003). Large-eddy simulation of turbulent flow in a channel with rib roughness. *J. of Fluid Mech.*, *94*(1), 103–128.

Curran, S. J., and Black (2005) Oxygen transport and cell viability in an annular flow bioreactor: comparison of laminar Couette and Taylor-vortex flow regimes. *Biotechnol Bioeng.*, *89*(7), 766–74.

Davey, A. (1962). The growth of Taylor vortices in flow between rotating cylinders. *J. of Fluid Mech.*, *14*, 336.

Davey, A., DiPrima, R. C., and Stuart, J. T. (1968). On the instability of Taylor vortices. *J. of Fluid Mech.*, *31*(1), 17–52.

Delville, J., Ukeiley, L., Cordier, L., Bonner, J., and Glauser, M. (1999). Examination of large scale structures in a turbulent plane mixing layer, part 1. proper orthogonal decomposition. *J. of Fluid Mech.*, *391*, 91–122.

Dong, S. (2007). Direct numerical simulation of turbulent TaylorCouette flow. *J. of Fluid Mech.*, *587*, 373–393.

Dong, S. (2008). Turbulent flow between counter-rotating concentric cylinders: a direct numerical simulation study. *J. of Fluid Mech.*, *615*, 371–399.

Dopazo, C. (1994). Recent development in PDF methods. *Turbulent Reacting Flows*, 375–474. Academic Press, London.

Dring, R. P. (1982). Sizing criteria for laser anemometry particles. *ASME J. Fluids Eng.*, *104*, 15.

Dumont, E., Fayolle, F., Sboblik, V., and Legrand, J. (2002). Wall shear rate in the Taylor-Couette-Poiseuille flow at low axial Reynolds number. *International J. of Heat and Mass Transfer*, *45*, 679–689.

Dutcher, C. S. and Muller, S. J. (2009). Spatio-temporal mode dynamics and higher order transitions in high aspect ratio Newtonian TaylorCouette flows. *J. of Fluid Mech.*, *641*, 85–113.

Dutta, P. k., and Ray, A. K. (2004). Experimental investigation of Taylor vortex photocatalytic reactor for water purification. *Chem. Eng. Sci.*, *59*, 5248–5259.

Eagles, P. M. (1974). On the torque of wavy vortices. *J. of Fluid Mech.*, *62*, 751–755.

Eswaran, V. and Pope, S. B. (1988). Direct numerical simulations of the turbulent mixing of a passive scalar. *Phys. Fluids*, *31*, 506.

Farnik, J. and Kozubkova, M. (2006). Numerical simulation of the fluid instabilities in the gap between two rotating cylinder. *TRANSACTIONS of the VSB - Technical University of Ostrava*, http://transactions.fs.vsb.cz/2006-1/1495_FARNIK_Jiri_KOZUBKOVA_Milada.pdf. (accessed 19 April 2015)

Fenstermacher, P. R., Swinney, H. L., and Gollub, J. P. (1979). Dynamical instabilities and the transition to chaotic Taylor vortex flow. *J. of Fluid Mech.*, *94*, 103–128.

Fitchett, D. E. and Tarbell, J. M. (1990). Effect of mixing on the precipitation of barium sulfate in an MSMPR reactor. *AIChE J.*, *36*, 511.

Fox, R. O. (1996). The Fokker-Plank closure for turbulent molecular mixing: passive scalars. *Phys. Fluids A*, *4*, 1230–1244.

Fox, R. O. (2003). *Computational Models for Turbulent Reacting Flows*, Cambridge University Press, Cambridge.

Fox, R. 0. and Yeung, P. K. (2003). Improved Lagrangian mixing models for passive scalars in isotropic turbulence. *Phys. Fluids*, *15*, 961–985.

Friess, C., Poncet, S., and Viazzo, S. (2013). Taylor-Couette-Poiseuille flows: from RANS to LES. *International Symposium on Turbulence and Shear Flow Phenomena*, Conference paper.

Gardner, K. H. and Theis, T. L. (1996). A unified kinetic model for particle aggregation. *J. Colloid Interface Sci.. 180*, 162–173.

Gollub, J. P. and Swinney, H. L. (1975). Onset of Turbulence in a Rotating Fluid. *PhyS. Rev. Lett.. 35*(14), 927–930.

Gollub, J. P. and Freilich, M. H. (1976). Optical heterodyne test of perturbation expansions for the Taylor instability. *Phys. Fluids*, *19*, 618–626.

Gooch, J. R. V. and Hounslow, M. J. (1996). Monte Carlo simulation of size-enlargement mechanisms in crystallixaiton. *AIChE J.*, *42*(7), 1864–1996.

Gordon, R. G. (1968). Error bounds in equilibrium statistical mechanics. *J. Math. Phys.*, *9*, 655–663.

Gorman, M. and Swinney, H. L. (1979). Visual observation of the second characteristic mode in a quasiperiodic flow. *Phys. Rev. Lett.*, *43*(25), 1871–1875.

Gorman, M. and Swinney, H. L. (1982). Spatial and temporal characteristics of modulated waves in the Circular Couette system. *J. of Fluid Mech.*, *117*, 123–142.

Gorman, M. and Swinney, H. L. (1982). Modulated Wavy Vortex flow in Laboratory and Rotating Reference Frames, . *Phys. Rev. Lett.*, *87A*(9).

Haut, B., Amora, H. B., Coulonb, L., Jacquetb, A., and Halloin, A. (2003). Hydrodynamics and mass transfer in a CouetteTaylor bioreactor for the culture of animal cells. *Chem. Eng. Sci.*, *58*, 777–784.

Heikkila, W., and Hollis-Hallett, A. (1955). The viscosity of liquid helium II. *Can. J. Phys.*, *33*, 420–435.

Heinrichs, R. M., Cannell, D. S., Ahlers, G., and Jefferson, M. (1988). Experimental test of the perturbation expansion for the Taylor instability at various wavenumbers. *Phys. Fluids*, *31*, 250–255.

Higashitani, K., Ogawa, R., and Hosokawa, G. (1982). Kinetic theory of shear coagulation for particles in a viscous fluid. *J. Chem. Eng. Japan*, *15*, 299–304.

Hulburt, H. M. and Katz, S. (1964). Some problems in particle technology, a statistical mechanical formulation. *Chem. Eng. Sci.*, *19*, 555–574.

James, J. F. *A Student's Guide to Fourier Transforms with Applications in Physics and Engineering*, Third Edition.

Jones, C. A. (1981). Non-linear Taylor vortices and their stability. *J. of Fluid Mech.*, *102*, 249.

Jones, C. A. (1985). The transition ro wavy Taylor vortices. *J. of Fluid Mech.*, *157*, 135.

von Karman, T. (1934). Some aspects of the turbulence problem. *Proc. 4th Inter. Congr. For applied Mech.*, *Cambridge*, England, 54-91.

Kataoka, K. (1985). chapter Taylor vortices and instabilities in circular Couette flows *Encyclopedia of Fluid Mechanics*, *volume 1.*

King, G. P., Li, Y., Lee, W., Swinney, H. L., and Marcus, P. S. (1984). Wave speeds in wavy Taylor vortex flow. *J. of Fluid Mech.*, *141*, 365.

Kolmogorov, A. N. (1942). Equations of motion of an incompressible turbulent fluid. *Izv. Akad. Nauk. SSSR ser. Fiz.*, *6*, 56–58.

Kong, B., and Vigil, R. D., and Gollub, J. P. (2013). A Novel Taylor-Couette Photobioreactor for Energy Efficient Micro Algae Cultivation. *AIChE Annual Meeting*, *94*(1), 103–128.

Kramer, T. A. and Clark, M. M. (1999). Incorporation of aggregate breakup in the simulation of orthokinetic coagulation. *J. Colloid Interface Sci.*, *216*, 116–126.

Kravchenko, G., Moin, P., and Moser, R. (1997). Numerical Simulation of Three-Dimensional Couette-Taylor flows. *J. of Computational Phys.*, *127*(2), 412–423.

Launder, B.E., and Spalding, D.B. (1974). The numerical computation of turbulent flows. *Computer Methods in Applied Mech. and Eng.*, *3*(2), 269–289.

Lewis, G. S. and Swinney, H. L. (1999). Velocity structure functions, scaling, and transitions in high-Reynolds-number Couette-Taylor flow. *Phys. Rev. E*, *59*(5), 5457-67.

Liao, C. B., Jane, S. J., and Young, D. L. (1999). Numerical Simulation of Three-Dimensional Couette-Taylor flows. *International J. for numerical method in fluid*, *29*, 827-847.

Liu, S. S., Yao, L., and Wang, M. (1991). Phase Portraits and Flow Regimes in a Circular Couette System with Counter-Rotating Cylinders. *Chinese Phys.*, *8*(1).

Lueptow, R. M., Docter, A., and Min, K. (1992). Stability of axial flow in an annulus with a rotating inner cylinder. *Phys. Fluids A*, *4*(11).

Marchisio, D. L., Barresi, A. A., and Fox, R. O. (2001a). Simulation of turbulent precipitation in a semi-batch taylor-couette reactor using computational fluid dynamics. *Ind. and Eng. Chem. Res.*, *40*, 5132–5139.

Marchisio, D. L., Pikturna, J. T., Fox, R. O., Vigil, R. D., and Barresi, A. A. (2003a). Quadrature method of moments for population-balance equations. *AIChE J.*, *49*, 1266–1276.

Marchisio, D. L., Vigil, R. D., and Fox, R. O. (2003b). Implementation of the quadrature method of moments in CFD codes for aggregation-breakage problems. *Chem. Eng. Sci.*, *58*, 3337–3351.

Marchisio, D. L., Vigil, R. D., and Fox, R. O. (2003c). Quadrature method of moments for aggregation-breakage processes. *J. Colloid Interface Sci.*, *258*, 322–334.

Marchisio, D. L., Fox, R. O., Barresi, A. A., and Baldi, G. (2001b). On the comparison between presumed and full pdf methods for turbulent precipitation. *AIChE J.*, *47*, 664–676.

Marcus, P. S. (1984). Simulation of Taylor-Couette flow. Part 1. Numerical methods and comparison with experiment. *J. of Fluid Mech.*, *146*, 45–64.

Marcus, P. S. (1984). Simulation of Taylor-Couette flow. Part 2. Numerical results for wavy-vortex flow with one travelling wave. *J. of Fluid Mech.*, *146*, 65–113.

Moser, R. D., Moin, P., and Leonard, A. (1983). A Spectral Numerical Method for the Navier-Stokes Equations with Applications to Taylor-Couette Flow. *J. of Computational Phys.*, *52*, 524–544.

Nicmanis, M. and Hounslow, M. J. (1998). Finite-element methods for steady-state population balance equations. *AIChE J.*, *44*(10).

Noguchi, Y., Tsuda, K., and Shiomi, Y. (2011). Turbulent Characteristics in a Taylor-Couette Flow. *J.of JSEM*, *11*, Special Issue.

Parker, J. and Merati, P. (1996). An investigation of turbulent Taylor-Couette flow using Lase Doppler Velocimetry in a reflective index matched facility. *Trans. of the ASME*, *118*, 810–818.

Patte-Rouland, B., Lalizel, G., Moreau, J., and Rouland, E. (2001). Flow analysis of an annular jet by particle image velocimetry and proper orthogonal decomposition. *Mcas. Sci. Technoi.*, *12*, 1404–1412.

Pirro, D. and Quadrio, M. (2007). Direct Numerical Simulation of turbulent TaylorCouette flow. *European J. of Mech. B*, *27*, 552–566.

Prasad, A. K., Adrian, R. J., Landreth, C. C., and Offutt, P. W. (1992). Effect of resolution on the speed and accuracy of particle image velocimetry interrogation. *Expts. in Fluids*, *13*(1), 105–116.

Press, W. H., Teukolsky, S. A., Vetterling, W. T., and Flannery, B. P. *Numerical Recipes in C*, Second Edition.

Raman, V., Fox, R. O., Harvey, A. D., and West, D. H. (2001). CFD analysis of premixed methane chlorination reactors with detailed chemistry. *Ind. and Eng. Chem. Res.*, *40*, 5170–5176.

Raman, V., Fox, R. O., Harvey, A. D., and West, D. H. (2003). Effect of feed-stream configuration on gas-phase chlorination reactor performance. *Ind. and Eng. Chem. Res.*, *42*(12), 2544–2557.

Riechelmann, D. and Nanbu, K. (1997). Three-dimensional simulation of wavy Taylor vortex flow by direct simulation Monte Carlo method. *Phys. Fluids*, *9*, 811.

Roberts, P. H. (1964). The stability of hydromagnetic Couette flow. *Proc. Camb. Phil. Soc.*, *60*, 635–651.

Saffman, P. G. (1970). A Model for Inhomogeneous Turbulent Flow. *Proc. Roy. Soc. London*, *A317*, 417–433.

Salhi, Y., Si-Ahmed, E., Degrez, G., and Legrand, J. (2012). Numerical Investigations of Passive Scalar Transport in Turbulent Taylor-Couette Flows: LES versus DNS. *J. of Fluids Eng.*, *134*(4), 041105.

Schmitt, D., Alboussiere, T., Brito, D., Cardin, P., Gagniere, N., Jault, D., and Nataf, H. C. (2008). Rotating spherical Couette flow in a dipolar magnetic field: experimental study of magneto-inertial waves. *J. of Fluid Mech.*, *604*, 175–197.

Schmitt, Cardin, P., La Rizza, P., and Nataf, H. C. (2002). MagnetoCoriolis waves in a spherical Couette flow experiment. *European J. of Mech. B*, *Fluids 37*, 10–22.

Schroder, W. and Keller, H. B. (1990). Wavy Taylor-vortex flows via multigrid-continuation methods. *J. Comput. Phys.*, *91*, 197.

Seckler, M. M., Bruinsma, O. S. L., and Rosmalen, G. M. V. (1995). Influence of hydrodynamics on precipition: A computational study. *Chem. Eng. Comm.*, *135*, 113–131.

Sengupta, T. K., Kabir, N. F., and Ray, A. K. (2001). A Taylor vortex photocatalytic reactor for water purification. *Industrial and Eng. Chem. Research*, *40*(23), 5268–5281.

Shaw, R. S., Andereck, C. D., Reith, L. A., and Swinney, H. L. (1982). Superposition of traveling waves in the circular Couette system. *Phys. Rev. Lett.*, *48*, 1172.

Sirovich, L. (1987). Turbulence and the dynamics of coherent structures. *Quarterly of Applied Mathematics*, *5*, 564–590.

Smith, G. P. and Townsend, A. A. (1982). Turbulent Couette flow between concentric cylinders at large Taylor numbers. *J. of Fluid Mech.*, *123*, 187–217.

Smith, M. and Matsoukas, T. (1998). Constant-number Monte Carlo simulation of population balances. *TChem. Eng. Sci.*, *53*, 1777–1786.

Sodja, J. (2007). *Turbulence models in CFD*, .

Spalart, P. R. and Allmaras, S. R. (1992). A One-Equation Turbulence Model for Aerodynamic Flows. *AIAA Paper*, *92*, 0439.

Speziale, C. G. (1991). Analytical methods for the development of Reynolds-stress closures in turbulence. *Annu. Rev. Fluid Mech.*, *23*, 107–157.

Swift, J. B., Gorman, M., and Swinney, H. L.(1982). Modulated wavy vortex flow in laboratory and rotating reference frames. *Phys. Lett.*, *88*(A), 457–460.

Swinney, H. L. (1983). Observations of Order and Chaos in Nonlinear System. *Physica D*, *7*(1-3), 3–15.

Takeda, Y., Fischer, W. E., Kobashi, K., and Takeda, T. (1992). Spatial characteristics of dynamic properties of modulated wavy vortex flow in a rotating Couette system. *Exps. in Fluids*, *13*(2-3), 199–207.

Takeda, Y. (1999). Quasi-periodic state and transition to turbulence in a rotating Couette system. *J. of Fluid Mech.*, *389*, 81–99.

Takeda, Y., Morinaga, M., and Tasaka, Y. (2008). Oscillating Taylor-Couette Flow (Azimuthal motion). *J. of Phys., Conference Series*(2008), 012002.

Taylor, G. I. (1923). Stability of a viscous liquid contained between two rotating cylinders. *Phil. Trans. Roy. Soc. A*, *233*, 298–343.

Taylor, G. I. (1933). Fluid friction between rotating cylinders I - Torque measurements. *Proc. R. Soc. A*, *157*, 546–564.

Thomas, D. G., Khomami, B., and Sureshkmar, R. (2009). Nonlinear dynamics of viscoelastic TaylorCouette flow: effect of elasticity on pattern selection, molecular conformation and drag. *J. of Fluid Mech.*, *620*, 353–382.

Tsai, K. and Fox, R. O. (1998). The BMC/GIEM model for micromixing in non-premixed turbulent reacting flows. *Ind. and Eng. Chem. Res.*, *37*, 2131.

Versteeg, H. K., and Malalasekera, W. *An Introduction to Computational Fluid Dynamics*, Second Edition.

Walden, R. W. and Donnely, R. J. (1979). Reemergent Order of Chaotic Circular Couette Flow. *Phys. Rev. Lett.*, *42*(5).

Wang, L., Olsen, M. G., and Vigil, R. D. (2005) Reappearance of azimuthal waves in turbulent TaylorCouette flow at large aspect ratio. *Chem. Eng. Sci.*, *60*, 5555–5568.

Watanabe, T., and Toya, Y. (2012) Vertical TaylorCouette flow with free surface at small aspect ratio. *Acta Mech.*, *223*, 347–353.

Wei, H. and Garside, J. (1997). Application of CFD modelling to precipitation systems. *Trans. IChemE*, *75 Part A*, 217–227.

Wendt, F. (1933). Turbulente Stromungen zwischen zwei rotierenden konaxialen Zylindern. *Ing. Arch.*, *4*, 577–595.

Wereley, S. T. and Lueptow, R. M. (1994). Azimuthal velocity in supercritical circular Couette flow. *Exps. Fluids*, *18*, 1–9.

Wereley, S. T. and Lueptow, R. M. (1998). Spatio-temporal character of non-wavy and wavy Taylor-Couette flow. *J. of Fluid Mech.*, *365*, 59–80.

Wereley, S. T. and Lueptow, R. M. (1999). Velocity field for Taylor Couette flow with an axial flow. *Phys. Fluids*, *11*, 3637–3649.

Wereley. S.T., Akonur, A., and Lueptow, R.M. (2002). Particle-fluid velocities and fouling in rotating filtration of a suspension. *J. of Membrane Sci.*, *209*, 469–484.

Wilcox, D. C., and Alber, I. E. (1972). A turbulence model for high speed flows. *Proceedings of the 1972 Heat Transfer and Fluid Mech. Ins.*, *Stanford University Press*, 231–252.

Wilcox, D. C. (1988). Reassessment of the Scale-Determining Equation for Advanced Turbulence Models. *AIAA J.*, *26*(11), 1299–1310.

Wilcox, D. C. (1993). *Turbulence Modeling for CFD*, Third Edition.

Wilcox, D. C. (1993). Comparison of Two-Equation Turbulence Models for Boundary Layers with Pressure Gradient,. *AIAA J.*, *31*(8), 1414–1421.

Wilcox, D. C. (1994). Simulation of Transition with a Two-Equation Turbulence Model. *AIAA J.*, *32*(2), 247–255.

Wilcox, D. C. (2000). *Turbulence Modeling for CFD*, *DCW Industries, Inc.*, CA, Second Edition.

Wild, P. M., Djilali, N., and Vickers, G. W. (1996). Experimental and computational assessment of windage losses in rotating machinery. *Trans. ASME: J. Fluids Engng*, *118*, 116–122.

Yeung, P. K. (2001). Lagrangian characteristics of turbulence and scalar transport in direct numerical simulations. *J. of Fluid Mech.*, *427*, 241–274.

Zhang, J. and Li, X. (2003). Modelling particle-size distribution dynamics in a flocculation system. *AIChE J.*, *49*, 1870–1882.

Zhang, L., and Swinney, H. L. (1985). Nonpropagating oscillatory modes in Couette-Taylor flow. *Phys. Rev. A*, *31*, 1006–1009.